Constraining the Presence of Helium in Type Ia Supernovae

A thesis submitted for the degree of Master of Science (MSc)

April 2021

Kelly Skillen

Trinity College Dublin
Coláiste na Tríonóide, Baile Átha Cliath
The University of Dublin

Declaration

I declare that this thesis has not been submitted as an exercise for a degree at this or any other university and it is entirely my own work.

a) I agree to deposit this thesis in the University's open access institutional repository or allow the Library to do so on my behalf, subject to Irish Copyright Legislation and Trinity College Library conditions of use and acknowledgement.

b) In the case of a thesis for which the work has been carried out jointly; the declaration must have a statement that it includes the unpublished and/or published work of others, duly acknowledged in the text wherever included.

c) Open access electronic theses are freely available over the World Wide Web for users to read, copy, download, and distribute subject to Irish Copyright Legislation and Trinity College Library conditions of use and acknowledgement. Withheld access will be implemented, as applicable, according to the terms in Calendar Part III section 1, paragraph 114.

d) A digital repository is an online, searchable, web-accessible database containing works of research deposited by scholars, the purpose of which is both increased access to scholarship and long-term preservation.

Kelly Skillen

Summary

The aim of this thesis is to investigate the possibility of visible helium features in the near-infrared region of the spectra of Type Ia supernovae, in particular a single feature thought to appear around 10250 Å, caused by the He I 10830 Å line. It is theorised that helium features will appear around this region if the supernova was caused by a helium shell detonation (Boyle et al. 2017). However, there have been very few detections of these types of events in nature. The purpose of this thesis was to create a large sample of Type Ia supernovae, spanning a range of their different spectral classes to try and find a handful of objects which may have been possible helium shell detonation events. The spectral data of 33 Type Ia supernovae were taken using the X-Shooter echelle spectograph on the Very Large Telescope (VLT). Common spectral features (Si II 6355 Å, Ca near-infrared (NIR) triplet and O I 7773 Å) were then fit using a new velocity fitting code for all supernovae in the sample. These are three features which appear in nearly all Type Ia spectra and can be used to build an idea of the line forming regions of the ejecta. This is important in cases when investigating uncertain spectral features, such as the helium features in the NIR region, especially as this feature can be blended in with the C I 10693 Å and Mg II 10927 Å lines. These velocity fits can help to break the degeneracy between different blends.

The next step after measuring velocity ranges for different features across the sample was to visually inspect the NIR region of all of the spectra to see which contained features around 10250 Å. Out of the 33 supernovae in this sample, 9 objects had features which were in the correct spectral region to be possible helium detections. Again, the velocity fitting code was used to simulate these features and estimate velocities for their constituents. The initial velocities from the Si, Ca and O fits were then used to determine which of these elements was the most likely cause of the NIR feature.

Out of the 9 objects with a feature, 7 were found to most likely be made entirely of Mg II. 2 of the objects, SN 2017gah and SN 2017ejb, were found to be a likely blend of the Mg II 10927 Å and He I 10830 Å lines.

To confirm or deny the possibility of a helium feature in these two events, the radiative transfer code TARDIS was used to create model spectra of the objects to test whether synthetically, the feature could be made with a blend of helium and magnesium. In these models, a subluminous density and abundance profile, based off the work of Heringer et al. 2017, were used to model the objects as they were both deemed to be

subluminous events.

It was found that both events were reasonably well modelled with helium shell detonations. SN 2017gah was best fit by a helium shell model spanning a velocity range of 11836 – 27014 km s^{-1} with a post-burning helium shell mass of 0.0236-0.0591 $M_{\odot}$. This gave a helium velocity of 11572 – 11870 km s^{-1}, which is in good agreement with the initial velocity fit which estimated the feature would have a velocity of 11860 km s^{-1} if it were made of helium. SN 2017ejb was best fit with a helium shell model spanning a velocity range of 13598 – 27014 km s^{-1} with a post-burning helium shell mass of 0.0064 $M_{\odot}$. This corresponds to a helium velocity of 13735 km s^{-1}. Again, this is in good agreement with the initial velocity fit (13922 km s^{-1}).

Both of these velocities are lower than those predicted by the models of Boyle et al. 2017 ($\sim$ 16000 – 19000 km s^{-1}). It is thought that the difference between the two sets of models is due to the density profiles used in each - Boyle et al. 2017 used steeper density profiles, similar to the common ω7 model used for normal luminosity events. The ones in this thesis were shallower and it is likely that this allowed for the difference between the recovered velocities of features, though further work would need to be carried out to prove this hypothesis.

Out of a total of 33 type Ia supernovae, 1-2 events containing possible helium features corresponds to a minimum of $\sim 3 - 6\%$ of the sample which could have been potential helium shell detonations. The true number could, in fact, be higher as a non-detection of helium does not necessarily preclude the possibility of a helium shell detonation, as found in this thesis. Both of these objects were subluminous events, though it is thought that helium features may also be visible in normal luminosity events if they were caused by a helium shell detonation. If this rate is indicative of subluminous events, then it would be expected that a handful of helium shell detonations would be detected each year. If normal luminosity events can also be included in this figure, then the number of expected detections should increase even more. The fact that there have been so few detections of these kinds of objects suggests that perhaps some of these events are being missed and a new observing strategy focusing on near-infrared detections such as those used in this thesis may help to improve the sample size in the future.

Acknowledgements

I would like to thank my supervisor, Dr Kate Maguire, for all of her help and support throughout this project. It has been a genuine pleasure to work with her - she always made time for me and had advice to offer when I needed it but allowed me to work independently and at my own pace. Her and the rest of her group were always incredibly welcoming and always willing to answer any questions (and spend hours installing and reinstalling software onto my computer until we finally got it, however unwittingly).

I would also like to thank Kate and the team of scientists at the VLT who collected the spectral and photometric data used within this thesis and Epson Heringer for providing the subluminous density and abundance profiles from his paper for use in this thesis. Without all of them, this work wouldn't have been possible.

At the risk of sounding like an Oscar winner, I am going to continue and thank my friends and family. I know it hasn't been easy listening to me explain why helium in Type Ias is important or complaining that my code is broken again, in a new-but-not-really-any-less-broken way this time, so I very much appreciate the efforts that were made. A particular mention has to go to my cousin Caitlyn for her idea to 'just Google whether they have helium or not.' I would have saved myself some work if I had just taken her advice!

A special thanks to my parents, Brenda and Colin, for supporting me throughout this project (and driving me to the Dublin bus at unholy hours in the morning) and to my brother, Rory, for all the pep talks at 1am.

Thank you as well to Chris and Shannon for all of the lunch time coffees and coming to steal me away from work every now and again. Thank you to Greg for all the after work Stardew and Stick Fights. And finally, thank you to Lara for always telling me that I could do it, every step of the way and for reminding me to relax and stream a movie at the weekends. You were definitely my common sense more than once.

Contents

List of Figures

List of Tables

Chapter 1: Introduction

There is a long history of supernovae observations which dates back to at least 185 AD (Zhao et al. 2006) and possibly as far back as 4500±1000 BC (Joglekar et al. 2006). At the time, it was not understood what caused these seemingly new stars to appear in the sky, sometimes bright enough to be seen during the day before they faded away months later, never to be seen again. Now we understand that these events were not new stars or 'guest stars' as the Chinese observers described them but are instead supernovae; extremely bright explosions caused by the deaths of stars.

Despite having been observed for possibly millennia, it was not until after supernova SN 1885A, which occurred in the Andromeda galaxy (Chevalier et al. 1988), that the true nature of supernovae started to be uncovered. The term 'super-novae' was first used by Walter Baade and Fritz Zwicky to describe this new class of events in a paper they had written on SN 1885A in 1934 (Baade et al. 1934) and this is the real beginnings of the supernovae field of study. More of these events were discovered in galaxies outside of the Milky Way throughout the 20th century which allowed astronomers to see the diversity in the types of supernovae and develop classifications systems for these new events. It also allowed some insights into the nature of the progenitors of these events as the numbers of observations grew steadily.

Since the dawn of large scale surveys such as LSST (Large Synoptic Survey Telescope; Ivezić et al. 2019), Pan-STARRS (Panoramic Survey Telescope and Rapid Response System; Chambers et al. 2016) and ZTF (Zwicky Transient Facility; Graham et al. 2019), the numbers of observations of all classes of supernovae have increased dramatically, from a handful of events to hundreds or thousands. These surveys have also increased the detections of outliers to the original groupings, leading to a much greater diversity than was initially believed. However, the original classification system is still widely used and new classes or sub-classes have simply been added, making it increasingly complicated.

1.1 Supernovae Types

The diversity in stellar types means that there are also a wide variety of supernova (SN) types. As previously mentioned, the classes and sub-classes of supernovae are ever-changing and maintaining a classification system can be challenging. Initially in

this chapter, the simplest version of the system still in use today is described, though there are many sub-classes which branch off from those discussed here which are not mentioned as they are not relevant in the context of this investigation.

The first part of the classification of supernovae is dependent on whether hydrogen lines appear in the spectrum of the object. If hydrogen cannot be seen, the SN is classified as a 'Type I' (Type 1) SN. This definition of 'type I' dates back to Minkowski in 1941 (Minkowski 1941). If there are visible hydrogen lines, then it is a 'Type II' (Type 2).

1.2 Core-Collapse Supernovae

Within these categories, supernovae (SNe) are divided up further into different classes. Type II supernovae can be divided further into IIn, IIb, II-L or II-P. IIn show narrow hydrogen lines in their spectra. IIb are named as such because although initially they appear to have weak hydrogen lines, later these disappear from the spectrum and it more closely resembles the Type Ib category, which is defined further on in this chapter. II-L and II-P are categorised based on light curve shape rather than spectral features, with II-L showing a linear decline in the light curve whilst II-P show a plateau in the decline.

Type I supernovae are also divided into further classes; Ia, Ib and Ic, based on their spectra. If a SN shows no hydrogen but shows helium, it is classified as Type Ib and is similar to the IIb type, except for the initial hydrogen detection in the IIb. Type Ia and Ic supernovae both show no hydrogen or helium but Ia differ from Ic supernovae in that they show strong silicon absorption; this absorption feature is the defining characteristic of the Ia class. If the SN shows no hydrogen, helium or strong silicon, it is then a Type Ic.

These type classes were created from the limited information that could be gathered from the earliest observations of these objects. As we learned more about the different types, it was found that perhaps this was not the best way to divide the supernovae but despite this, the original system persists. We now know that Type Ib, Ic and Type II supernovae are all caused by the collapse of the cores of massive stars and are hence collectively known as 'core-collapse' supernovae. Type Ia supernovae (SNe Ia) differ from the other categories in that they are not caused by the collapse of giant stars, but rather by thermonuclear runaway on the surface or near the centre of a particular stellar remnant, known as a white dwarf, which then unbinds the remnant

in an explosion (explained further in Chapter 1.4). It is this unique explosion channel that makes Type Ia supernovae such interesting and useful objects within astrophysics. Within the core-collapse group of SNe, there are many different sub-classes, such as superluminous supernovae (SLSNe; Quimby et al. 2007) and 'interacting' supernovae such as Ibn or the previously mentioned IIn, named for the narrow emission features they both show (helium for Ibn and hydrogen for IIn, see Pastorello et al. 2007 and Schlegel 1990 respectively). However, these sub-classes are not relevant to this thesis and so are not discussed further.

1.2.1 Thermonuclear Supernovae

Though there are numerable sub-classes of supernovae within the classes mentioned above, as this investigation focuses on Type Ia supernovae and not core-collapse events, only further sub-classes of the thermonuclear Ia category will be discussed. Even within this category alone, there are still many further divisions which can be made and so only a few of the sub-types which are most relevant to this investigation are mentioned. There are at least three main sub-classes within the Ia category. These are known as 'normal', 'subluminous' and 'over-luminous' events. 'Normal' luminosity events are ones in which the light curve has a rise time of around 19 days and peaks at a magnitude of $\sim$ –19.3 mag in the B-band filter (Phillips 1993).

'Subluminous' events are ones in which the light curve peaks at least 1.5 magnitudes fainter than the normal -19.3 mag (i.e. $\sim$ –17.8 mag due to the way the magnitude system works). There are a few subluminous sub-classes but perhaps the most common are those in the '91bg-like' category. This class of events are similar to the original subluminous event SN 1991bg, which this class is named after. These supernovae tend to have stronger Si II 5972 Å and O I 7773 Å lines than those found in the spectra of 'normal' Ias, as well as being less luminous and having faster declines in their light curves (Filippenko et al. 1992a, Ruiz-Lapuente et al. 1993, Taubenberger 2017).

The other main type of SNe Ia are the 'over-luminous' events. The most commonly referred to type of 'over-luminous' SNe Ia are a sub-class known as '91T-like' events, which are named after SN 1991T, the first of these events to be recorded (Filippenko et al. 1992b, Phillips et al. 1992). Initially, there was a controversy about how much brighter these events were compared to 'normal' luminosity events. Some of the initial papers disagreed vastly on the magnitude, with estimates ranging from 0.3 mag to at

least 1.0 mag brighter (Phillips et al. 1992, Filippenko et al. 1992b, Ruiz-Lapuente et al. 1992) but modern estimates suggest that this number is, on average, lower, usually around 0.3 mag brighter than 'normal' events (Sasdelli et al. 2014, Taubenberger 2017). A more important characteristic of these '91T-like' events is their initial lack of the usual Si II and Ca II lines which appear in 'normal' luminosity spectra and the weakness of these lines once they do appear around maximum light. Unlike 'normal' events, '91T-like' spectra instead show high UV flux, strong Fe III lines around 4250 and 4950 Å and an almost featureless blue continuum beyond 5500 Å. Their light curves also decline slower than those of 'normal' luminosity events. Figure 1, adapted from Taubenberger 2017, shows all of these sub-classes, plus several which are not discussed here e.g. Type Iax (Wang et al. 2013), calcium-rich (Ca-rich; Perets et al. 2010) and Ia which interact with circumstellar material (Ia-CSM; Hamuy et al. 2003), to give an idea of the magnitudes ($M_{B,max}$) and decline times ($\Delta m_{15}(B)$) of the different events, relative to the other sub-classes.

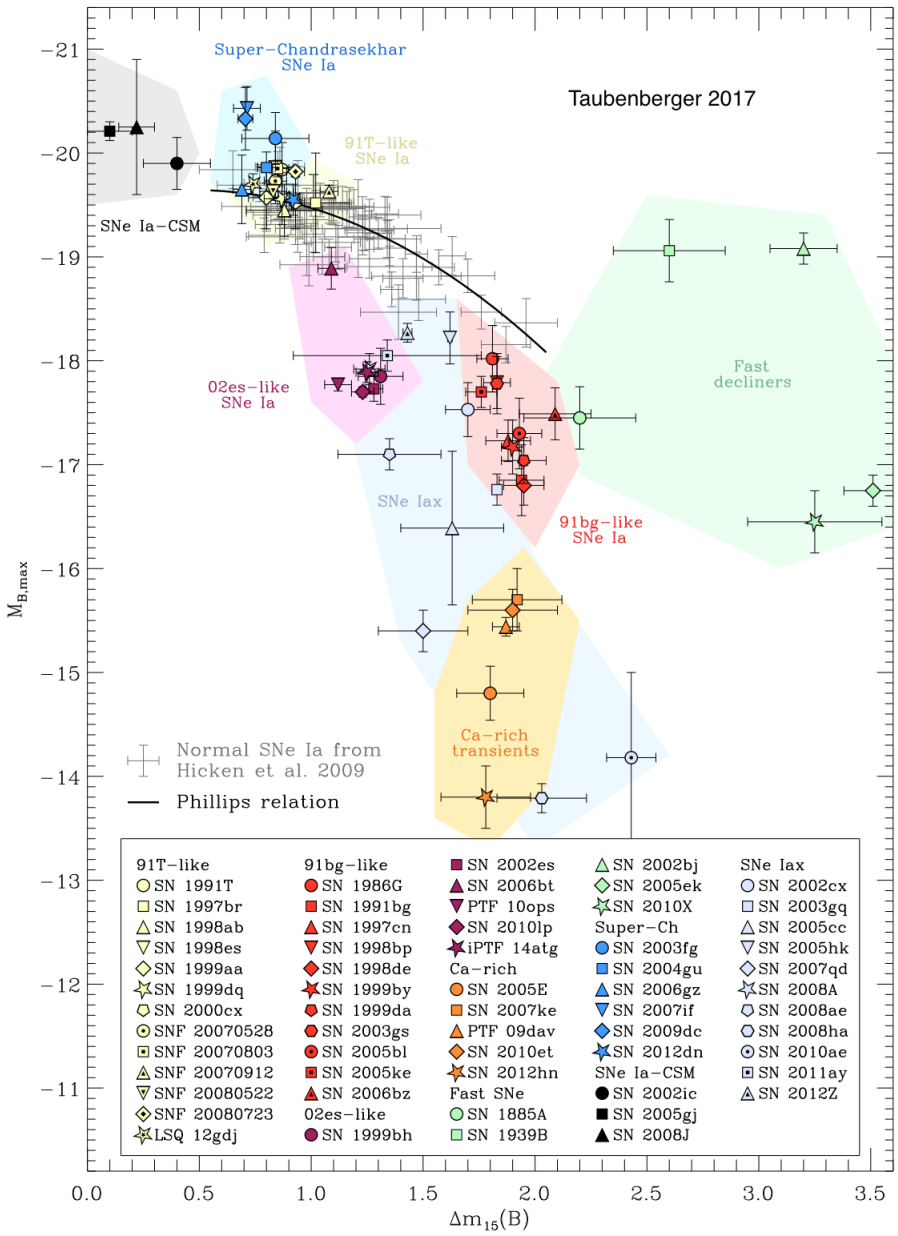

Figure 1: Sub-classes of Type Ia supernovae, adapted from Taubenberger 2017. This figure shows magnitude versus light-curve decline rate and the Phillips relation which is used to correct the luminosity and decline rate of outliers to use in cosmological studies (see Chapter 1.3).

1.3 Type Ia Supernovae in Cosmology

SNe Ia are a uniquely important tool in discovering the nature of our Universe. They have been used to prove that the Universe is expanding at an accelerated rate (Riess et al. 1998, Perlmutter et al. 1999) and are also one of the most precise methods of measuring the amount of dark matter and dark energy in the Universe. They can also be used to put stringent constraints on the nature of dark energy (Betoule et al. 2014, Scolnic et al. 2018), which ultimately predicts the fate of the Universe. SNe Ia are one

of the most powerful distance estimators in the Universe due to their unique physical characteristics e.g. high luminosity meaning they can be measured to high redshift, giving them a status that almost no other optical transients can claim. However, despite the unending usefulness of these objects and the numerous studies carried out into their nature, the progenitors of these supernovae are still somewhat unclear.

In theory, SNe Ia would be expected to all have the same peak luminosity if they all exploded at the same mass; the so-called Chandrasekhar mass limit (see Chapter 1.4) but some SNe Ia are also produced by white dwarfs which have not reached this limit. These events are aptly named sub-Chandrasekhar SNe Ia. All white dwarfs would need to explode at the Chandrasekhar limit to make SNe Ia what are known as 'standard candles', i.e. an object of known brightness, which then allows the distance to the object to be measured accurately, using the known luminosity-distance equation. However, as discussed in Chapter 1.1, there is a known variability in the peak magnitude of these objects, which can be caused by many different factors, such as these sub-Chandrasekhar events. SNe Ia are not perfect standard candles but this does not affect their ability to measure distances accurately. Instead, SNe Ia are known to be good 'standardisable candles', meaning that they can be corrected to become a pseudo-standard candle. The variability in the shape of the light curve can be shifted in magnitude and time (known as colour and stretch corrections respectively) so that the light curve agrees with the template SNe Ia light curve which would be created by an explosion of a white dwarf close to the Chandrasekhar limit. Hence, it can still be used as a pseudo-standard candle to measure an accurate distance to the object.

The relationship between a SNe Ia and its peak magnitude was first discovered in 1993 and is known as the Phillips relationship. It states that SNe Ia with wider light curves (i.e. slower fading) are more luminous than those with narrower light curves (Phillips 1993). Initially, the rate at which the light curve faded over 15 days after peak (Δm_{15}) was used to correct the light curve shape but this has since been replaced by stretch (s or x_1; Jha et al. 2007, Guy et al. 2007, Conley et al. 2008), which measures the width of the light curve, though some studies still use Δm_{15}. This relationship between the width of the light curve and the luminosity of the SN, plus the corrections for colour and luminosity is what allows SNe Ia to be 'standardisable candles'.

It has also recently been discovered that there is an apparent relation between the mass of the host galaxy and the residuals of SN brightness after the light curves have been corrected (see, for example, Sullivan et al. 2006, Conley et al. 2011, Betoule et al.

2014, Roman et al. 2018), though there is much controversy over this observation, for example, there is a debate over whether the differences between hosts could be due to dust or not. It is also thought that correlations could exist between other host galaxy properties and the residuals after the light curve has been corrected, such as local star-formation rate (SFR, Rigault et al. 2015 but also see Jones et al. 2015), global specific star formation rate (sSFR; Uddin et al. 2017), galactic metallicity (Childress et al. 2013b, Moreno-Raya et al. 2016), stellar age (Childress et al. 2013b) and H_α emission (Rigault et al. 2013), which only worsens the controversy as the apparent relation in host galaxy mass could be underpinned by any of these other properties or could simply be an additional factor. These 'extra' corrections may or may not be necessary as an additional correction to the Phillips relation and work is still being carried out into this area.

Some subcategories of SNe Ia, such as the faint SNe Iax, do not follow the Phillips relationship (Magee et al. 2018) and are not used for cosmological studies as their magnitudes cannot be corrected in this fashion. It is thought that these peculiar objects are created by a different explosion mechanism than those which create SNe Ia, which would explain why they do not follow this relationship. Although there are exceptions to the Phillips relationship, for the majority of SNe Ia, it is a powerful tool which allows them to be used as accurate distance estimators.

This relationship, however, is based on empirical evidence and the reasons behind this inherent trait are not yet fully understood. This means that despite being widely accepted as a means to deal with the differences in light curve shapes, further investigation is still required into the reasons why these variances exist in the first place. It may be found that there is a better correction or that another parameter needs to be added to the Phillips relationship to more accurately carry out this correction, or indeed, that there is a particular subgroup of SNe Ia which come from one progenitor type which makes them stronger distance indicators than the others and perhaps they should be used instead of trying to correct other subgroups. Without knowing the cause of this relationship, it is difficult to say for certain that this is the best treatment of these objects and so, more work needs to be carried out into determining the progenitors of these explosions to ensure accuracy in any cosmological parameters.

1.4 SNe Ia Explosion Physics

It is now understood that SNe Ia are caused by the explosions of low mass stellar remnants known as white dwarfs (WD). WD are made from stars which are not massive enough ($<\sim 8M_{\odot}$) to undergo core-collapse to become a neutron star or black hole. Instead, the star sheds its outer layers and leaves behind a lump of carbon and oxygen (the WD) when helium fusion ceases within the core, as the star is not massive enough to reach the temperatures required for carbon fusion to start. The WD then begins to cool and given enough time, will become a black dwarf, provided there is no further interaction between the WD and a companion (see, for example, Fontaine et al. 2001). SNe Ia occur when there is interaction between a WD and a companion. In the classical scenario, as the WD accretes mass from the companion, it will continue to grow until it approaches the Chandrasekhar limit of $\sim 1.44M_{\odot}$ (Chandrasekhar 1931, Chandrasekhar 1935, Anand 1965). As the mass increases, the central density of the WD also increases until finally, fusion occurs. This triggers thermonuclear runaway of carbon and oxygen in the WD, causing a SNe Ia (Hoyle et al. 1960, Nomoto et al. 1984, Blondin et al. 2012).

It is now widely believed that SNe Ia could come from at least two different progenitor channels. The first is known as the 'single-degenerate' channel. This channel involves a WD and a non-degenerate companion star, e.g. a main-sequence, sub-giant star or helium star. Non-degenerate in this scenario means any star which is not a WD or a neutron star, i.e. any star not being held up against gravitational collapse by electron or neutron degeneracy pressure. In this channel, the WD accretes matter over time from the non-degenerate companion. Most WD will accrete matter until it approaches the Chandrasekhar limit and then explodes in a SN (Whelan et al. 1973, Nomoto 1982), however, there is also a single-degenerate channel where the WD accretes matter from a non-degenerate helium star and explodes as a sub-Chandrasekhar event (i.e. a SN which occurs before reaching the Chandrasekhar limit; see, for example, Nomoto et al. 2018).

There are a number of proposed explosion mechanisms within the 'single-degenerate' progenitor channel for creating Chandrasekhar mass explosions to try and explain the wide variety of observed properties of all the known sub-classes of SNe Ia. One method is known as 'delayed detonation' in which subsonic burning (deflagration) within the WD after some time becomes supersonic burning (detonation), which unbinds the WD

and causes the SN. This is thought to happen in WD near the Chandrasekhar mass limit and is one of the most popular methods for creating normal and subluminous SNe Ia (Blondin et al. 2013, Seitenzahl et al. 2013).

There is a similar method which is known as the 'pure deflagration' model, where the burning in the WD never becomes a detonation. In these models, the WD does not become fully unbound, meaning that a remnant is left behind after the event. This is thought to be a good method for creating very fast and subluminous events, such as SNe Iax (Foley et al. 2013, Fink et al. 2014, Magee et al. 2016, Magee et al. 2018).

The second progenitor channel is known as the 'double-degenerate' channel. This is when the WD interacts with another degenerate companion, usually another WD, and accretes material from it, or merges with it, triggering a detonation and causing a SNe Ia (Iben et al. 1984, Webbink 1984, Shappee et al. 2018). It is thought that both the single- and double-degenerate channels are viable methods of making SNe Ia and that both probably occur in nature, however, there is still uncertainty about whether one is more common or how the different progenitor channels affect the observed light curve and spectral features of the SN.

To make matters more complicated, it is also thought that SNe Ia which occur through the double-degenerate channel may happen before the Chandrasekhar mass limit is reached. These events are known aptly as 'sub-Chandrasekhar' explosions and are thought to create some of the subluminous types of SNe Ia, such as '91bg-like' SN mentioned previously and 'normal' luminosity events (Blondin et al. 2017). There was also an idea that there could be 'super-Chandrasekhar' SNe Ia; explosions where the WD had existed above the Chandrasekhar limit due to the spin of the WD before exploding, which could explain the over-luminous groups such as the '91T-like' class. This idea has recently lost traction as the models of 'super-Chandrasekhar' explosions do not match the spectral or photometric properties of any known class of SNe Ia (Fink et al. 2018) and it is now thought that the over-luminous nature of these objects may be due to interactions (Noebauer et al. 2017).

1.4.1 Double-Detonation Scenario

The explosion mechanism that is investigated within this analysis is known as the 'double-detonation' or 'helium-shell detonation' model. In this model, the WD accretes a helium shell from a companion, through either the single- or double-degenerate

progenitor channel. An initial detonation within the helium shell propagates around the surface of the WD and penetrates into the carbon-oxygen (CO) core, causing a secondary detonation which unbinds the WD in a SNe Ia explosion (Fink et al. 2010, Sim et al. 2010, Sim et al. 2012, Shen et al. 2014, Shen et al. 2018). Depending on the mass of the WD and of the helium shell, it is possible that this explosion mechanism will leave traces of helium within the spectrum of the SNe Ia and will cause the early colours of the light curve to appear bluer before turning red, perhaps even creating a so-called early 'bump' in the shape of the light-curve due to its rise initially being powered by radioactive material produced in the outer ejecta before the usual power source of ^{56}Ni takes over (Boyle et al. 2017, Noebauer et al. 2017, Polin et al. 2019). Whilst there are other suggestions for creating early time light curve bumps (for example, clumps of nickel in the ejecta: see Magee et al. 2020 and references within), no other proposed explosion mechanism for creating SNe Ia would show traces of helium in the spectrum. Finding signatures of this is a smoking gun, pointing directly to a helium shell explosion.

1.5 Observational Constraints on Double Detonations

Despite the detection of helium appearing to be a simple diagnostic for a helium shell detonation, there are remarkably few detections of these kind of events. There are several 'normal' luminosity SNe Ia which have been caught early enough to show a potential 'bump' in the light curve; SN 2017cbv (Hosseinzadeh et al. 2017, Sand et al. 2018), SN 2018oh (Shappee et al. 2018, Dimitriadis et al. 2018, Li et al. 2018) and SN 2019yvq (Miller et al. 2020). The cause of these 'bumps' is still open to debate and helium-shell models have not yet been entirely ruled out in these cases.

To date, only a handful of candidates have been put forward as helium-shell detonation events with the two most likely events being SN 2016jhr (Jiang et al. 2017) and SN 2018byg (De et al. 2019). Both of these events differ from each other, with SN 2016jhr thought to have been caused by a thin helium shell ($\sim 0.054 M_{\odot}$) whilst SN 2018byg is thought to have been caused by a thick helium shell ($\sim 0.15 M_{\odot}$). A third event, SN 2019yvq, was also recently modelled with a thin helium shell ($0.04 M_{\odot}$) and reproduces some of the light curve features but fails to reproduce all of them or to reproduce the spectrum of the object, making this a less likely candidate than the others (Miller et al. 2020). The fact that there have only been a handful of plausible detections so

far and that these events are thought to come from drastically different progenitors may suggest that these types of events are intrinsically rare, or it could suggest that these events were all caused by thicker helium shells and that events caused by thinner helium shells are more common but more difficult to detect.

An alternative, or perhaps additional explanation for the lack of conclusive observations comes from the position of the proposed helium features in the spectra of these objects. It is expected that visible He I features will appear around 10830 Å and 20000 Å (also known as the 2μm line), both of which fall into the near infrared (NIR) region of the spectrum (Boyle et al. 2017). There are also optical helium lines produced but these are much weaker than the 10830 Å line and even harder to distinguish. This in itself poses problems for detection. The Earth's atmosphere creates some strong telluric absorption lines in this NIR region, making the data noisy and increasing the difficulty of observing any feature with ground-based instruments. Another problem is that many detectors do not extend to this range beyond visible wavelengths and so cannot be used to detect these events due the weakness of the helium lines in the optical region (see, for example, Figure 2 of De et al. 2019). For the two possible helium-shell objects mentioned above, De et al. 2019 had one NIR spectrum of SN 2018byg taken with the Multi-Object Spectrometer for Infrared Exploration (MOSFIRE) that covered the 10830 Å region but not the 2μm but do not comment specifically on the detection and Jiang et al. 2017 had no infrared spectra of SN 2016jhr. All of this combined makes detections incredibly difficult and means that even if these events are not rare, many of them may be missed.

Covering a wider wavelength range out to the 2μm region gives a distinct advantage in confirming the presence of helium. Boyle et al. 2017 suggests that although the He I 10830 Å should be visible in both normal and subluminous SNe Ia spectra if a helium shell detonation has occurred, the presence of two other lines; C I 10693 Å and Mg II 10927 Å, at high enough velocities could blend with the He I 10830 Å and disguise the feature. The ability to check whether the other He I feature shows around 2μm in the spectra used in this investigation allows for a more robust detection of He I than those previous.

As already discussed, detections of the characteristic indicators of a helium shell detonation are challenging. The early blue colours and the 'bump' in the light curve are only visible for a very short time after explosion (∼5 days after explosion), whereas many SNe Ia are usually not observed until nearer maximum light (∼19 days after ex-

plosion). This means that most SNe Ia are not caught early enough to use this feature as a confirmation of a helium shell detonation.

Even if an event is caught early enough to detect this early flux excess, it is not enough to say whether a helium shell detonation occurred, as there are other methods which also produce early light curve bumps e.g. nickel clumps. Nickel clump models also predict the suppression of blue flux, as do helium shell models, due to the short-lived radioactive isotopes. This means that detecting helium features is a much more decisive indicator of a helium shell detonation.

The helium features in the spectrum appear at later times, around a week before maximum light and last until at least a week after (Boyle et al. 2017), meaning that as long as there are good NIR observations of the object, the helium should be detectable when a double-detonation explosion occurs. A large sample with good NIR data gives a distinct advantage over those which chance upon a single object, particularly when those single objects have no NIR information. This not only increases the chance of finding one of these objects but also increases the robustness of any detection made. It also potentially allows for a preliminary comparison to be made between characteristics of any objects thought to have been caused by a helium shell detonation, such as the spectral type or stretch values, which is presently not possible with only two, possibly three, events modelled with such different helium shells and allows for a very rough estimate of how rare these events are by scaling up the sample size to be representative of a galaxy. This could provide insights into the types of events that observers should look for to find more helium shell detonations, which in turn could help to increase the sample size of these events and provide further insights into the progenitor systems of these objects.

The structure of this thesis is as follows; the sample selection and photometric and spectroscopic corrections of a sample of combined optical and near infrared spectra of SNe Ia around maximum light are presented in Chapter 2. Chapter 3 describes the method used to carry out velocity fittings to different spectral features in these spectra. The radiative transfer code TARDIS used to model the SNe Ia spectra and the methods used to create the synthetic spectra are described in Chapter 4. Chapter 5 contains an analysis of the sample and of the results from the line fitting carried out in Chapter 3. Chapter 6 presents the objects from the sample which were initially highlighted as possible helium shell candidates and the results of the helium shell modelling for two of these events and finally, Chapter 7 presents the conclusions of this work.

Chapter 2: Observations and Data Reduction

As discussed in Chapter 1, there are many theories and models which describe how helium shell detonations may occur and what effects these have on the SNe light curves and spectra. However, there are very few observations which potentially show any of these predicted features. The aim of this thesis is to try and tie the theory and observations together by searching through a large sample of SNe Ia to find possible helium shell detonations. This may not only increase the sample size of these objects, which is currently almost non-existent, but could also lead to a deeper understanding of how helium shell detonations affect physical properties of the SNe Ia (i.e. light curves and spectra) in nature and not just in theory.

In this chapter, observations of 33 SNe Ia are presented, including intermediate resolution spectra and corresponding light curves, from both observations and literature. 17 were previously published in Maguire et al. 2013 as part of an analysis of circumstellar material but this is the first time that their near infrared spectra have been analysed. The other 16 are previously unpublished. Sample selection, as well as spectroscopic and photometric observations are discussed in this chapter.

2.1 Sample Selection

All of the SNe Ia in this sample were chosen because they have intermediate resolution spectra which were taken around maximum light ($\sim$ –14 < t < +12 days, where t is the time the spectrum was taken in days since maximum light in the B-band). The proposed helium features are expected to appear at least a week before maximum light and to strengthen with time, hence the chosen time interval. Theory also predicts that these helium features will be stronger in subluminous SNe Ia but may also appear in 'normal' luminosity SNe Ia (Boyle et al. 2017). To test this, a variety of spectral sub-types were studied. Most of the SNe Ia are of the 'normal' sub-type, while a few are categorised as subluminous ('91bg-like') and over-luminous ('91T-like') spectra. The properties of the selected SNe Ia used in this study are found in Table 1. Further discussion of the sample properties is presented in Chapter 5 in the context of the helium detection constraints.

Table 1: Properties of the SNe Ia and their light curves

SN Name	Host Galaxy	Spec. MJD	Phase	B-Band Max MJD[a]	Heliocentric Redshift[b], z	A_v[b]	LC Source	Spectral Type
SN 2012cg	NGC 4424	56081.0	-0.8	56081.8	0.001538	0.057	Vinko et al. 2018	Normal
LSQ12dbr	Anon.	56110.4	-0.3	56110.7	0.0196	0.214	LSQ, LT+RATCam	Normal
PTF12iiq	2MASX J02500784-0016014	56178.3	-3.8	56182.1	0.02908	0.161	LT+RATCam, P48	Normal
SN 2012et	CGCG 476-117	56201.1	11.1	56190.0	0.02478	0.221	Amanullah et al. 2015	Normal
SN 2012fw	ESO 235-37	56174.1	7.2	56166.9	0.018586	0.097	FTS	Normal
LSQ12fuk	Anon.	56237.2	4.6	56232.6	0.0202	0.229	P48	Normal
LSQ12fxd	ESO 487 -G 004	56244.2	-1.9	56246.1	0.031242	0.069	LSQ	Normal
LSQ12gdj	ESO 472-G 007	56249.0	-4.4	56253.4	0.030324	0.064	SWOPE, LSQ	91T-like
LSQ12hzj	2MASX J09591230_0900095	56301.3	0.7	56300.6	0.029	0.183	LSQ	Normal
PTF12jgb	2MASXi J0415016_152053	56209.3	5.4	56203.9	0.02811	0.177	LT+IO:O, P48	Normal
SN 2012hd	IC 1657	56258.1	-6.7	56264.8	0.01218	0.073	FTN, LSQ	Normal
SN 2012hr	ESO 121-26	56283.1	-6.1	56289.2	0.007562	0.124	LCOGT Chile	Normal
SN 2012ht	NGC 3447	56293.3	-1.6	56294.9	0.003559	0.08	LT+IO:O	Normal
SN 2013aa	NGC 5643	56347.3	3.3	56344.0	0.003999	0.466	LCOGT	Normal
SN 2013aj	NGC 5339	56360.3	0.8	56359.5	0.009126	0.101	LT+IO:O, SWOPE	Normal
SN 2013ao	Anon.	56361.0	-6.8	56367.8	0.04	0.11	LT+IO:O	91T-like
SN 2013u	CGCG 8-23	56336.2	-1.6	56337.8	0.03417	0.08	LT+IO:O	91T-like
SN 2017ckq	ESO 437-G 056	57853.1	2.5	57850.6	0.0099	0.2077	ATLAS	Normal
SN 2017ejb	NGC 4696	57913.1	0.1	57913.0	0.00987	0.3007	LCOGT South Africa	91bg-like
SN 2017erp	NGC 5861	57920.2	-13.3	57933.5	0.0062	0.2945	ATLAS	Normal
SN 2017fgc	NGC 0474	57961.3	2.1	57959.2	0.008	0.0961	ATLAS	Normal
SN 2017gah	NGC 7187	57982.3	-2.7	57985.0	0.0089	0.0961	ATLAS	Normal
SN 2017guh	ESO 486-G 019	58021.3	-1.9	58023.2	0.015	0.0992	ATLAS	Normal
SN 2017fzw	NGC 2217	57983.4	-3.6	57987.0	0.0054	0.1178	LCOGT South Africa	Normal
SN 2017gvp	UGC 12739	58026.1	-2.8	58028.9	0.023	0.0837	ATLAS	Normal
SN 2016hvl	UGC 03524	57702.3	-7.8	57710.1	0.013	1.1997	ATLAS	91T-like
SN 2016ipf	CGCG 031-049	57725.3	-3.1	57728.4	0.021	0.0775	ATLAS	Normal
SN 2017azw	ESO 015-G010	57816.0	1.0	57815.0	0.016	0.0496	LCOGT South Africa	Normal
SN 2017awz	CGCG 125-030	57816.2	4.0	57812.2	0.022	0.062	ATLAS	91T-like/Normal
SN 2017hm	MCG -02-30-003	57775.3	2.9	57772.4	0.0213	0.1147	ATLAS	Normal
SN 2017hn	UGC 08204	57773.3	2.4	57770.9	0.0238	0.0899	ATLAS	91T-like/Normal
SN 2017yv	ESO 275-G 018	57797.2	2.8	57794.4	0.0156	0.2294	ATLAS	Normal
SN 2017bkc	2MASX J17503055-0148023	57816.4	5.4	57811.0	0.0174	1.1377	ATLAS	Normal
SN 2017cbv	NGC 5643	57837.2	-2.8	57840.0	0.004	0.173	LCOGT South Africa	Normal

a: Taken from Maguire et al. 2013, b: The total extinction values A_V of the objects, taken from NASA/IPAC Extragalactic Database (NED)

2.2 Spectroscopy

As discussed in Chapter 1.5, there are many difficulties to observing the possible He I features in the NIR region of spectra. To combat these effects, an instrument with good resolution in the NIR is required. The X-Shooter echelle spectograph on the Very Large Telescope (VLT) in Paranal, Chile covers a wide range of wavelengths, from $\sim$ 3000 Å to $\sim$ 24000 Å and has intermediate resolution (Vernet et al. 2011), making it a good candidate for this kind of investigation. The narrowest slit widths were used

to achieve resolutions of $\sim$ 9700, $\sim$ 18400 and $\sim$ 11600 for the ultraviolet-blue (UVB), visible-red (VIS) and near-infrared (NIR) arms respectively. The sample of object spectra presented in this paper were taken with X-Shooter, covering the regions where both the He I 10380 Å and 2μm lines appear and I reduced the data using the public X-Shooter Reflex pipeline (Freudling et al. 2013, Modigliani et al. 2014).

This pipeline fully reduces the spectral orders from the three arms on the X-Shooter instrument into a merged and calibrated one-dimensional spectrum of the object. The spectra from the three arms are treated separately until all the spectroscopic and photometric corrections (discussed in following chapters) are carried out and then the three arms are joined together to make a single spectrum for the object.

Following the spectral reduction with the pipeline, I used another program, Molecfit (Noll et al. 2013, Smette et al. 2015, Kimeswenger et al. 2017), to remove telluric features from the spectra. This program calculates a best fit model of the spectrum over a set of given wavelength ranges where telluric features occur (in this case, caused by the molecules H_2O, CO_2, CO, CH_4 and O_2) and uses this to remove such features from the full spectrum. This fit was carried out for the visible and near-infrared spectra for each object. The program did not apply any visible changes to the ultraviolet spectra as tellurics have very little effect in this spectral region and so Molecfit was not used on the UVB spectra. An example of a Molecfit fit spectrum is shown in Figure 2.

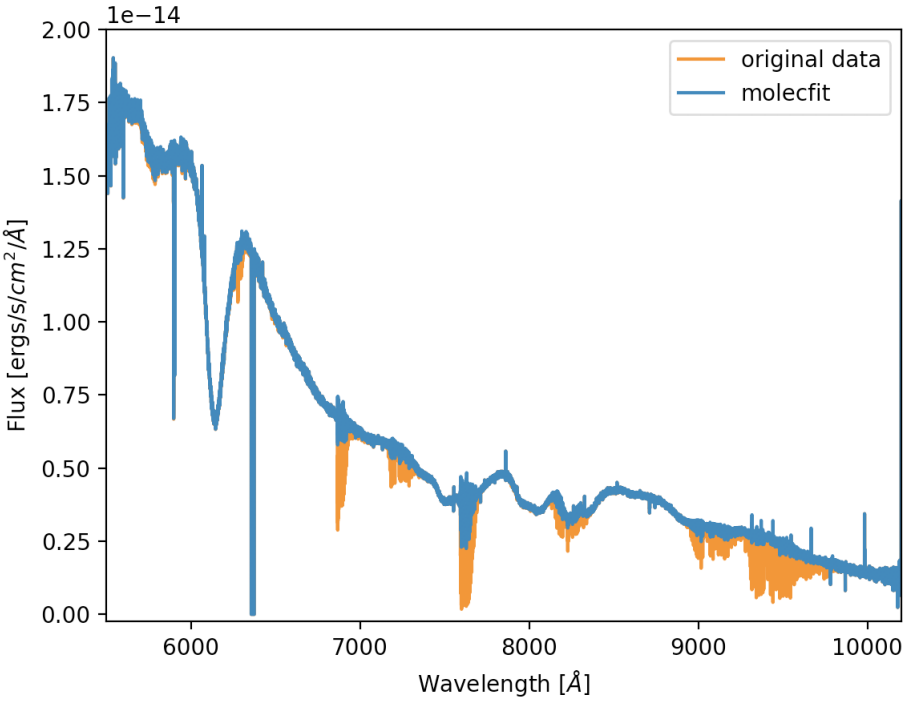

Figure 2: Uncorrected visible spectrum for SN 2012cg (orange) compared to the Molecfit corrected spectrum (blue).

Molecfit was able to fit all of the objects in this sample to some degree. It had a high success rate in the visible range of the spectrum and was able to fit all of the objects in this region. It had a slightly lower success rate in the NIR region, usually making very little change to the spectra unless the spectra were from nearby objects (i.e. bright) and had very little intrinsic noise, for example, SN 2012cg and SN 2017cbv. Three objects were not able to be fit in the NIR region with Molecfit. These were PTF12iiq, SN 2012et and PTF12jgb. The raw versions of the NIR spectra had to be used for these objects as Molecfit vastly worsened the quality of these spectra when trying to fit them. Overall, Molecfit was useful for cleaning the spectra of tellurics but was less successful on noisier spectra. Many of the spectra still retained some traces of tellurics in certain regions even after having been cleaned with Molecfit, for example, the O I 7773 Å feature (see Chapter 3.3) which made fitting of certain features difficult.

2.3 Photometry

Observed photometry was taken from a variety of sources for the SNe Ia in this sample: (i) the Palomar 48 inch (P48) telescope at PTF (Palomar Transient Factory), (ii) the 40 arcsec ESO Schmidt Telescope at LSQ (La Silla Quest), (iii) the 1m SWOPE telescope at Las Campanas observatory, (iv) the 2m Liverpool Telescope (LT), (v) the Faulkes

Telescope North (FTN) at Haleakala Observatory, part of the Las Cumbres Observatory Global Telescope (LCOGT) and (vi) the LCOGT 1m telescope array in Chile and vii) the LCOGT 1m array in Sutherland, South Africa. Two of the SNe Ia in the sample had poor or no photometric data and so light curves from the literature were used instead (SN 2012cg; Vinkó et al. 2018, SN 2012et; Amanullah et al. 2015). The sources for each of the SNe Ia light curves are shown in Table 1.

The PTF data was taken in the R band and reduced with the Infrared Processing and Analysis Centre (IPAC) Pipeline (see Maguire et al. 2013 and references within). The LSQ data was taken in the wide *'g+r'* filter and the SWOPE data was taken by the Carnegie Supernova Project II (CSP) in the natural system BVr filters. The LT data was taken in the *gri* filters by RATCam and Infrared-Optical:Optical (IO:O) optical imagers. The FTN data was taken with the Spectral Optical Imager in *gri* filters and the LCOGT data was taken in the Johnson-Cousins $UBVR$ and *'SDSS-like' gri* filters. For SN 2012cg, the data in Vinkó et al. 2018 was obtained from Konkoly Observatory, Hungary. The data at Konkoly was obtained in the Bessell $BVRI$ filters using the 0.6m Schmidt telescope. For SN 2012et, the data from Amanullah et al. 2015 was taken from the Hubble Space Telescope (HST) with the Wide-Field Camera 3 (WFC3) in the UVIS (*F225W, F275W* and *F336W* passbands) and IR channels (*F125W* and *F160W* passbands) and ground-based observations were taken by the Nordic Optical Telescope (NOT) with the Andalucia Faint Object Spectrograph and Camera (ALFOSC) in *U (#7), B (#74), V (#75), R (#76), i (#12)* filters.

I fit the light curves for all 33 SNe Ia using a Python function *curve_fit* (*curve_fit* 2018), which calculates the best non-linear least squares fit between a given model and the data and fits this curve to the data. Low order polynomials were used to estimate the magnitude of the photometry on the night the spectra were taken. These magnitudes were converted into flux densities using another Python package *pyphot* (Fouesneau et al. 2018). This package calculates the total flux that should be received through a given filter when given the AB or Vega magnitude of the object. The converted flux densities were then used to correct the observed flux of the spectra for losses through each filter (ignoring any i filters due to the different evolutionary shape of the light curves in this filter) by averaging the scale factors of the total flux in each filter calculated with *pyphot* to the measured flux through each filter and using this average scale factor to correct the entire spectrum. This worked well for the majority of the objects, except for SN 2012et and SN 2012cg which both had poor quality light curves. For these

objects, raw data was taken from the literature instead (Amanullah et al. 2015 and Vinkó et al. 2018 respectively) so that this method could also be tested on these two objects. When this was done, both agreed very well with the results in the papers, suggesting that this method worked well to correct the flux of the objects.

2.4 Extinction Corrections

I also corrected the spectra for extinction due to dust in the Milky Way. Dust scatters shorter wavelength light (i.e. towards the blue/UV) more than it scatters longer wavelength (red) light. This means that any dust present between the observer and the object can reduce the amount of blue light received and, by comparison, make the object appear redder than it really is. This process is known as 'extinction' or 'reddening'. Any contribution from the host galaxy to extinction has not been corrected for as this is unknown for most of the SNe Ia.

The extinction is corrected for with the equation

$$R_V = A_V / E(B-V) \tag{1}$$

where R_V is the ratio of selective to total extinction along the line of sight, A_V is the total extinction and $E(B-V)$ is the colour excess of the object. The A_V values shown in Table 1 for each of the objects were obtained from NASA/IPAC Extragalactic Database (NED). For most of the SNe, it was assumed that $R_V = 3.1$ as this is a typical value for the Milky Way (see, for example, Mandel et al. 2009, Marion et al. 2015), except for SN 2012et and SN 2017cbv which were reported to have lower R_V of 1.70 and 1.16 respectively (Amanullah et al. 2015, Sand et al. 2018).

There are many different models for the extinction correction, as it is not known exactly how the dust affects the spectrum at all wavelengths. Two of the most commonly used models are the Fitzpatrick (Fitzpatrick 1999) and the Cardelli, Clayton & Mathis (CCM; Cardelli et al. 1989) models. In this thesis, the CCM model was used.

The correction was calculated and applied with a Python package called *extinction* (Barbary 2016). The function calculates the extinction in magnitudes over a given wavelength range for given values of A_V and R_V and then applies these values to the given fluxes in the same wavelength range to produce new dust-corrected flux values.

2.5 Final Corrections

I joined the corrected spectra from the three separate arms of the X-Shooter instrument at this point into a single spectrum for each object, ranging from wavelengths in the UV through to the near-infrared ($\sim$2970-24500 Å). As the recorded fluxes of the objects showed variations between different arms of $\leq\sim$ 30% (this increased to $\leq\sim$ 60% in very noisy spectra such as PTF12iiq and SN2012et), the UVB and NIR fluxes were scaled down to match the VIS flux. This was done by calculating the average scale factor over a spectral region where the two spectra showed similar shapes (5540-5600 Å for the UVB/VIS crossover and 10090-10150 Å for VIS/NIR) and using this to scale the entire spectrum from one arm (i.e. UVB) to match the visible spectra.

The spectra were corrected for redshift using the values in Table 1, which were obtained from NED. The values were verified using classification spectra from the Weizmann Interactive Supernova Data Repository (WISeREP; Yaron et al. 2012).

The spectra were then smoothed with a function that carries out a boxcar average to remove noise from the data which helped to further reduce any contribution from telluric lines that Molecfit was not able to remove.

Chapter 3: Velocity Fitting

Estimates of spectral line velocities are extremely useful for a study of this nature. There are two other spectral lines which can appear in the same NIR region of the spectra as the predicted He I 10830 Å line; Mg II 10927 Å and C I 10693 Å. These can either cause features in this region to be misidentified or they can cause line blending and may 'hide' the helium feature. To counteract this, the velocities of known spectral features were measured to build up an idea of where lines were forming in the ejecta. In cases where spectral features could not be measured directly e.g. carbon, limits were placed on the velocity of this feature using the velocities of spectra which showed it.

3.1 Silicon II Velocities

The velocities were measured using the multiple Gaussian method discussed in Childress et al. 2013a and Maguire et al. 2014. A pseudo-continuum is defined visually by applying a linear fit between two user-defined regions either side of the feature to be measured. The spectral feature is then normalised to this pseudo-continuum. The wavelengths are transformed into velocity space using the relativistic Doppler formula (Equation 2) before the Gaussian fitting was performed to the spectral feature;

$$\lambda = \lambda_0 \frac{\sqrt{1 + \frac{v}{c}}}{\sqrt{1 - \frac{v}{c}}} \tag{2}$$

where λ is the observed wavelength, λ_0 is the rest wavelength, v is the measured velocity of the feature and c is the speed of light.

The feature was fitted with Gaussians as described below and then the start and end points of the pseudo-continuum were shifted by 0.2 Å within the user-defined regions, and the feature was normalised to this new continuum and fitted again. This was carried out over a region of at least 10 Å for each spectra and then the results of the fits were averaged to produce the final fits, shown in, for example, Figure 3. This meant that at least 50 runs, though usually ≥ 100 because the user defined region was usually around ~ 20 Å, were averaged to create each fit. This in turn meant that, particularly in noisier spectra when artefacts or tellurics could not be entirely removed from either side of the feature to be fitted, noise did not have an adverse effect on the fit as it was averaged out to produce the final model. It also meant that the user definition of the pseudo-continuum had much less of an effect on the final results than if the user had

simply chosen a single start and end point to define the continuum.

A double Gaussian model was used to fit the photospheric velocity Si II feature (PVF) to account for the two silicon lines (Si II 6347.11 & 6371.37 Å). Some other studies have only used one Gaussian in this fit as the data is not of high enough resolution to require both lines. Some preliminary tests were carried out comparing the single and double Gaussian method for this sample. It was found that the velocities varied by approximately 1000 km s^{-1} when using a double Gaussian compared to the single. For the purposes of this investigation, it was decided that the double Gaussian model would be used as the spectra are of high enough resolution and signal-to-noise ratio (S/N) to require both lines and the velocities given out by this method are consistent with values in the literature.

Following Childress et al. 2013a and Maguire et al. 2014, the widths of both PVF Si II lines were made to be equal and the relative velocity difference between the two lines was fixed throughout the fit (i.e. the distance between them was constant).

Initially, the lines were made to have the same amplitudes, as in the previously mentioned papers. However, there is still debate as to whether the ejecta from the SNe is in the optically thick or optically thin regime at this point in time. Maguire et al. 2014, Childress et al. 2014 and Pan et al. 2015 assume an optically thick regime but Silverman et al. 2015 assume optically thin and report little difference in the final results. Which regime the SNe is in determines whether the lines should be saturated or not and whether they should be assumed to have the same amplitudes (optically thick) or allowed variance in their strengths (optically thin).

Both options were tested in this investigation. Relative line strengths were taken from atomic data measured by the National Institute of Standards and Technology (NIST; Kramida et al. 2018) and were used to vary the amplitudes of the lines relative to each other to assume the optically thin regime. For the optically thick regime, they were forced to have the same amplitudes when being fitted.

Both methods gave very consistent velocity measurements for the Si II 6355 Å lines, with $<$ 100 km s^{-1} difference in the final values, which is in line with what was found by Silverman et al. 2015, but allowing the variance in the strengths was found to produce better fits for more complicated features, such as the Ca II NIR triplet (discussed in Chapter 3.2), which contains many lines that get blended. Therefore, it was assumed that the ejecta is in the optically thin regime throughout and the line strengths were varied in all fits for all features to ensure consistency in the recovered velocities, which

differs from the investigations of Childress et al. 2013a and Maguire et al. 2014. This model is shown in the left panel of Figure 3.

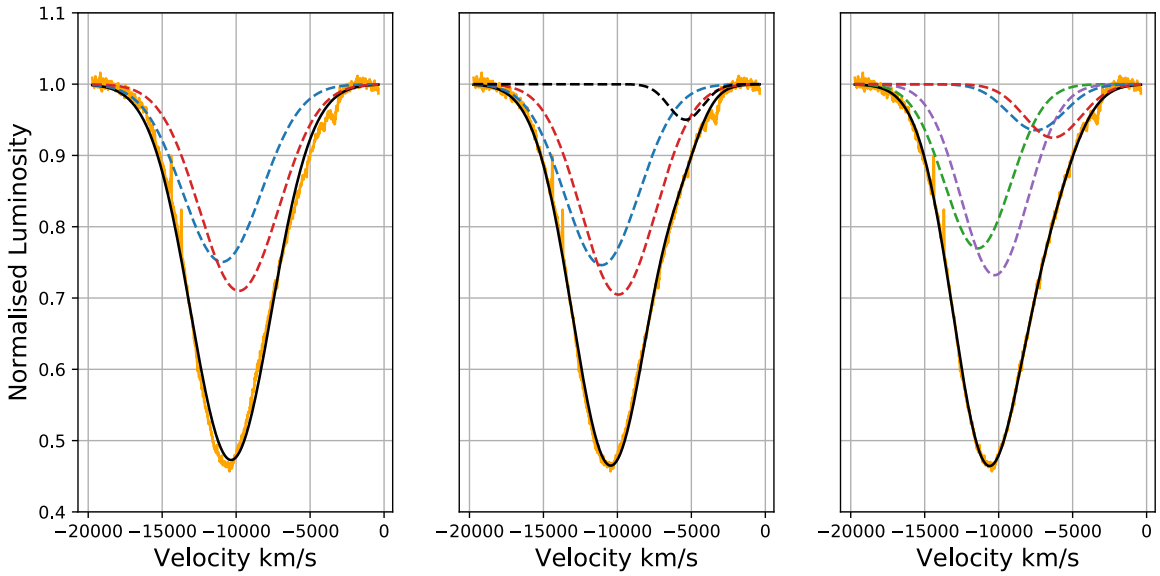

Figure 3: Example of Silicon 6355 Å fits. The dashed lines represent different lines included in the fit (blue and red; PVF Silicon, black; Carbon, green and purple; HVF Silicon). The solid black line represents the combined fit. The left panel shows the fit for PVF Si II only. The middle panel shows PVF Si II + C II. The right panel shows PVF + HVF Si II (right and left respectively).

Two variations of the simple Si model described above were also employed. The first was to allow for the possibility of C II 6580 Å, which is shown in the middle panel of Figure 3. This feature can either appear blended into the Si II 6355 Å as in this example, or can appear separately to the right of this feature, if the carbon velocity is lower, as shown in the middle panel of Figure 4 below. It has been found that approximately 30% of pre-maximum SNe Ia spectra contain optical carbon features (Parrent et al. 2014, Hsiao et al. 2015) and hence, this option was included as a model.

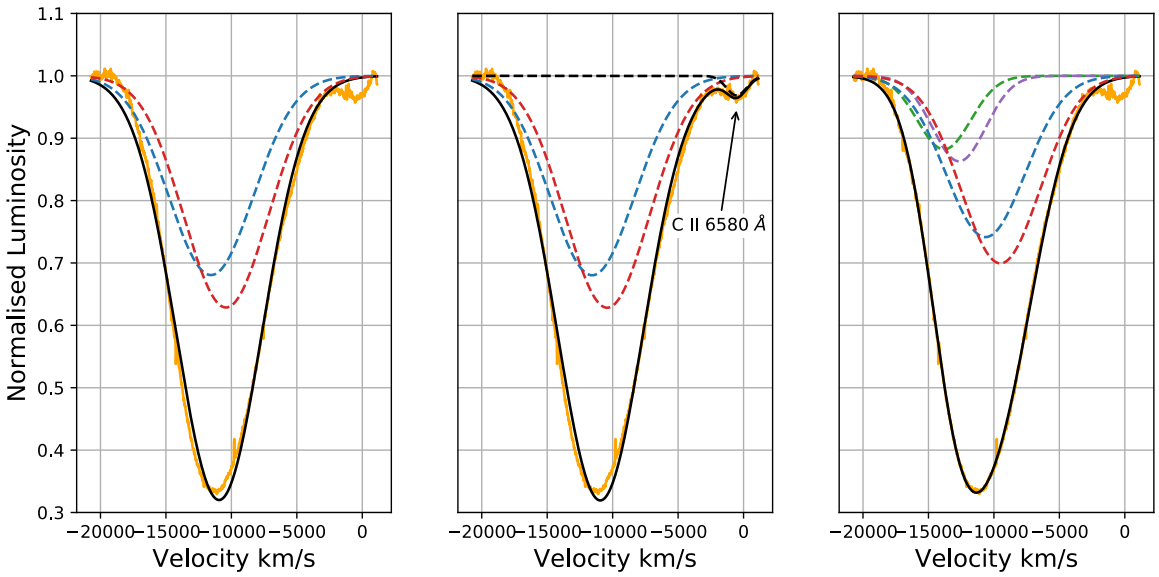

Figure 4: Example of Si II 6355 Å fits with C II 6580 Å exterior to the Si II feature for SN 2012ht. The dashed lines represent different lines included in the fit (blue and red; PVF Silicon, black; Carbon, green and purple; HVF Silicon). The solid black line represents the combined fit. The left panel shows the fit for PVF Si II only. The middle panel shows PVF Si II + C II. The right panel shows PVF + HVF Si II (right and left respectively).

The amplitude and width of the carbon feature were initially unconstrained, however, this led to the Si II 6355 Å feature of many of the SNe to be fit almost entirely by carbon, rather than silicon, which is incorrect. To remedy this, the amplitude and width were constrained, based on the values found when fitting the carbon feature to SN 2012cg, which had a reasonably small contribution from carbon in the feature but produced a better fit than silicon alone. The size of this feature is consistent with the size of the feature in the few SNe which have been claimed to contain carbon features in their spectra. Running the models again with these constraints in place allowed all of the features to be fit mostly by silicon and still allowed a handful of objects to have a carbon feature blended into the silicon feature. A few other objects had carbon features which were visibly separate to the silicon in the spectra at lower velocities, as previously mentioned. An example of this can be seen in Figure 4, compared to Figure 3 where the carbon is not a separate feature.

The second variation of the simple silicon model was to include the possibility of high velocity silicon features (HVF) which were blended into the feature. These are detached features which are separate to the PVF silicon and are usually found in very early spectra (for example, Marion et al. 2013, Barna et al. 2016). As with the PVF

silicon, the HVF features were also fitted with two Gaussians, which were made to have the same width. The Gaussians had different amplitudes based on their relative line strengths and the distance between the two lines were fixed.

To be recognised as a separate feature from the PVF silicon, it was decided that the HVF had to have velocities which were ≥ 5000 km s^{-1} higher than the PVF velocity. There is no defined value in the literature to separate these features so this one is arbitrary but is based on the high velocity Ca II features that have previously been studied. For values lower than this, the HVF and PVF Gaussians were visibly blended. There were a few SNe which had better fits when the HVF was included than PVF alone and all of these had separations of above 5000 km s^{-1} and so this was chosen as the separation value. An example of all of these models is shown in Figure 3: the left panel shows the model with only the two PVF Si II lines (red and blue dashed lines). The middle panel shows the fit which includes the PVF Si II and C II 6580 Å (black dashed line). The right panel shows the fit with both PVF & HVF Si II (green and purple dashed lines). The Si + C model was chosen as the best fit model for SN 2012cg by an information criterion (see Chapter 3.4). The width and amplitude of this feature was then used to constrain the C II contribution in the rest of the SNe within this sample to avoid over-fitting by C II, as mentioned previously.

All of the transformations and fitting methods described in this and following chapters were carried out with a new spectral fitting code, written specifically for this thesis. It was decided that writing new code to carry out these fits was important due the uncertainty of whether the ejecta is in the optically thick or optically thin regime and also due to the uncertainty of which elements contribute to these features (particularly in the calcium and oxygen features). It was important to have a code which could test all of these differences to get a better understanding of how to fit these features, rather than making assumptions on how to fit them beforehand and so this new code was written to test all of the possibilities.

3.2 Calcium II Velocities

Several other prominent features were also fitted using this multiple Gaussian method. The Ca II NIR triplet, which consists of the 8498 Å, 8542 Å & 8662 Å lines, was fitted rather than the Ca II H&K lines. The H&K lines appear around ~ 3700 Å, in the UV part of the spectrum. This area is dominated by iron-group elements (IGEs), which

create many lines and make it difficult to distinguish what each feature is comprised of, as many will have IGE lines blended in (Childress et al. 2013a, Zhao et al. 2015). In contrast, the NIR region has much fewer contaminants and should therefore be easier to fit, which in turn should provide more accurate velocities. Hence this region was chosen over the Ca II H&K region to estimate calcium velocities.

The NIR feature was fit with 6 Gaussians, 3 for PVF Ca II and 3 for the HVF. Unlike with the Si II, all of the NIR features were fitted with separate HVF as in the literature (see, for example, Maguire et al. 2014, Zhao et al. 2015, Barna et al. 2016). This is because the features were clearly separated and always by $\geq$ 5000km s^{-1}. As before, the 3 PVF features were required to have the same width, the relative velocity distances between the three lines were fixed throughout and the feature amplitudes were varied using the relative line strengths from NIST. This is shown in the middle panel of Figure 5, with the PVF & HVF Ca II shown as red and blue dashed lines, respectively.

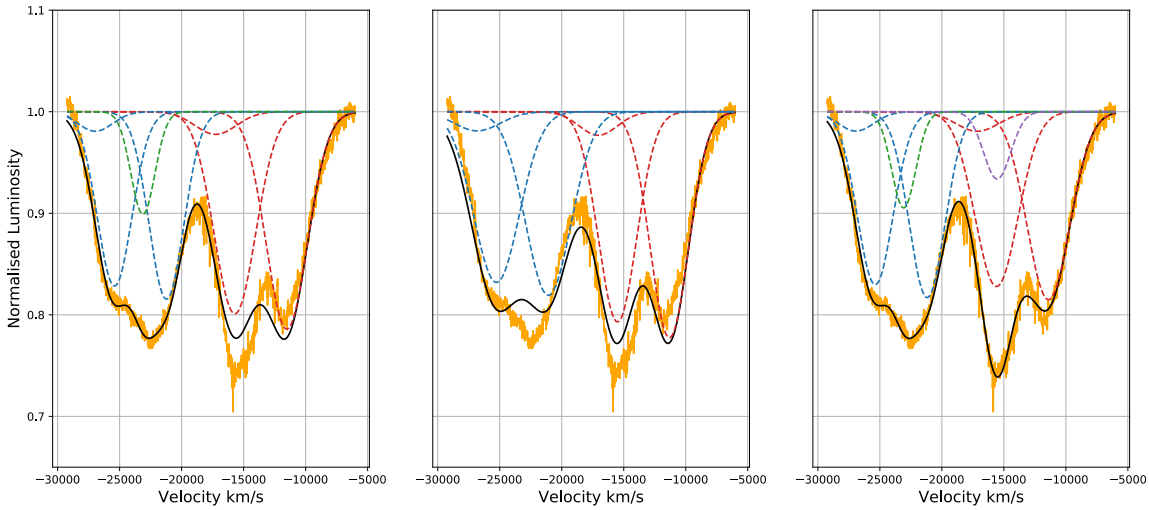

Figure 5: Example of Calcium NIR fits for SN 2012cg. The dashed lines represent different lines included in the fit (blue; HVF Calcium, red; PVF Calcium, green; Oxygen, purple; unidentified). The solid black line represents the combined fit. The left panel shows the fit for PVF (right) + HVF (left) Ca II + O I (smaller feature to the left). The middle panel shows PVF (right) + HVF (left) Ca II. The right panel shows PVF (right) + HVF (left) Ca II + O I (smaller feature to the left) + an unidentified feature (smallest feature to the right).

A second model was used which included 7 Gaussian features; the 6 Ca II lines and one for O I 8446 Å (see Figure 4 of Folatelli et al. 2012 and Figures 1 and 2 of Barna et al. 2016). The oxygen feature had a much smaller amplitude than the calcium which meant that its position in some fits was incredibly variable, depending on the initial position used. Therefore, oxygen was only included in the fit if the initial position of

the feature could be moved by $\geq$ 1000 km s^{-1} without moving the final position of the oxygen and this still allowed the HVF and PVF Ca II features to be separated by $\geq$ 5000km s^{-1}, regardless of whether it produced a better fit with the oxygen included. This fit is shown in the left panel of Figure 5, with the O I 8446 Å line shown as a green dashed line.

A few of the models required 8 Gaussians to perform a good fit to the feature; 6 Ca II, 1 O I and an unknown spectral feature. There is no mention in the literature of another feature other than calcium and oxygen appearing in this region. However, a handful of the SNe in this sample show a preference for this model over the Ca and O model (the method used to determine the 'best fit' model is discussed later in Chapter 3.4). The reason this other feature is not mentioned in the literature may be for three reasons; the first is that the quality of the spectra used in this sample is high and this may be the first time that this feature has been distinguishable from the other features in this region. The second is that in many studies, a single Gaussian is fit for the PVF Ca and another for the HVF Ca. This gives good estimates of the Ca velocity and so many previous investigations have used this method, which would negate any contribution from other much smaller features, meaning that perhaps this feature does appear in other data but has been overlooked. The third is that these handful of SNe which require the eighth Gaussian may be peculiar events, for example, perhaps there was more internal mixing within the progenitors of these SNe which led to different line forming regions within the ejecta from 'normal' SNe Ia, creating this feature which usually does not appear in the spectra. An example of these models is shown in the right panel of Figure 5 with the unknown feature plotted as a purple dashed line.

3.3 Comparison Oxygen I Velocities

The O I 7773 Å feature was also fitted to compare to the oxygen velocities obtained from the Ca NIR feature and to measure a velocity for Mg II 7890 Å as Mg II 10920 Å is a possible contaminant of the He II 10830 Å feature (Boyle et al. 2017). This feature appears to give more consistent velocities for the oxygen than those measured from the Ca NIR triplet. This is most likely due to the amplitudes of the respective features; in the Ca NIR triplet, the calcium dominates the fit as it has much larger widths and amplitudes than the O I. This means that the oxygen could be forced into being a narrower, shallower feature in the fit by the calcium, which in turn allows the fit more

freedom to position the oxygen. Even for the SNe which showed little to no variation in the final position of the O I, the O I could be consistently fitted to the wrong place in the spectrum because the feature is so small in comparison to the calcium, giving either much higher or much lower velocities than the standard. Contrary to this, the O I 7773 Å line in the feature around $\sim$ 7500 Å is the dominant feature and the widths and amplitudes of the other features in this region are similar to that of the O I, lessening this effect and giving more consistent results.

This feature was fitted with one of three models. The first model was used for spectra which were particularly affected by the strong telluric absorption in this region. It contained only 1 Gaussian to fit the feature, assumed to be O I. Any feature which was fit with this model was used to calculate limits on the oxygen velocity, rather than an estimate of the oxygen velocity. The second model had 2 Gaussians; one for a PVF of O I and one for Mg II. The last model added the option for fitting a HVF O I and had three Gaussians; the PVF O I, the HVF O I and the Mg II. The HVF was included as some SNe Ia have been claimed to exhibit high velocity oxygen in this region (Zhao et al. 2016, Barna et al. 2016). The distinction between the HVF and PVF feature was relaxed slightly from the $\leq$ 5000km s^{-1} used in the Si II and Ca II fits to $\leq$ 4500km s^{-1} for the oxygen fits. This was due to the telluric feature influencing the fits in this region. For three objects - SN 2013aj, SN 2017gah and SN 2017ejb - this distinction was not used. This is due to the velocity measurements of these three objects being used as limits, rather than direct measurements of the velocities. As explained later in this chapter, these three objects had very wide Mg II features and this forced the PVF O I velocities to appear higher than they probably are, lessening the distinction between the HVF and PVF to $\leq\sim$ 4000km s^{-1} for SN 2013aj and SN 2017gah and to $\leq\sim$ 3500km s^{-1} for SN 2017ejb. As the true PVF O I are probably lower than the limits provided for these three objects, in these cases only, the smaller separation between HVF and PVF features was allowed. Figure 6 shows the fits to the O I 7773 Å feature.

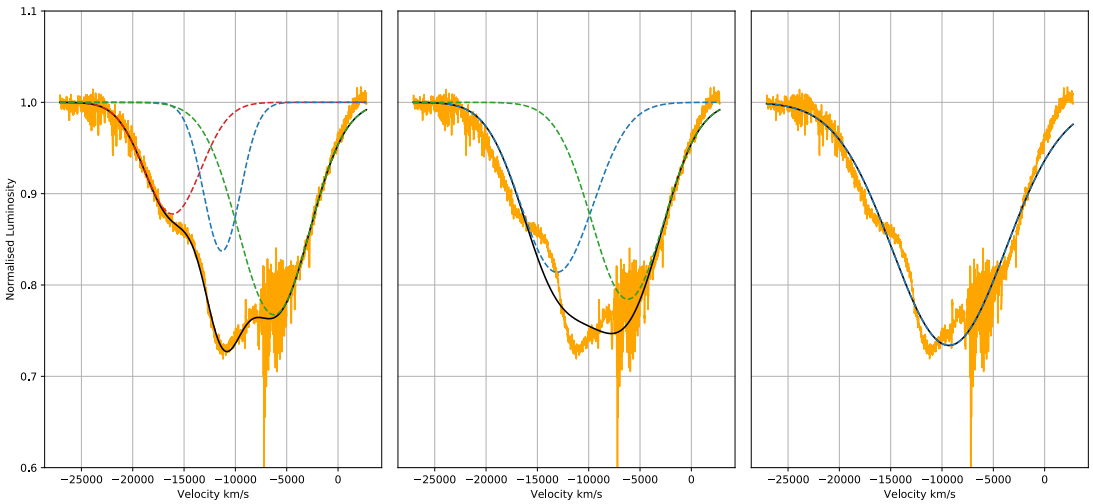

Figure 6: Example of Oxygen 7773 Å fits. The dashed lines represent different lines included in the fit (blue; PVF Oxygen, red; HVF Oxygen, green; Magnesium). The solid black line represents the combined fit. The left panel shows the fit for PVF (middle) + HVF (left) O I + Mg II (right). The middle panel shows the fit for PVF O I (left) + Mg II (right). The right panel shows the fit with PVF O I only (the blue dashed line is concurrent with the solid black line) used for features affected by the strong telluric in this region.

This region proved challenging to fit even in cases when the telluric could mostly be removed by smoothing. In some cases, the model with HVF oxygen was clearly the best fit, both visually and according to the information criterion used to determine the best fit model (see Chapter 3.4), and the fit required 3 Gaussians to fit all of the bumps in the spectrum. However, the Mg II feature was very wide and this caused the PVF O I to be narrower and pushed further left (to higher velocities) as shown in Figure A.1.

In these cases, there appears to be more structure to the feature i.e. extra 'bumps' compared to the same feature in other SNe (see Figure 6 as a comparison). This could be an indicator of other lines in this region which are not included as possibilities in the fits. Other Gaussians were not included in the models to test this as the literature has no suggestions of other features ever having been measured in this region, and unlike in the case with the Ca II fits, the models still fit relatively well without extra components. This however, leads to an Mg II feature which is wider than those measured in the rest of the sample and which becomes the main absorption feature in this region. This seems unlikely, particularly as this feature is meant to be comprised mainly of O I. It is suggested that if this fit was carried out with the inclusion of an extra component, this would lower the amplitude of the Mg II and narrow the feature, allowing the O I to widen and contribute more to the main absorption feature. In doing so, this would

move the wider peak of the O I component to lower velocities, which would be more consistent with the rest of the sample. Hence, these values, measured when the O I was forced to higher velocities by a too-wide Mg II component, were used as upper limits of the oxygen velocity.

In other cases, the fit could only be carried out with one Gaussian, assumed to be O I and was poor, meaning these velocities were also only included as limits. This was the case for SN 2012et, PTF12iiq and LSQ12gdj. An example of the fit for SN 2012et is shown in Figure A.2. The feature around 7500 Å for these SNe was wide and lacked the structure that this feature had in the other SNe in the sample (see Figures 6 and A.1 for comparison). Due to this, it was difficult to determine whether the feature was made of a blend of lines or was one broad feature. It is possible to move the oxygen to higher velocities than this single Gaussian velocity, depending on which of the other two models are used. In particular, it should be noted that as these three appear to have a different structure for this feature compared to the oxygen features of the other SNe in this sample, there may, for some reason beyond the scope of this thesis, be lines blended into this feature which do not appear in the rest of the sample. This may mean that the oxygen could also appear at lower velocities than those measured, making it impossible to tell whether these three velocities are indeed upper or lower limits.

3.4 Akaike Information Criterion

One way of determining how 'good' the fit of a model is to the data is by using an information criterion. Two of the most popular information criterion in statistics are the Akaike Information Criterion (AIC) and the Bayesian Information Criterion (BIC). For this study, the AIC was chosen over the BIC as the AIC has been shown to be better at choosing a 'good' model and minimises the risk of choosing a very bad model compared to the BIC (Burnham et al. 2002, Burnham et al. 2004, Vrieze 2012), making it ideal for this investigation.

The AIC, despite minimising the potential of choosing a bad model, has shown a tendency to over-fit data in smaller samples. To overcome this, a correction term has been added to the AIC to remove this bias (AICc; Hurvich et al. 1989, Burnham et al. 2002). The correction term is necessary in this study as the number of models to compare for the individual SNe is very small (< 4).

The AIC was calculated with a function which takes the data, the model used to fit the

data and the number of parameters required to create the model as input and uses these to calculate the 'goodness' of the fit. It does this by comparing the information gained by adding another parameter to the fit with the total number of parameters needed to make the fit and finds the best balance between these. This function, however, does not include the option for the AICc and so this extra term was added outside the function. The AICc scores were used in conjunction with visual inspection of the fits to choose the best model as in some cases, for example, with the oxygen in the Ca NIR feature, the AICc might suggest that the fit with oxygen is the best model but when visually inspected, the oxygen feature might appear at an unphysical velocity and so this fit would have to be discarded.

Chapter 4: TARDIS Radiative Transfer Modelling

The next step after the initial velocity analysis was to model the spectra with a radiative transfer code to try and match the estimations and provide further insights into the data. This chapter discusses TARDIS, the radiative transfer code used in this investigation and the setup of the models within this code. It is broken down into the initial model setup, which did not include helium but aimed to provide a base model for the SNe and the model which included a helium shell on top of the base model.

4.1 TARDIS Spectral Synthesis Code

There are a variety of different codes available which can be used to model SNe spectra, from those which take seconds or minutes to run and can be used for quick line identifications (for example, SYNAPPS or SYN++; Thomas et al. 2011) to computationally expensive codes which give a much deeper insight into the physics of the object, such as ARTIS (Kromer et al. 2009), SEDONA (Kasen et al. 2006) or more recently, JEKYLL (Ergon et al. 2018). Which code to use depends largely on the size of the sample to be tested and on how much information is required to be output from the model.

For this investigation, the spectral synthesis code TARDIS (Temperature and Radiation Diffusion in Supernova; Kerzendorf et al. 2014) was chosen. TARDIS is much less computationally expensive than other codes such as ARTIS but also gives more information than simple speedy line identifications which codes such as SYN++ produce. As the sample in this paper is large, computationally expensive models would take too much time to run for the entire sample. However, as this investigation is into helium features, it was necessary that the code used could still support the use of non-local thermodynamic equilibrium (NLTE) physics, which simple codes such as SYN++ do not. TARDIS was designed specifically for Type Ia SNe, unlike other codes which are designed for SNe in general and TARDIS also has an option for the required treatment of helium in its approximation (Kerzendorf et al. 2014, Boyle et al. 2017). For these reasons, TARDIS was chosen to model the spectra in this sample.

4.1.1 TARDIS Code Description

TARDIS is a 1D radiative transfer code which uses Monte-Carlo (MC) simulations of r-packets to model spectra, assuming spherical symmetry and homologous expansion

of the ejecta (Kerzendorf et al. 2014). The code creates a computational zone with an inner 'photosphere', defined by user inputs, which is assumed to emit blackbody radiation. The computational zone is divided into radial shells, each with their own density and abundance profiles. Indivisible packets of energy which act as photons, called r-packets, are created and placed at this inner boundary. The packets then move through the ejecta, either being scattered, absorbed and re-emitted or passed through to the next grid boundary, as the simulation iterates through improving values of radiation temperature T_R, inner temperature T_i and dilution factor W until convergence or the number of iterations input by the user is reached. The packets which reach the outer boundary during this computation are binned and used to produce an output spectrum. Packets which are scattered back to the inner boundary are assumed to be lost.

TARDIS also has an option for creating a virtual spectrum (Kerzendorf et al. 2014, Bulla et al. 2015). This is the same as the spectrum created by the propagation of the r-packets but typically with less MC noise, which is more useful for detecting blended features or those with much smaller amplitudes e.g. He I. Hence virtual TARDIS spectra were used throughout to compare to the data from the SNe.

The virtual spectrum is generated using v-packets, which are similar to the r-packets used to make the model spectrum. When an r-packet is about to change trajectory, either because it has been injected at the inner boundary, or has been scattered or re-emitted in one of the shells, the simulation is paused and a number of v-packets are created and propagated through the ejecta. They have the same properties as the r-packet which created them and are all assigned a different trajectory. As the purpose of the v-packets is to enhance the signal in the spectrum created at the outer boundary, none of the v-packets are given trajectories which will send them into the inner boundary. The v-packets are also strictly virtual and as such, do not interact with the ejecta through absorption or scattering the way the r-packets do. The optical depth τ_v of the v-packet along its trajectory is recorded as it reaches the outer boundary and each v-packet contributes to the luminosity of the frequency bin it is placed in, weighted by its optical depth (see Equation 21 in Kerzendorf et al. 2014).

TARDIS requires several input parameters to create a model spectrum; the luminosity at the outer boundary L_o, the time since explosion t_{exp}, a set of atomic data and density and abundance profiles for the ejecta. Several other parameters such as the treatment of excitation and ionisation can also be altered but for the purposes of this investigation, only the properties mentioned above were changed from the default

TARDIS settings. The atomic data used is the same as that of Kerzendorf et al. 2014. One important difference between the example file which comes with TARDIS and the files used to run these models is a command called *helium_treatment*. In the example TARDIS file, helium is not considered as an important feature and hence there is no helium in the example uniform abundance. This means that there is no requirement to tell TARDIS how to handle helium as it creates the spectrum. On the other hand, this is clearly important in an investigation such as this into the possibility of helium features. For all of the TARDIS models which contained helium (discussed later), the helium treatment was set to *recomb-nlte*. This method uses an approximation of NLTE which saves computational time by not carrying out full NLTE equations but also provides a deeper insight than simply assuming local thermodynamic equilibrium (LTE). This is necessary in the treatment of helium as its unique atomic structure means that it is not as well fitted by the LTE approximation which is used for other elements in SNe, as shown in Hachinger et al. 2012. The conditions in the ejecta mean that the lowest excited levels of He I are coupled more strongly to the He II ground state than the He I ground state. The *recomb-nlte* approximation takes this into account and treats the He I ground state as negligible, which is a valid approximation to make for weeks after maximum light, as shown in Dessart et al. 2015, and the He II excited state and He III ground state populations are calculated relative to the He II ground state rather than to the He I ground state (Boyle et al. 2017, Magee et al. 2018). Most of the He I excited states are treated with a crude NLTE approximation, known in TARDIS as *dilute-LTE* (Kerzendorf et al. 2014), except for the two lowest excited states of He I, which are important in their roles for creating the 10830 Å and 2μm lines, which include an extra $\frac{1}{\mathrm{w}}$ factor as these are metastable states. All of this allows a more accurate approximation of how helium should be treated when modelling spectra without requiring the same amount of time necessary to complete full NLTE equations (Boyle et al. 2017).

It should be noted that in this implementation of NLTE, TARDIS assumes that the helium is predominantly singly-ionised. In practise, the position of the helium relative to the radioactive ^{56}Ni would affect the strength of the helium features but in these models, it is assumed that the helium is singly-ionised regardless of the relative position between the two species. In the shell models used in this thesis, it would be expected that at least some of the helium and the radioactive species would be in similar locations in the shell, meaning that this is not a bad approximation to make. However, the most

important thing to note is that even if the helium and ^{56}Ni were located on top of each other, the TARDIS models will still most likely over-estimate the ionisation state. This means that regardless of the assumptions made on the position of the helium relative to radioactive species, the helium features recovered from these models should always be treated as upper limits.

4.2 Base Model Setup

Initially a uniform abundance profile was used, as this is the simplest approximation which can be made, alongside both exponential and power law density profiles. All combinations of these provided reasonable fits to some of the main features, such as the Si II and Ca II, but did not reproduce other important features, such as O I. Therefore, I used a custom abundance profile (and hence a custom density profile, as required by the setup of TARDIS) to test if it made an improvement to the models.

TARDIS takes in custom density profiles as an input parameter. For this study, three different density profiles were used. The density profile used for the 'normal' luminosity events in the sample was taken from Mazzali et al. 2014, who used the standard w7 model (Nomoto et al. 1984, Hachinger et al. 2009) for the prototypical 'normal' SNe Ia, SN 2011fe. This profile was used to model these events (not the sub-luminous events) as the 'normal' luminosity SNe most likely occurred around the Chandrasekhar mass limit and this is one of the common models for events which occur around this limit. A subluminous density profile was also used to fit the '91bg-like' events. This was taken from work done on fitting a subluminous event, SN 2005bl, in Heringer et al. 2017 (private communication). This subluminous density profile was altered later to provide a better match to some of the transitional objects in this investigation, though this alteration is discussed in Chapter 6.2.1 alongside these peculiar events. A comparison of these density profiles is shown in Figure 7, with the altered subluminous density profile shown here in orange for comparison.

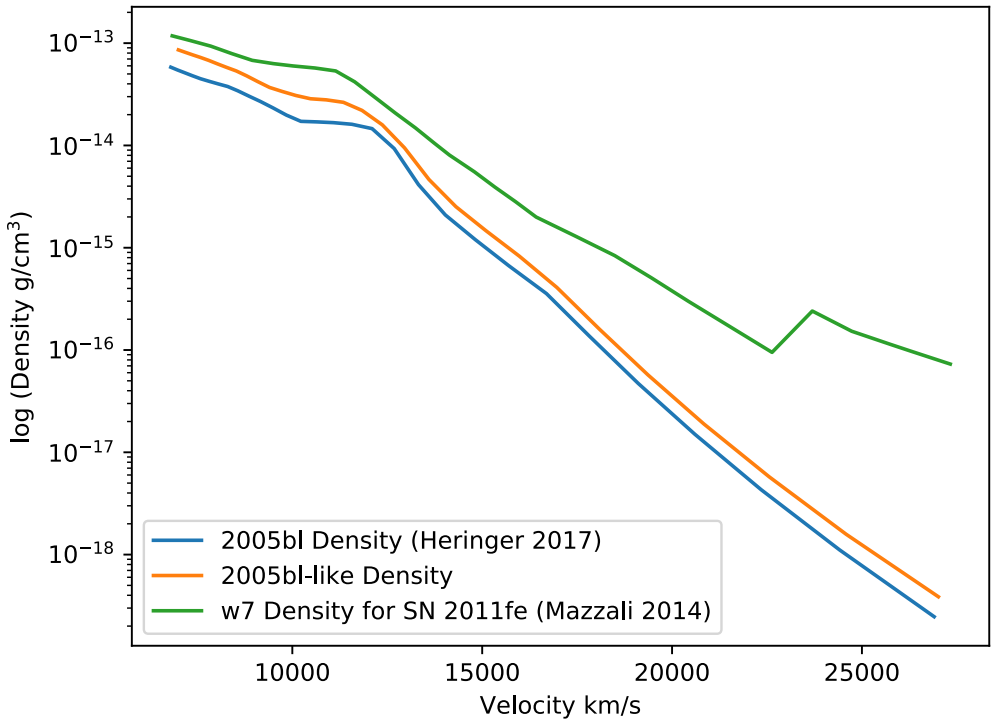

Figure 7: Comparison of w7 density profile used for normal luminosity SNe Ia from Mazzali et al. 2014 (green: top), the density profile for SN 2005bl from Heringer et al. 2017 (blue: bottom) and the altered density profile used to model the subluminous SNe in this investigation, based on 2005bl model from Heringer et al. 2017 (orange: middle).

TARDIS also accepts custom abundance profiles as input and in fact, if a custom density profile is used, a custom abundance profile then becomes a requirement of the code, rather than an optional input. Again, two abundance profiles were used; one for 'normal' events and one for subluminous events. These were both taken from Table 2 in Heringer et al. 2017 and were used as base models to test a range of luminosity and t_{exp} values to find a set of good matches for each SNe.

For this part of the parameter space study, the spectrum was initially treated as a black-body. The main concern was that the absolute flux of the model spectrum matched that of the real data in the optical region, around 3500 – 5500 Å. This region was chosen over the rest of the spectrum as most of the flux shows up in the optical around maximum light and TARDIS also had difficulties matching the NIR flux level, meaning that this region is less reliable an indicator of luminosity and t_{exp} than the optical.

The user can control the level of flux contributing to the final spectrum by altering the given luminosity and time since explosion in the TARDIS models. As expected, flux

increases as the given luminosity increases. t_{exp} has a slightly different effect on the flux levels. It controls the region where most of the flux can get through the ejecta to be observed, controlling the shape of the spectrum, rather than the amplitude. Up to and around maximum light (about ~ 19 days after explosion for a normal SNe Ia), the flux mainly shows in the optical region around 3500 – 5500 Å. After maximum light, optical flux begins to decrease again in this region as t_{exp} increases, as the nickel powering the flux output continues to decay and the peak moves further into the optical region of the spectrum (i.e. > 5500 Å). Thus, to ensure a good match to the amplitude of the optical peak, a wide range of explosion times ($7 \leq t_{exp} \leq 30$ days) and luminosities ($8.8 \leq L_o \leq 9.6$ $\log(L_\odot)$) that covered the usual parameter space for normal and subluminous SNe were tested.

The luminosities were changed in steps of 0.1 $\log(L_\odot)$. The full range of explosion times, increasing in steps of 1 day, were also tested for each given luminosity step i.e. for $L_o = 8.8$, t_{exp} was 7 days, then 8 days etc. until 30 days and then L_o was changed to 8.9 and the sequence was carried out again. All of these combinations were used as input for TARDIS, whilst keeping the same density and abundance profiles mentioned above and the models were then compared to the data to find a range of values which gave a good match to the amplitude of the optical region of the spectrum.

A 'good' match was determined by means of residuals between the model and the data in the optical in the range of 3750–5750 Å. An arbitrary limit was implemented so that only models with residuals less than 3×10^{42} erg s^{-1} were defined as 'good' ($\sim 30\%$ of the peak luminosity).

After a rough range of explosion times and luminosities to use in the models had been determined, the abundance profile was altered from that of Heringer et al. 2017 to try and match features in the spectra. The base abundances of all the elements were determined by running the TARDIS model and plotting the result against the spectral data. Abundances were adjusted according to the strength and position of the features in the model. If a feature was too strong, the abundances were lowered and vice versa. If it appeared shifted from the feature in the spectrum, the abundances were moved to different velocity shells to match the data.

Due to the nature of the TARDIS models, the model parameters returned from this type of investigation will generally not be unique. For example, it may be found that a certain temperature and silicon abundance gives a good fit but that reducing the temperature and increasing the silicon abundance also produces a similar fit and this

makes uncertainties in the model parameters very difficult to quantify. However, this does not mean that these models are entirely unhelpful or inaccurate. The abundances and temperatures used in the model are based on explosion models and nucleosynthesis so that the models have a reasonable degree of accuracy. The main advantage of using these kinds of models is that limits can be put on certain features or features can be excluded to stop the models becoming unrealistic so that when a good model is chosen, despite the lack of calculable uncertainties, it can be fairly certain that the model is still a reasonable estimate of what could be happening in nature.

The new abundances plus the helium abundances are shown in Table 2, after the discussion of adding helium to these base models. These are the abundances used for the rest of this investigation.

4.3 Adding Helium Shells

To simulate a thin helium shell on top of the base models, the helium abundance of the outer layers of the ejecta (i.e. the highest velocity regions) was increased so that these outer layers were comprised almost entirely of helium ($\sim 99\%$ He). These values were arbitrarily chosen (TARDIS automatically scales abundances so that the total abundance in a shell is equal to 1) and confined to a thin shell, spanning a velocity range $\sim 16966 - 27000$ km s^{-1}. Table 2 shows these initial values, which are essentially ratios of elements within each of the velocity shells of the TARDIS models. Changing these values does not affect the mass of the shell but alters the percentage of the shell which is made of certain elements. The values shown in Table 2 were altered throughout to increase the number of shells which contained helium, for example, to move from the 6 shell model which is shown in the table to the 7 shell model, the helium abundance in the 7th row from the bottom of the table was changed from 0 to 0.9897.

The thickness of the helium shell is also rather uncertain. Whilst most models are focused on thin helium shells, as these are thought to produce features most similar to the 'normal' category of SNe Ia (e.g. Boyle et al. 2017, Polin et al. 2019), there are also cases where a thick helium shell might be appropriate, such as SN 2018byg, which is claimed to have been caused by the explosion of a $\sim 0.75 M_{\odot}$ WD with a $\sim 0.15 M_{\odot}$ helium shell (De et al. 2019). Another possible detection of a SNe Ia with a helium shell in literature is SN 2016jhr (Jiang et al. 2017). This event was claimed to have been caused by a much thinner helium shell of $\sim 0.054 M_{\odot}$ on a larger WD of $1.03 M_{\odot}$.

At the time of writing, these are the two most promising candidates for helium shell explosions. Another recent SNe Ia, SN 2019yvq, was also modelled with a $0.04M_{\odot}$ helium shell on a $0.92M_{\odot}$ WD (Miller et al. 2020). This was reported as the best helium shell model for this event and reproduced several of the features of this peculiar event, such as the optical flash and r_{ZTF} colour evolution but failed to reproduce others, such as the g_{ZTF} and i_{ZTF} band evolution and the spectra of the object, making it uncertain whether this event could be explained as a helium-shell detonation.

All of the helium shell masses mentioned above for SN 2018byg, SN 2016jhr and SN 2019yvq are pre-burning helium shell masses. This means that post-explosion, there will likely be less helium left than the amounts mentioned here as the explosion will burn some of the helium into by-products. Therefore, these values represent an upper limit for the amount of helium left in the ejecta after explosion.

As there is a large variance in the helium shell masses of these events, a number of different shell thicknesses also had to be tested. However, in TARDIS, the mass of the helium shell that can be measured is the post-explosion mass, not the pre-burning mass. This means that comparison between the events from the literature and events modelled with TARDIS in this thesis is not direct, as previously mentioned, the helium shell masses in the literature are essentially upper limits of the post-burning mass whereas the values from TARDIS are the post-burning masses from the models used. Helium shells which left post-burning helium masses in the range of 0.0014 - 0.1651 $M_{\odot}$ were used to see how the effects of this compared to the spectra. This is a wider range than that tested in Boyle et al. 2017 and Fink et al. 2010, which is one of the papers the work of Boyle et al. 2017 is based upon. The reasons for this are discussed along with the results in Chapter 6.2.2.

The mass of these initial helium shells were then increased and decreased by 10%, 20%, 40%, 50%, 80%, 85%, 90% and 95% whilst maintaining the same ratio of helium to other elements in the shell (i.e. 99% as shown in Table 2). There were two extra models which were increased by 100% and 200% but these were not mirrored in the decreasing models because -200% gives a negative He abundance, which is not physical and -100% gives a He abundance of 0, which, while physical, will not run in TARDIS while the helium treatment is switched to *recomb-nlte* as there is no helium to treat.

Velocity (kms^{-1})	He	O	Mg	Si	S	Ca	Ti	Cr	Fe	Ni
6895 - 7000	0.0000	0.0000	0.0000	0.3334	0.0000	0.0167	0.0008	0.0008	0.1250	0.5233
7000 - 7183	0.0000	0.0000	0.0000	0.3135	0.0000	0.0209	0.0052	0.0052	0.0005	0.6546
7183 - 7377	0.0000	0.0000	0.0000	0.2751	0.0000	0.0254	0.0064	0.0064	0.0006	0.6861
7377 - 7581	0.0000	0.0865	0.0000	0.2824	0.0000	0.0247	0.0062	0.0062	0.0006	0.5933
7581 - 7796	0.0000	0.1863	0.0000	0.2311	0.0000	0.0233	0.0058	0.0058	0.0006	0.5355
7796 - 8024	0.0000	0.1907	0.0000	0.5703	0.0116	0.0238	0.0060	0.0060	0.0006	0.1907
8024 - 8266	0.0000	0.1855	0.0272	0.5548	0.0119	0.0232	0.0058	0.0058	0.0006	0.1855
8266 - 8523	0.0000	0.1828	0.0416	0.5466	0.0116	0.0228	0.0057	0.0057	0.0006	0.1828
8523 - 8797	0.0000	0.2206	0.0399	0.5914	0.0114	0.0210	0.0053	0.0053	0.0063	0.1050
8797 - 9089	0.0000	0.2206	0.0399	0.5914	0.0053	0.0210	0.0053	0.0053	0.0063	0.1050
9089 - 9400	0.0000	0.3656	0.0396	0.4583	0.0053	0.0208	0.0031	0.0031	0.0625	0.0417
9400 - 9734	0.0000	0.3656	0.0396	0.4583	0.0052	0.0208	0.0031	0.0031	0.0625	0.0417
9734 - 10092	0.0000	0.3656	0.0396	0.4583	0.0052	0.0208	0.0031	0.0031	0.0625	0.0417
10092 - 10478	0.0000	0.7255	0.0392	0.2064	0.0052	0.0206	0.0005	0.0005	0.0010	0.0010
10478 - 10894	0.0000	0.7255	0.0392	0.2064	0.0052	0.0206	0.0005	0.0005	0.0010	0.0010
10894 - 11346	0.0000	0.7255	0.0392	0.2064	0.0052	0.0206	0.0005	0.0005	0.0010	0.0010
11346 - 11836	0.0000	0.7255	0.0392	0.2064	0.0052	0.0206	0.0005	0.0005	0.0010	0.0010
11836 - 12370	0.0000	0.7255	0.0392	0.2064	0.0052	0.0206	0.0005	0.0005	0.0010	0.0010
12370 - 12955	0.0000	0.8741	0.0437	0.0690	0.0052	0.0115	0.0000	0.0000	0.0006	0.0011
12955 - 13598	0.0000	0.4227	0.0211	0.0334	0.0000	0.0056	0.0000	0.0000	0.0003	0.0006
13598 - 14308	0.0000	0.4227	0.0211	0.0334	0.0000	0.0056	0.0000	0.0000	0.0003	0.0006
14308 - 15096	0.0000	0.4270	0.0113	0.0337	0.0000	0.0056	0.0000	0.0000	0.0003	0.0006
15096 - 15976	0.0000	0.4270	0.0113	0.0337	0.0000	0.0056	0.0000	0.0000	0.0003	0.0006
15976 - 16966	0.0000	0.4270	0.0113	0.0337	0.0000	0.0056	0.0000	0.0000	0.0003	0.0006
16966 - 18086	0.9897	0.0000	0.0102	0.0000	0.0000	0.0000	0.0000	0.0000	0.0001	0.0000
18086 - 19366	0.9897	0.0000	0.0102	0.0000	0.0000	0.0000	0.0000	0.0000	0.0001	0.0000
19366 - 20840	0.9897	0.0000	0.0102	0.0000	0.0000	0.0000	0.0000	0.0000	0.0001	0.0000
20840 - 22558	0.9897	0.0000	0.0102	0.0000	0.0000	0.0000	0.0000	0.0000	0.0001	0.0000
22558 - 24585	0.9897	0.0000	0.0102	0.0000	0.0000	0.0000	0.0000	0.0000	0.0001	0.0000
24585 - 27014	0.9897	0.0000	0.0102	0.0000	0.0000	0.0000	0.0000	0.0000	0.0001	0.0000

Table 2: Abundance profile used in TARDIS models for SN 2017gah and SN 2017ejb, adjusted from Table 2 of Heringer et al. 2017. Any of the first 30 elements in the periodic table not mentioned here are assumed to have abundances of 0 at all points in the ejecta. Note, the values in this table are percentages, not the raw abundance values used. The values shown in this table are also adjusted later to include helium over a wider velocity range.

Chapter 5: Sample Analysis

This chapter aims to put the sample used in this analysis into context by comparing it to a wider range of SNe Ia from the literature (PTF sample from Maguire et al. 2014). A few of the most important properties of the light curves, such as the light curve

stretch, and other properties, such as spectral populations and host galaxy redshift are included in this comparison. Figures 8 and 9 show the stretch and redshift distributions of the sample. Stretch is a parameter which measures the width of the SNe light curve. Some SNe in this sample do not have a measured stretch value due to poor quality light curves. In both figures, the bins which contain the nine SNe with a feature in the NIR region (see section 6.1) around $\sim$ 10250 Å are marked with black dashed lines. Two of these nine which may have possible He I detections, SN 2017gah and SN 2017ejb, are marked in Figure 9. SN 2017gah is also marked in Figure 8 but SN 2017ejb is not as there is no stretch measurement for this event.

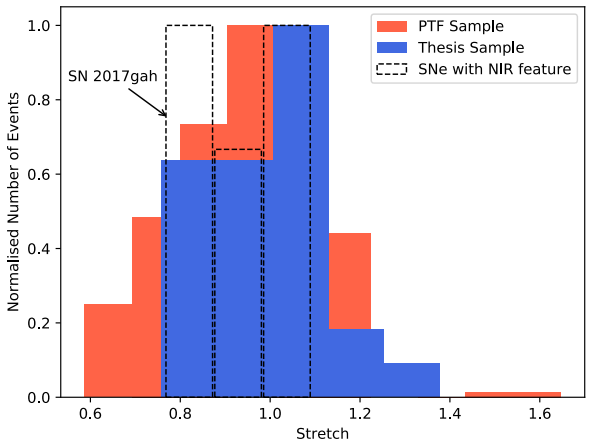

Figure 8: Histogram of light curve parameter stretch of the sample presented in this paper (blue) compared to the PTF sample from Maguire et al. 2014 (pink). The black dashed lines represent the 9 SNe with features around $\sim$ 10250 Å. SN 2017gah, a SNe with possible He I 10830 Å is marked on. SN 2017ejb, the other event with a possible He I detection, has no stretch value.

There appears to be no correlation between SNe which show a feature in the NIR and the stretch factor of the light curve. The eight SNe with this feature which also have stretch values appear in a wide range of bins. The SNe are rather evenly split across low (< 1.0) and high (> 1.0) stretch events with 4 and 4 SNe respectively in each group. The mean stretch value of the sample used in this investigation is 1.05 ± 0.06, which is consistent with that of the PTF sample, which has a mean stretch value of 1.00 ± 0.05.

In contrast, there may be a correlation between SNe in this group and redshift, as shown in Figure 9. All nine appear in the same low value redshift bin, meaning that they are all nearby (closer than $\sim$ 87Mpc). However, with such a small number of events, it is difficult to say for certain that there is any sort of correlation. Further work would

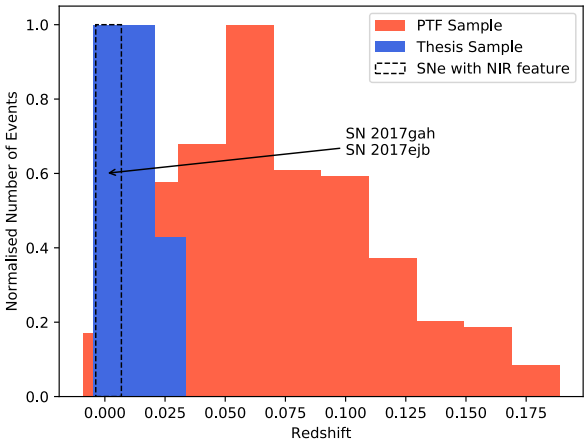

Figure 9: Histogram of host galaxy redshift of the sample presented in this paper (blue) compared to the PTF sample from Maguire et al. 2014 (pink). The black dashed lines represent the 9 SNe with features around $\sim$ 10250 Å. SN 2017gah and SN 2017ejb, two SNe with possible He I 10830 Å are marked on.

need to be done to increase the sample size to confirm this tenuous correlation.

If there is a correlation, it may be due to systematics rather than an intrinsic property of these events. There is a known problem in observational astrophysics, the Malmquist bias (Butkevich et al. 2005), which states that at higher distances, brighter objects are systematically more likely to be observed simply because they are easier to detect. This could be an explanation for why the SNe with this NIR feature appear at lower redshifts (lower distances). At least some of the SNe in this group are either classified as subluminous or are probable candidates for being transitional, subluminous events, despite their classification as a 'normal' luminosity SNe (see Chapter 6.2). This means that at higher distances, the same events become harder to observe and may be missed, leading to an apparent correlation between redshift and these events.

5.1 Line Fitting Results

5.1.1 Silicon Velocities

In this chapter, the results from the line fitting code described in Chapter 3 are shown. The velocity results from the silicon fits for the entire sample are shown in Figure 10 in blue (PVF) and orange (HVF), with velocities from the PTF sample in Maguire et al. 2014 shown in grey as comparison. It can be seen that most of the PVF Si II appears to come from a region deep within the ejecta, in a velocity shell of $\sim$ 10000–13000 km s^{-1},

around maximum light. The one point which appears above 18000 km s^{-1} (SN 2017erp) may at first glance appear inconsistent with the rest of the sample but is easily explained by the phase of the SN. This spectrum was taken almost two weeks (-13.3 days) before maximum light, approximately 4-5 days after explosion. At this epoch, all measured velocities are much higher because the lines are formed further out in the ejecta. As time progresses towards maximum light, these velocities fall to within the usual range and so SN 2017erp is still consistent with the rest of the sample (Brown et al. 2018). The PVF Si II velocities measured in this sample are also consistent with those measured in the PTF sample from Maguire et al. 2014 (grey dots).

The HVF Si II features also appear within a rough band around maximum light of $\sim$ 16000 – 18000 km s^{-1}. One HVF feature appears higher than the others, around 19000 km s^{-1} at 2.1 days (SN 2017fgc). This appears to be a high velocity event, as the PVF Si II also appears higher than the rest of the Si velocities ($\sim$ 14000 km s^{-1}). This event was modelled as one with HVF Si and though these features do not reportedly last until this phase, choosing either of the other Si models only worsens this discrepancy, pushing the PVF Si velocity up to over 15000 km s^{-1}. The reason for the high velocities of this particular event are beyond the scope of this investigation.

The uncertainties on the Si II velocities were calculated by taking the standard error in the positions of the Gaussian peaks of the $\sim$ 100 runs averaged to create each final model (see Chapter 3.1).

The values of the best fit models for the Si II 6355 Å feature for all SNe in this sample are shown in Table 3.

5.1.2 Calcium Velocities

The Ca II velocities are shown in Figure 11 in blue (PVF) and orange (HVF), with velocities from the PTF sample in Maguire et al. 2014) shown in grey (PVF) and yellow (HVF) as comparison. Again, there appear to be two distinct shells, with the PVF values ranging between $\sim$ 10000 km s^{-1} and 15000 km s^{-1} near maximum light. The HVF velocities also appear in a band between $\sim$ 15000 km s^{-1} and 25000 km s^{-1}, declining with time as with the PVF velocities. The 5000 km s^{-1} difference between these two bands is by definition of the HVF feature having to be at least 5000 km s^{-1} higher than the PVF to be counted as a separate feature. Again, SN 2017erp may appear inconsistent with the other velocities but this is again due to the early phase

of the spectrum.

The uncertainties in this figure are the standard error of the measured calcium velocity, calculated between the three models mentioned in Chapter 3.2. This is different from the method used to calculate the uncertainties in the silicon models, which took the standard error on the ~ 100 runs used to create each of the 3 separate models. This is because with the calcium feature, the certainty about what elements make up this feature is much lower than in the silicon models. While the silicon models gave fairly consistent velocities across the three models, the calcium models gave much larger differences due to the uncertainty of whether the much smaller O I and the unknown features should be included and their positions. The points with large uncertainties are models in which the position of the oxygen feature was flexible, which led to calcium velocities that were very different in comparison to the model without any other features and this was why a different method was used for the calcium uncertainties.

As with the Si II velocities, both the PVF and HVF Ca II velocities measured in this sample are consistent with the velocities measured for these features in the PTF sample (grey and yellow dots respectively).

The values of the best fit models for the Ca NIR feature for all SNe in this sample are shown in Table 3.

5.1.3 Oxygen Velocities

The oxygen velocities from the fits in Chapter 3.3 are shown in Figure 12. As mentioned previously, there were 2 cases in which the velocities were used as limits. These are shown as downwards arrows if the point is an upper limit or as triangles if the fit was poor, as described earlier. The uncertainties are calculated using the same standard error method as was used for the uncertainties in the calcium velocities, as again, this feature has a much less certain make-up than the silicon fits. There are no comparisons to the PTF sample for the oxygen velocities as this feature was not measured in Maguire et al. 2014.

Looking only at the limits in Figure 12, as this is where the O I velocity is relatively certain, the PVF and HVF features again appear in two distinct bands around maximum light, with the PVF features ranging from $\sim 10000 - 12500$ km s^{-1} and the HVF ranging from $\sim 14000 - 20000$ km s^{-1}. The one outlier not marked as an upper or lower limit is SN 2017bkc, with O I velocity of ~ 7600 km s^{-1} at a phase of +5.4 days. This

may be a particularly low velocity event, but given that SN 2017bkc fell within the 'normal' range in the silicon and calcium velocities, suggests that this is not true. It could also be that the value is lower because SN 2017bkc is at a later phase than other events (+5.4 days).

A possible explanation for this low velocity is over-fitting of the feature. As with SN 2012et, LSQ12gdj and PTF12iiq (marked with triangles in Figure 11, mentioned in Chapter 3.3), the feature around 7500 Å in SN 2017bkc is wide and devoid of any 'bumps'. Unlike with these other three cases, the spectrum of SN 2017bkc is much smoother, allowing for a better fit to be made to the feature. However, as can be seen in Figure A.3, there is still some remnant of the telluric line left in this feature when the fit is being carried out. This leads the AIC to choose the model with HVF O I as the best fit to try and match the shape of spectrum when this telluric is included. However, visually, it is difficult to say whether the best fit (solid black line) is truly fitting the spectrum in this region or if it is over-fitting to fit the telluric. If this noise could be removed, it may be found that the AIC would then decide that the HVF O I component is unnecessary and choose the PVF O I + Mg model as the best.

If this were the case, the O I velocity would increase to $\sim$ 11000 km s^{-1} and fall in line with the rest of the sample. However, with the present models, it is difficult to say for certain that this is the case and so, the model chosen by the AIC was used as the best fit, which gives this low velocity value.

The values of the best fit models for the O I 7773 Å feature for all SNe in this sample are shown in Table 3.

	Silicon II 6355 Å						Calcium NIR								Oxygen I 7773 Å					
	PVF		HVF		Carbon		PVF		HVF		Oxygen		Other		PVF		HVF		Magnesium	
SN	vel (km/s)	wid (km/s)	vel (km/s)	wid (km/s)	vel (km/s)	wid (km/s)	vel (km/s)	wid (km/s)	vel(km/s)	wid (km/s)	vel (km/s)	wid (km/s)	wid (km/s)	vel (km/s)	wid (km/s)	vel (km/s)	wid (km/s)	vel (km/s)	wid (km/s)	
SN 2012cg	10733	2487	-	-	16474	1557	11407	1726	21192	1435	15503	969	1092	11327	1730	16079	2770	10830	3548	
LSQ12dbr	11721	2553	-	-	-	-	12442	1829	16957	2369	16189	1492	-	12193	2023	16692	2715	10007	3158	
SN 2012fw	9922	2164	-	-	9733	1524	10022	2401	16819	1755	16496	1544	-	10840	3036	16366	1393	7954	3289	
PTF12iiq	12653	3862	18063	2082	-	-	13089	3394	18953	3698	14308	2906	-	15509	3133	-	-	-	-	
SN 2012et	12484	3527	-	-	-	-	10624	2682	16149	2777	11935	1846	-	7377	5838	-	-	-	-	
LSQ12fnk	10054	2721	-	-	-	-	10458	2031	15387	2898	14607	1465	-	10058	3884	16820	2112	6835	2422	
LSQ12fxd	11278	2894	-	-	-	-	11335	1093	22406	2593	-	-	-	11670	1564	17372	2705	10329	2508	
LSQ12gdj	11132	3008	-	-	-	-	-	-	-	-	-	-	-	10871	-	-	-	-	-	
LSQ12hzj	9292	2897	-	-	-	-	9625	1633	19253	2016	-	-	-	10144	1892	14619	2801	8671	2907	
PTF12jgb	9898	2720	-	-	-	-	9895	2044	15397	3403	-	-	-	9321	2168	14870	3356	7838	2710	
SN 2012hd	11595	3424	16878	1465	11225	527	14547	3403	24311	2252	13628	1604	1491	16659	1593	20905	1655	14663	2984	
SN 2012hr	12991	3799	-	-	-	-	12922	2481	21169	2477	10715	1019	1342	13828	2839	19753	1346	13751	3387	
SN 2012ht	11189	3216	-	-	10970	775	10643	1967	17072	3302	10908	1073	1212	11494	1939	16042	3485	11171	2500	
SN 2013aa	10545	2406	-	-	16662	1176	10476	1890	15581	2342	14354	1521		11188	2641	16928	2500	8706	3485	
SN 2013aj	11240	3284	-	-	-	-	10761	2156	15877	2752	17326	2549	1052	17178	1061	20965	2209	14875	3492	
SN 2013ao	10860	2240	-	-	9915	1132	11367	1202	20999	1834	-	-	-	10788	2974	17778	2608	10001	2568	
SN 2013u	9899	3283	-	-	-	-	9653	1913	17047	2719	-	-	-	15107	3305	-	-	11292	4500	
SN 2017cbv	10286	2908	15696	1711	-	-	10710	1573	20669	1995	16731	1308	1192	10246	2305	15777	1170	9466	2500	
SN 2017ckq	10319	2553	-	-	9606	669	10973	1904	15056	2159	14771	1259	-	9832	2464	15327	3538	8604	2802	
SN 2017ejb	9778	3295	-	-	-	-	12208	2728	20674	1588	11310	1582	2211	16252	1138	19837	2012	13828	3665	
SN 2017erp	18598	5938	-	-	13716	680	21238	5423	30109	2949	-	-	-	19167	2818	-	-	18895	2039	
SN 2017fgc	14081	3802	19045	2301	-	-	12890	2678	19955	2506	20363	1390	2071	10263	3956	17092	2998	8337	2092	
SN 2017gah	11114	3560	16148	1955	-	-	10737	2793	18187	2175	12880	2184	1569	12134	3371	16072	2235	10698	3500	
SN 2017fzw	12227	3680	17514	2208	-	-	12124	2931	19758	2371	15509	1660	1328	17394	2687	-	-	18596	4310	
SN 2017gyp	11072	2913	-	-	-	-	11147	2040	21399	2186	15787	610	1583	11827	1690	16522	3272	11553	3000	
SN 2016hvl	-	-	-	-	-	-	-	-	-	-	-	-	-	-	-	-	-	-	-	
SN 2017azw	10667	2678	-	-	-	-	10633	1204	22990	1594	11107	3457	1061	11932	4188	-	-	8693	3143	
SN 2016ipf	10439	3636	-	-	-	-	9461	2135	18243	2834	9270	1105	2095	11248	2763	15926	3892	8711	3208	
SN 2017hn	11183	2006	-	-	-	-	11502	1544	16565	2643	16741	2146	1432	12253	2975	17683	1162	9170	3571	
SN 2017hm	10254	2643	-	-	-	-	10347	2128	20784	1695	14985	1108	2606	11448	2901	17132	1425	8408	2976	
SN 2017yv	11882	3024	-	-	-	-	12015	2396	18080	2167	14289	1752	-	12484	3842	-	-	8072	3134	
SN 2017awz	11558	2029	-	-	-	-	11775	1292	17584	1596	-	-	-	11932	4188	-	-	8693	3143	
SN 2017bkc	11823	3177	-	-	-	-	9939	2323	14957	2337	12900	2038	915	7612	4014	14041	2317	5197	2687	

Table 3: Best fit Gaussian values for Si II 6355 Å, Ca NIR and O I 7773 Å features measured using the initial velocity fit method explained in Chapter 3.

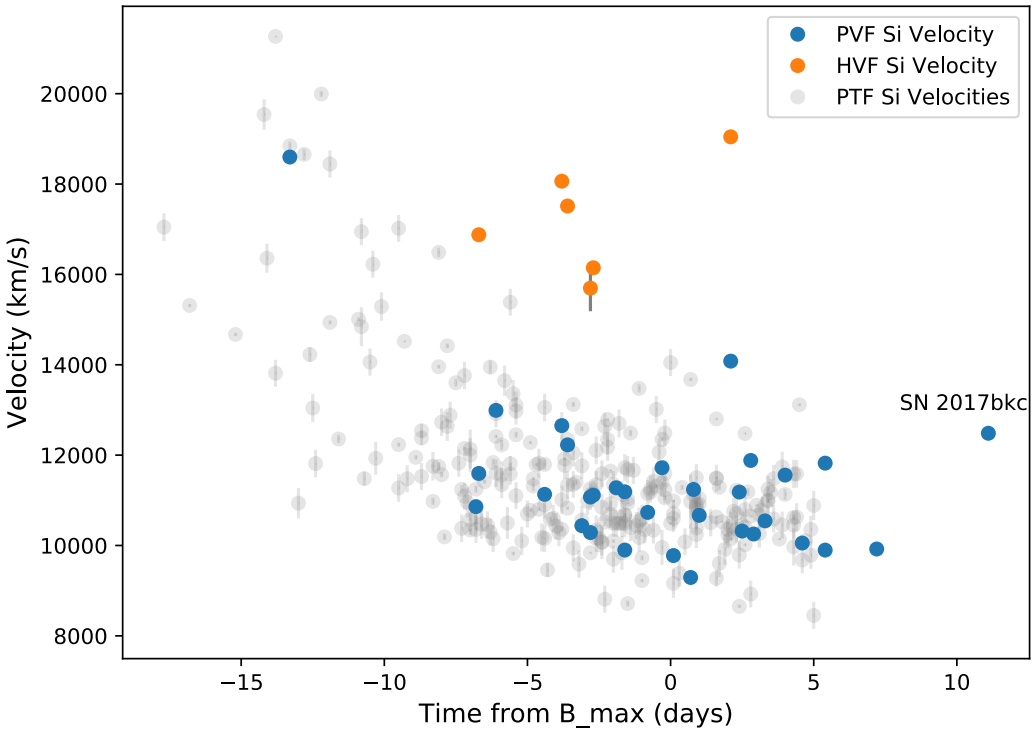

Figure 10: Si II velocities for the sample, measured from the 6355 Å feature. The orange points show the HVF features. The blue points show the PVF features. The grey points show the PVF velocities from the PTF sample in Maguire et al. 2014. Error bars are included on all points but are too small to be seen in most cases.

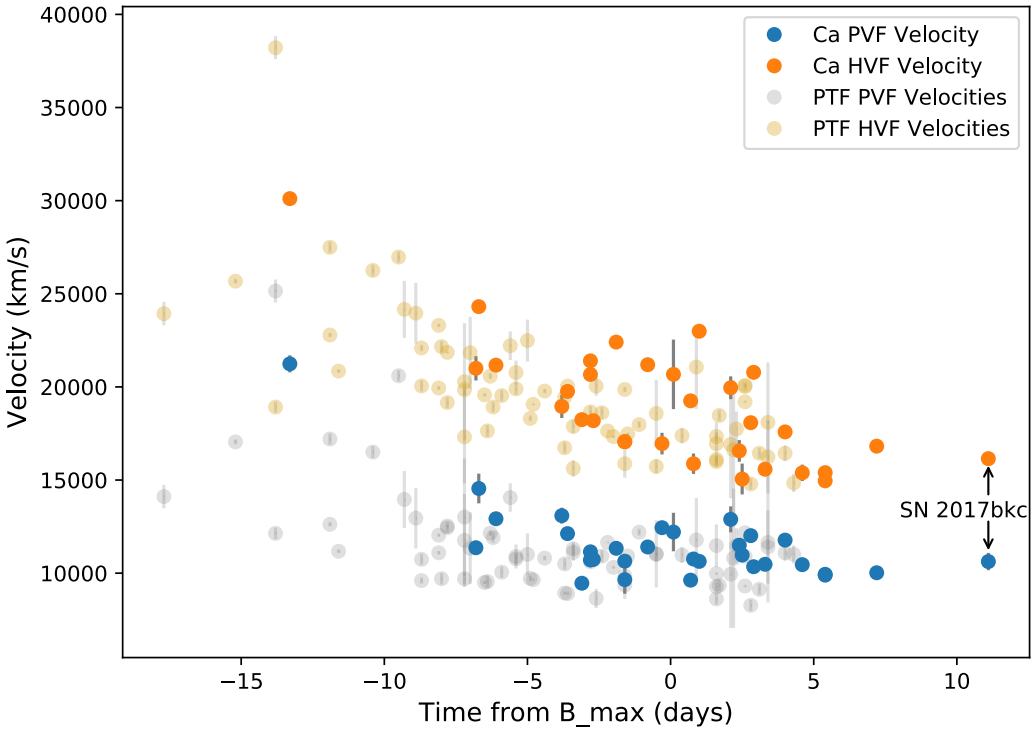

Figure 11: Ca II velocities for the sample, measured from the NIR feature. The blue points show the PVF features. The orange points show the HVF features. The grey points and yellow points show the PVF and HVF velocities respectively from the PTF sample in Maguire et al. 2014. Error bars are included on all points but are too small to be seen in most cases.

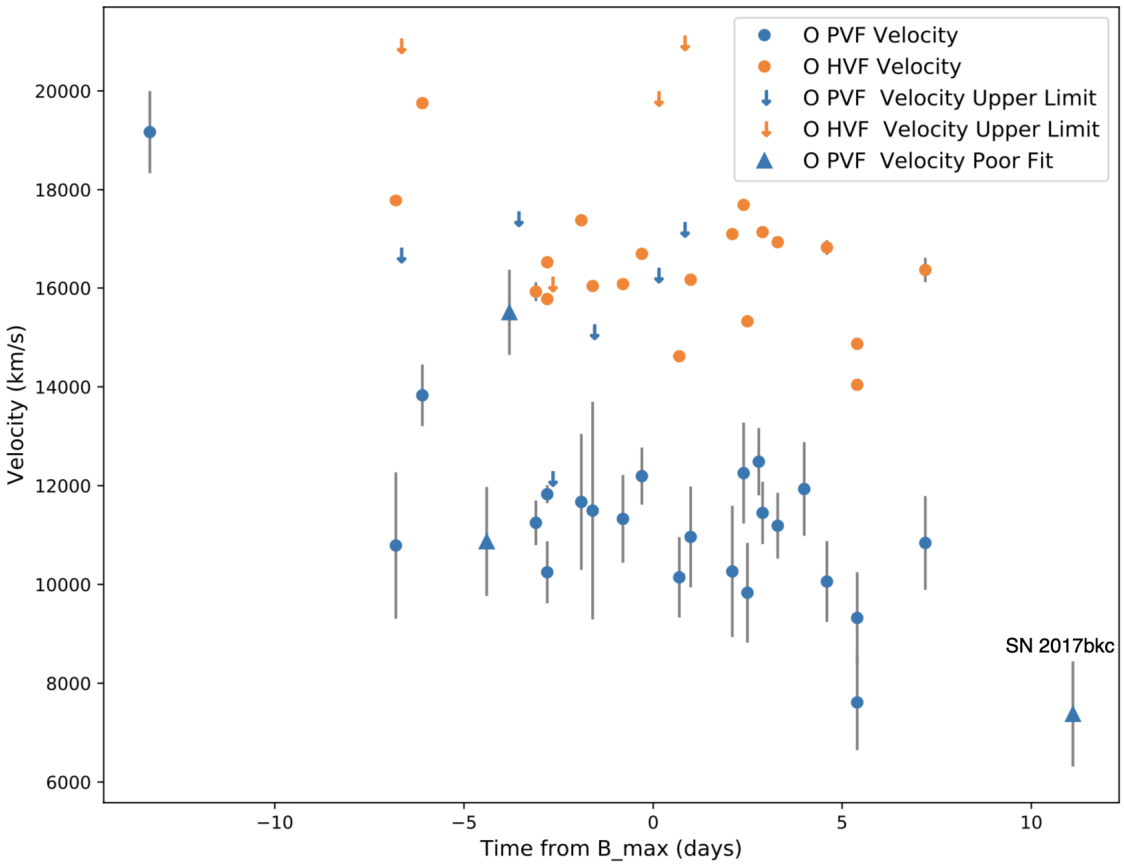

Figure 12: O I velocities for the sample, measured from the 7773 Å feature. The orange points show the HVF features. The blue points show the PVF features. The orange arrows show upper limits for HVF features. The blue arrows show upper limits for PVF features. The blue triangles show the three events (LSQ12gdj, PTF12iiq and SN 2012et) for which only one Gaussian could be fit to the feature, assumed to be O I. As these are very different structures to the other oxygen features, it is unclear whether these are upper or lower limits on the velocity.

Chapter 6: Constraining the Presence of Helium

This chapter discusses the possibility of helium features detected within the sample. Firstly, I discuss the SNe which showed features around 10250 Å, where the He I feature is expected to show, which were selected as possible candidates for having helium features and the initial velocity fits for these events in Chapter 6.1. Two of these objects, SN 2017gah and SN 2017ejb, were highlighted by the initial velocity fits to potentially contain helium in the NIR feature being investigated and the velocity fits to these objects are discussed further in Chapters 6.1.1 and 6.1.2 respectively. The setup for TARDIS models for these two objects and the results of these models compared to the observed spectra are discussed in Chapter 6.2.

6.1 Possible He I

For all 33 SNe in the sample, the region around where the He I 10830 Å is suggested to appear was visually inspected in search of visible features ($9500 < \lambda < 12000$ Å). 24 of the SNe showed no features in this region. 9 did have features which fell within this wavelength range and were preliminarily selected as candidates for possible He I features. The visible and near infrared spectra of these 9 objects are shown in Figures 13 and 14 respectively. Examples of the NIR region that was searched visually for features are shown in Figure 15 for events which show features in this region and those that do not for comparison. The full sample is shown in Figure A.4.

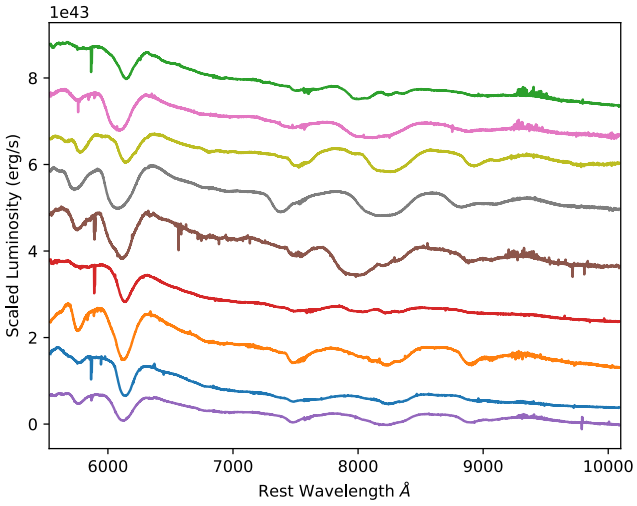

Figure 13: The visible region of the 9 spectra with features around 10250 Å. From top to bottom, they are SN 2017cbv (green), SN 2012hr (pink), SN 2017ejb (gold), SN 2017gah (grey), SN 2012hd (brown), SN 2012cg (red), SN 2013aj (orange), SN 2013aa (blue) and SN 2012ht (purple).

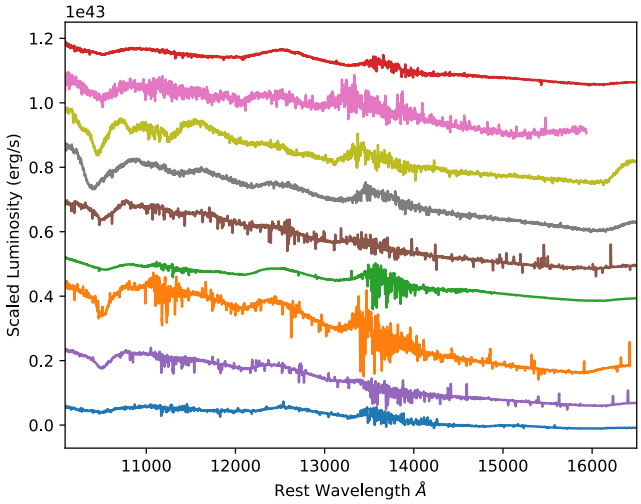

Figure 14: The near infrared region of the 9 spectra with features around 10250 Å. From top to bottom, they are SN 2012cg (red), SN 2012hr (pink), SN 2017ejb (gold), SN 2017gah (grey), SN 2012hd (brown), SN 2017cbv (green), SN 2013aj (orange), SN 2012ht (purple) and SN 2013aa (blue). SN 2012hr is cut off sooner than the other spectra because there was more noise in this region of its spectrum than for the other objects.

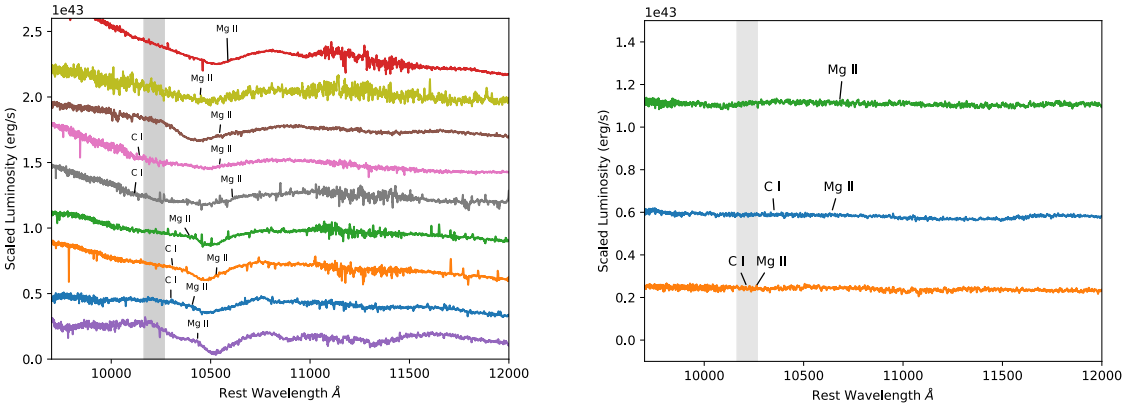

Figure 15: Left: The NIR region where He features may appear for the 9 SNe with possible detections. The grey shaded region represents the area predicted for where the He features would show from Boyle et al. 2017. The lines mark where magnesium and carbon features are expected to appear, based on their measured velocities for the same features in the optical region of each spectra. From the top down, these SNe are SN 2017cbv (red), SN 2012hr (gold), SN 2017gah (brown), SN 2012cg (pink), SN 2013aa (grey), SN 2013aj (green), SN 2012ht (orange), SN 2012hd (blue) and SN 2017ejb (purple). Right: The NIR region where possible He features may show, for 3 SNe which clearly show no features in this region. From the top down, these are SN 2013fuk (green), SN 2017erp (blue) and 2012fw (orange).

For the 9 candidates, this NIR feature was fit in a manner similar to the fitting of the other features in Chapter 3. A pseudo-continuum was defined by visually choosing a region of ~ 20 Å either side of the feature and applying a linear fit across the feature, then normalising the spectral feature to this pseudo-continuum. The start and end points of the user-defined region were then shifted by 0.2 Å and a new linear fit was applied and the feature normalised again. This was repeated a minimum of 50 times across the feature to reduce the effects of noise and of the user's choice of the start and end positions for the feature to be fitted.

For each of the 50+ runs, the normalised feature was then transformed into velocity space using Equation 2 and the feature was fit with Gaussians. Two models were used for this; one which fit a single Gaussian to the feature, simulating only a single element creating the feature and a model with two Gaussians, simulating a blend of elements. The Gaussians were fit to each of the 50+ runs for each SN and the results were then averaged to find the best overall fit to the feature.

The AICc scores combined with visual inspection of the features were again used to determine the best fit models. Out of the 9 SNe, 7 preferred the single Gaussian model (SN 2017cbv, SN 2013aj, SN 2012ht, SN 2012hr, SN 2013aa, SN 2012cg and SN 2012hd) while 2 showed preference for the double Gaussian model (SN 2017gah and

SN 2017ejb). Examples of these fits are shown in Figures 16 and 17, which illustrate one of the seven events which showed preference for the single Gaussian model (SN 2012cg) and one of the two which showed preference for the double Gaussian models (SN 2017ejb) respectively.

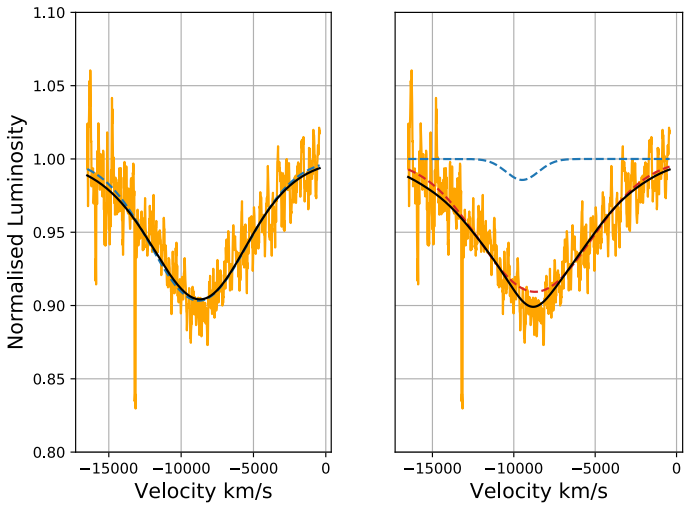

Figure 16: Example of the single and double Gaussian fitting to the NIR feature of SN 2012cg. This SN is one of the seven events which showed preference to the single Gaussian model.

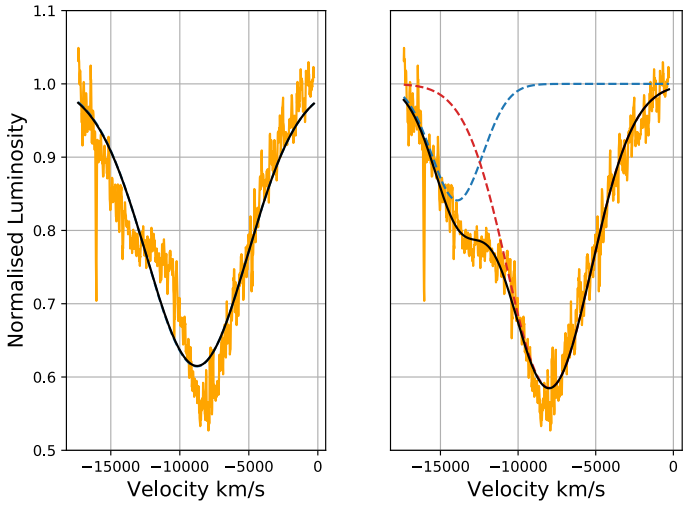

Figure 17: Example of the single and double Gaussian fitting to the NIR feature of SN 2017ejb. This SN is one of the two events which showed preference to the double Gaussian model.

For the single Gaussian fits, the velocity of the feature was estimated by assuming that it was caused by carbon, magnesium and helium respectively for the C I 10693 Å, Mg II 10927 Å and He I 10830 Å lines. These velocities were then compared to the measured magnesium and carbon velocities (when available) from the other features

of that SNe and also to the range of values for these features from the total sample to determine the most likely constituent.

It was found that the carbon velocities for all 7 SNe were systematically too low to cause this feature (< 6050 km s^{-1} compared to the measured values of > 9500 km s^{-1} for carbon from this sample). The magnesium velocities from this feature were far more consistent with both the measurements from the individual SNe and the sample as a whole ($\sim 10000 < v < 12540$ km s^{-1}). The helium velocities had no measured comparison values but if the feature had been comprised of He, the velocities would have been around or slightly lower than the photospheric velocities of other features ($\sim$ 8000 – 9200 km s^{-1} for the helium compared to $\sim$ 10000 – 13000 km s^{-1} for photospheric Si II). The only one of the seven objects which came close to this velocity band was SN 2012hr, which would have a velocity of 9862 km s^{-1} if the feature was made of helium. However, the photospheric velocity of silicon in this event is higher (12991 km s^{-1}) and so for this particular event, the helium velocity of almost 10000 km s^{-1} is still too low to be considered viable, as it too is below the photospheric velocities of other features in the same event. This would not be expected to be the case if the helium comes from a shell surrounding the white dwarf. The photospheric elements come from deep within the WD structure and tend to have lower velocities than the elements near the surface of the WD, hence it would be expected that the helium would not have velocities lower than these features. Indeed, Boyle et al. 2017 predicts He velocities much higher than those mentioned here ($\sim$ 16000 – 19000 km s^{-1}). Following this logic, it was determined that the feature in the NIR around $\sim$ 10250 Å for these 7 SNe was most likely made by the Mg II 10927 Å line.

For the 2 of these 9 SNe which showed a preference for the double Gaussian model, a similar approach was used to determine the most likely constituents of these features; both Gaussians (called 'red' and 'blue' for the right and left Gaussians respectively) were assumed to be comprised of carbon, magnesium and helium to estimate the velocities.

6.1.1 Potential He I in SN 2017gah

For SN 2017gah, the C I velocities were again too low for both features ($\sim$ 8050 km s^{-1} and $\sim$ 4145 km s^{-1} for the 'blue' and 'red' Gaussian respectively). The 'red' Gaussian has a velocity of 10638 km s^{-1} if it was made by the Mg II 10927 Å line, which is

consistent with measured Mg II velocities of 10698 km s^{-1} from the O I 7773 Å feature for SN 2017gah. This leaves the 'blue' side of the feature, which is not compatible with being Mg II or C I, to be a possible identification of He I at a velocity of 11868 km s^{-1}. This is lower than the values predicted in Boyle et al. 2017 but is consistent with a possible He I detection, blended with Mg II in SN1994D (Meikle et al. 1996). However, it is suggested that the possible He I from this SN comes from α-rich freeze-out, rather than a thin helium shell on the surface and so may be a less accurate comparison for the helium velocity. The discrepancy between the velocities found here and those of Boyle et al. 2017 are discussed later in Chapter 6.2. These fits and their respective velocities are shown in Figure 18.

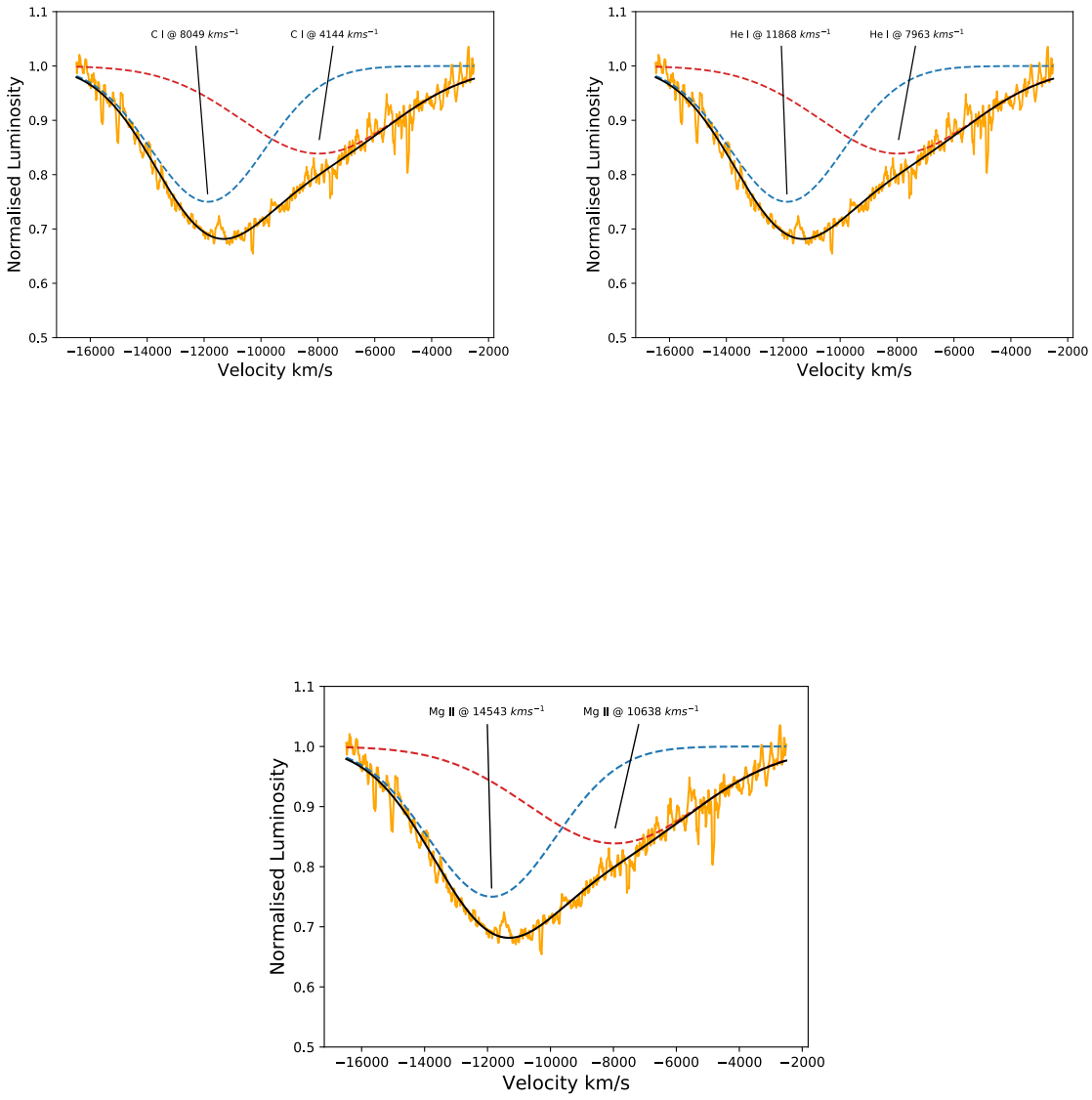

Figure 18: Velocities of the 'red' and 'blue' Gaussians described in Chapter 6.1.1 for SN 2017gah if they were made of carbon (top left), helium (top right) and magnesium (bottom).

6.1.2 Potential He I in SN 2017ejb

The fits with velocities of the different possible features for SN 2017ejb are shown in Figure 19. For SN 2017ejb, the velocity of the carbon is plausible for the 'blue' feature. It was measured to be $\sim$ 10100 km s^{-1}, which is consistent with the measurements of C II in the optical region of a few of the SNe in this sample ($\sim$ 9600 – 13720 km s^{-1}). However, SN 2017ejb was not found to have optical carbon or any other definite NIR carbon features to corroborate the existence of carbon in its spectrum (see Figures 13 and 14) and so this feature is ruled out. The measured velocity of Mg II in SN 2017ejb was 13828 km s^{-1}. This is used as an upper limit rather than an accurate estimation of the Mg velocity in this SN due to the width of the fitted Mg II feature (see Chapter 3.3). Using this as an upper limit rules out the possibility of Mg II for the 'blue' Gaussian as this would require a velocity of 16597 km s^{-1}, well beyond the upper limit. This again leaves the 'blue' side of the feature as a possible He I detection as it is inconsistent with being either Mg II or C I. This would yield a He I velocity of 13922 km s^{-1}, which is still below those predicted by Boyle et al. 2017.

If Mg is responsible for the 'red' Gaussian, the velocity would be 10666 km s^{-1}, which is consistent with both the upper limit and the measured Mg II velocities from the other SNe. The 'red' side of this feature is also inconsistent with being C I or He I as both produce velocities below those of the photospheric features in this SNe (4172 km s^{-1} and 7991 km s^{-1} for C I and He I respectively, compared to 9778 km s^{-1} for photospheric Si II), making Mg the most likely cause of this side of the feature.

Based on these arguments, it was preliminarily suggested that the feature around 10250 Å in both SN 2017gah and SN 2017ejb was produced by a blend of He I 10830 Å and Mg II 10927 Å.

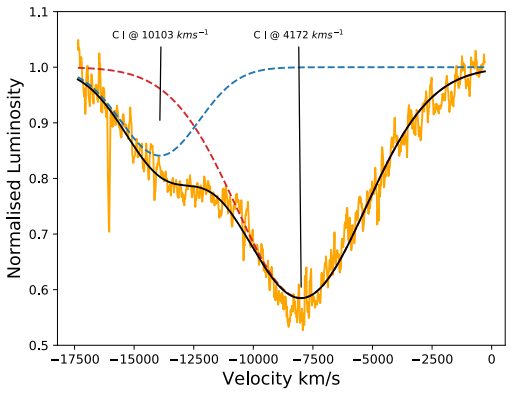

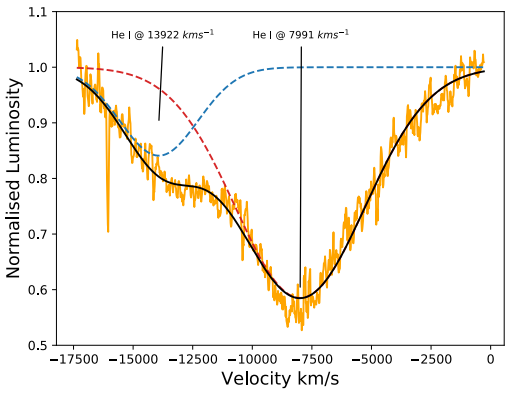

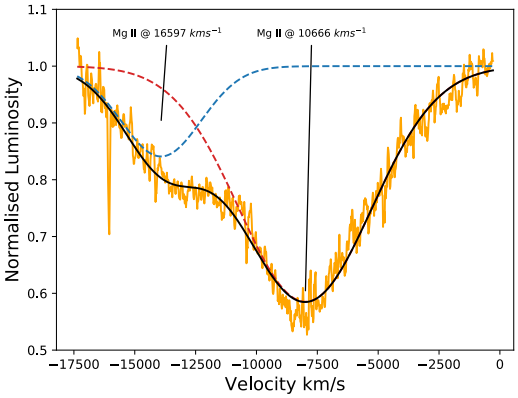

Figure 19: Velocities of the 'red' and 'blue' Gaussians described in Chapter 6.1.2 for SN 2017ejb if they were made of carbon (top left), helium (top right) and magnesium (bottom).

6.2 TARDIS Modelling of SN 2017ejb and SN 2017gah

TARDIS modelling, as mentioned earlier, is an important step in confirming or denying the plausibility of the NIR feature in SN 2017gah and SN 2017ejb as being caused by He I. As discussed in Chapter 6.1, the velocities do not match those predicted by the latest double detonation models but also do not appear to be either Mg II or C I. If TARDIS models can reproduce this feature with He, it lends a robustness to the estimates made by the line velocity fits, despite the discrepancy with the original models.

As shown in Table 1, SN 2017ejb was classified as a subluminous '91bg-like' SNe. SN 2017gah was classified as 'normal', however, its spectrum appears to have qualities similar to that of a '91bg-like' Ia, such as stronger Si II 5972 Å and O I 7773 Å (Heringer et al. 2017, Taubenberger 2017) as can be seen in Figure 13. These classifications were made using the Supernova Identification code (SNID; Blondin et al. 2007). SNID compares a given spectrum to templates of other SNe Ia spectra of all known sub-types and returns the type(s) with which it finds a best match. However, SNID can sometimes misidentify an event for two main reasons. The first is that the number of templates for well-defined classes such as 'normal' SNe Ia is much higher than peculiar sub-classes, meaning that the code is more likely to pick a template from one of these well-defined classes. The second is that SNID scales the given spectrum to match the templates, meaning that smaller details such as the Si II 5972 Å strength can be overlooked by the code if it is not a particularly strong feature. Both of these facts mean that although SN 2017gah was identified as a 'normal' SNe Ia, it may in fact be a 'transitional' event i.e. SNe that fall somewhere in the gap between '91bg-like' and

'normal' SNe, an idea which is reinforced by its spectral features.

6.2.1 Density Profiles

As mentioned in Chapter 4.2, a few density profiles were tested when running the TARDIS models, due to the possible subluminous nature of the two objects being tested. subluminous density profiles at different epochs were taken from Heringer et al. 2017, which in turn were based on the work of Hachinger et al. 2009. The two density profiles in Heringer et al. 2017 which were closest to the true epochs of the two objects were for 14 days and 21.8 days after explosion, compared to $\sim$ 16.3 days and $\sim$ 19.1 days for SN 2017gah and SN 2017ejb respectively. For both SNe, neither profile matched perfectly. The 14 day density profile led to too much flux in the UV region and features being at slightly too high velocities or showing too weakly. The 21.8 day profile matched the spectrum better, producing roughly the right amount of flux in the UV/VIS and features of the right strengths but producing features at velocities which were too low to match the spectra. To resolve this, three new density profiles were created for 16, 18 and 20 days to bridge the gap between these two. These were weighted averages between the 14 and 21.8 day density profiles so that the earlier profiles were more similar to the 14 day profile and later profiles were more similar to the 21.8 days. Of these three new profiles, the 20 day matched both spectra better than any of the others. This profile is the '2005bl-like' profile shown in Figure 7.

As SN 2017gah was classified as a 'normal' luminosity event, the normal luminosity density profile (Mazzali et al. 2014 in Figure 7) was also tested. The 11fe density profile did not provide a good match to SN 2017ejb but did, however, appear to provide a good match to SN 2017gah. It was able to recreate the strengths of the features reasonably well, although some such as the oxygen, were fit less well than when using the subluminous density profiles. However, the main discrepancy between the model using the 11fe density profile and the spectrum for SN 2017gah was in the NIR region around the possible He I feature. Using this density profile meant that little to no helium showed up in the NIR region, which is what is expected from previous 'high-mass' models in Boyle et al. 2017. It also reduced the strength of the Mg II feature so that the match between the model and the observed spectral feature around 10500 Å was poor. On further investigation, using the 11fe density profile to model SN 2017gah meant that while the main features appeared in the right velocity ranges and at the

right strengths, they were often made of the wrong ionisation state. For example, the Si II 6355 Å feature is expected to be made from singly ionised silicon (Si II as the name suggests) but in this case, the majority of the feature was being made by doubly ionised silicon (Si III). Using the higher density profile increased the temperature within the model and ionised elements to higher degrees than are expected in the ejecta. Hence, while this model appeared visually to create a good match to SN 2017gah, it was disregarded and the subluminous density profile at 20 days past explosion was used to fit both SN 2017gah and SN 2017ejb.

The final fits for SN 2017ejb and SN 2017gah using the '2005bl-like' density profile and the abundances found in Table 2 are shown in Figure 20 and Figure 21 respectively. Both SNe are fit relatively well by this combination. The model for SN 2017gah produces an excess of flux in the UV region before $\sim$ 4500 Å and the model velocities are slightly lower, but otherwise agrees reasonably well with the data and produces features in the right ionisation states, unlike with the 11fe density profile.

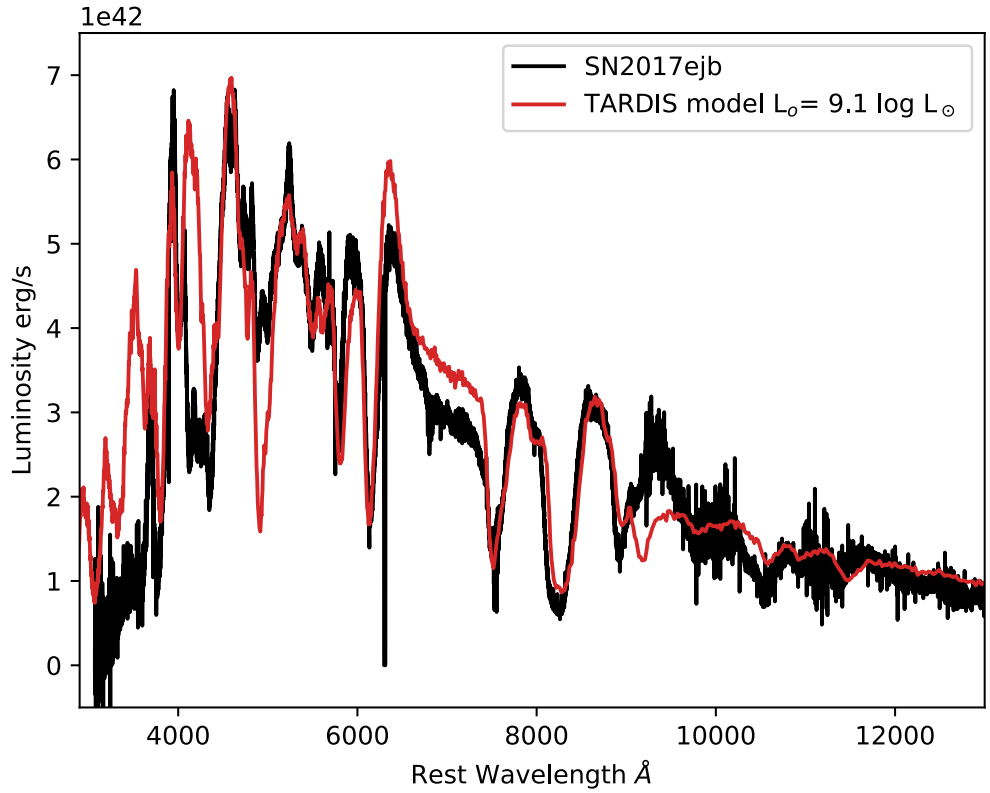

Figure 20: Full Spectrum of SN 2017ejb (black) compared to TARDIS model (red) made with abundance profile in Table 2, t_{exp} = 20 days, subluminous density profile in Figure 7 (2005bl-like) and L_o=9.1 log $L_\odot$

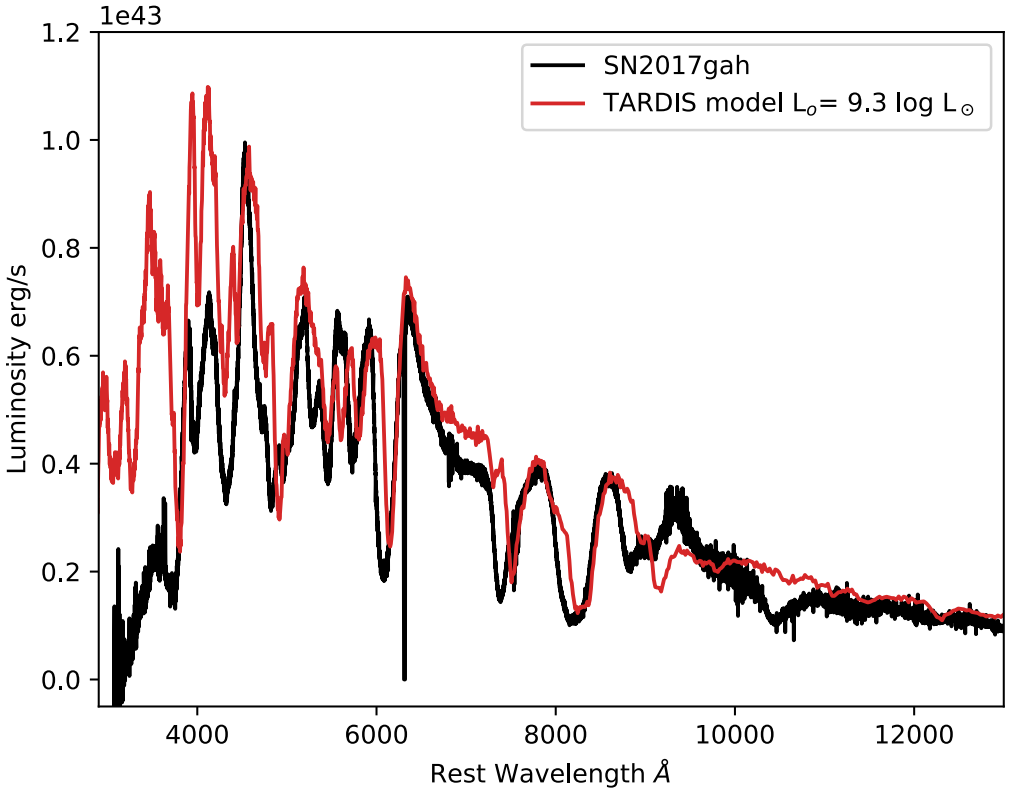

Figure 21: Full Spectrum of SN 2017gah (black) compared to TARDIS model (red) made with abundance profile in Table 2, t_{exp} = 20 days, subluminous density profile in Figure 7 (2005bl-like) and L_o=9.3 log $L_\odot$

6.2.2 Results of Helium Fits with TARDIS

A number of different helium shell models were tested on both of these SNe, ranging from very thin to very thick shells (with the outer 5-14 shells in the TARDIS models consisting almost entirely of helium, corresponding to velocity ranges of 18086 – 27014 km s^{-1} to 11346 – 27014 km s^{-1}) to cover the entire range of thicknesses in other proposed helium shell detonations (see Chapter 4.3). The helium shell was added to the base models described in the previous chapter by changing the number of shells in the TARDIS model from Table 2 which contained helium, starting from highest velocity shell (i.e. the outermost part of the ejecta) and moving inwards towards the photosphere (i.e. to lower velocities) as more shells were added. The number of shells containing helium and the corresponding post-burning mass and velocity range of the helium shell is shown in Table 4. The initial helium abundances were based on the abundances used in the outer shell of the models in Heringer et al. 2017 to produce carbon features and were modified to test which produced the best fits to the observed features.

Within each of the models shown in Table 4, the initial helium shell mass was also increased and decreased by various percentages ($\pm 10\%, \pm 20\%, \pm 40\%, \pm 50\%, \pm 80\%, \pm 85\%, \pm 90\%, \pm 95\%, +100\%$ & $+200\%$) as explained in Chapter 4.3. This is again due to the fact that the exact thickness and composition of the shell is not well known.

No. of shells containing He	Post-Burning He Mass $M_\odot$	Inner Velocity of Shell (km s^{-1})
5	0.0014	18086
6	0.0032	16966
7	0.0068	15976
8	0.0125	15096
9	0.0206	14308
10	0.0319	13598
11	0.0490	12954
12	0.0778	12370
13	0.1181	11836
14	0.1651	11346

Table 4: The number of shells in the TARDIS model which contained helium and the corresponding post-burning helium mass and inner velocity of the helium shell (all shells extend out to 27014 km s^{-1}, hence only the inner velocity is listed). Note the helium masses listed are for the initial abundances used and are increased and decreased from this value as explained in Chapter 4.3.

SN 2017ejb

For SN 2017ejb, the TARDIS models were run using t_{exp} = 20 days and L_o = 9.1 log($L_\odot$). The initial 5 shell model corresponded to a helium shell covering a velocity range of 18086 – 27014 km s^{-1} which left a post-burning helium mass of 0.0014 $M_\odot$. This model and the lower abundance models covering the same velocity range failed to produce a discernible helium feature around $\sim$ 10250 Å. However, the higher abundance models (i.e. models with +40% on the original helium abundance and higher, which corresponds to post-burning masses of 0.0020$M_\odot$ and above) did produce a helium feature in this region as predicted in Boyle et al. 2017, though at too-high velocities ($\sim$ 18250 km s^{-1}) to correspond to the observed feature in the spectrum. The 5 shell models with post-burning helium masses of 0.0014 $M_\odot$ and 0.0020 $M_\odot$ are shown in the top panels of Figure 22.

The 6 shell model (velocity range of 16966 – 27014 km s^{-1}) showed a drastic increase in depth and width of the feature from the 5 shell models. In this case, the initial helium abundance used, which gave a post-burning helium mass of 0.0032 $M_\odot$, produced a discernible helium feature in this region, unlike the 5 shell model. However, this feature is still at too high a velocity (17080 km s^{-1}) to produce the observed feature in the spectrum (13922 km s^{-1}). This model is shown in the top right panel of Figure 22.

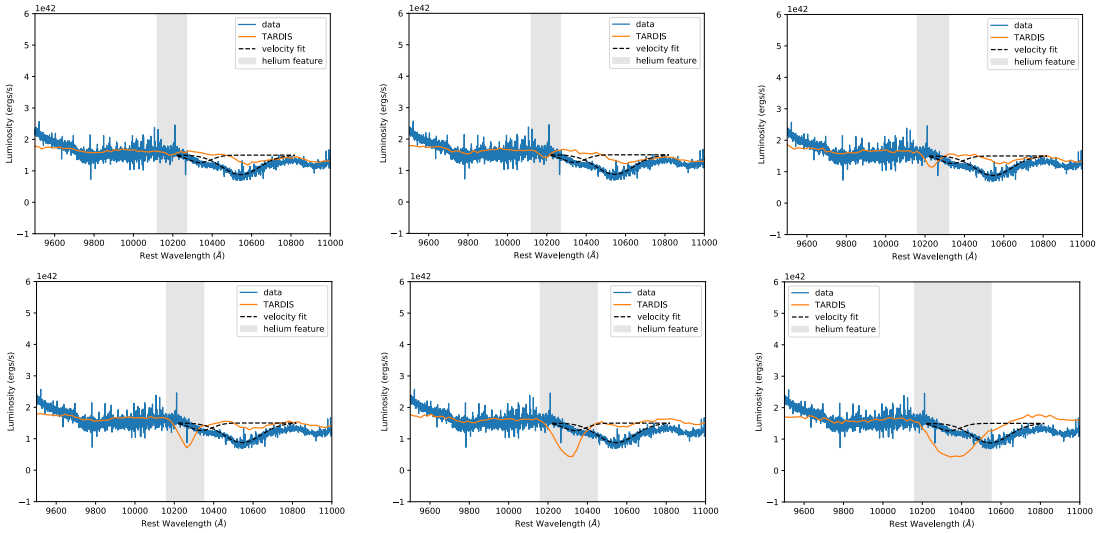

Figure 22: Top Left: The 5 shell model, covering a velocity range of 18086 – 27014 km s^{-1} with a post-burning helium shell mass of 0.0014 $M_{\odot}$ compared to the observed spectrum of SN 2017ejb. Top Middle: The 5 shell model, covering a velocity range of 18086 – 27014 km s^{-1}, with a post-burning helium shell mass of 0.0020 $M_{\odot}$ compared to the observed spectrum of SN 2017ejb. Top Right: The 6 shell model, covering a velocity range of 16966 – 27014 km s^{-1} with a post-burning helium shell mass of 0.0032 $M_{\odot}$ compared to the observed spectrum of SN 2017ejb. Bottom Left: The 7 shell model, covering a velocity range of 15976 – 27014 km s^{-1}, with a post-burning helium shell mass of 0.0068$M_{\odot}$ compared to the observed spectrum of SN 2017ejb. Bottom Middle: The 9 shell model, spanning a velocity range of 14308 – 27014 km s^{-1} with a post-burning helium mass of 0.0206 $M_{\odot}$, compared to the observed spectrum of SN 2017ejb. Bottom Right: The 14 shell model, spanning a velocity range of 11346 – 27014 km s^{-1} with a post-burning helium mass of 0.1651 $M_{\odot}$, compared to the observed spectrum of SN 2017ejb. In all panels, the blue lines are the observed spectrum, the thin, solid, orange line is the TARDIS model of the helium shell, the two dashed, black lines are the Gaussian velocity fits to the feature from Chapter 6.1.2 and the grey shaded regions mark where the helium features appear in the TARDIS models.

Once the feature appears in the TARDIS model, increasing the range of velocities covered by the helium shell continues to deepen the feature, drastically between the 6 and 7 shell (velocity range of 15976 – 27014 km s^{-1}) models and then only fractionally between the 7 to 9 shell models (velocity range of 14308–27014 km s^{-1}), suggesting that the depth of the feature is becoming saturated. The 7 shell model with a post-burning helium mass of 0.0068$M_{\odot}$ is shown in the bottom left panel of Figure 22.

The feature continues to widen as expected as the mass of the helium shell grows and the helium covers more of the velocity shells in the TARDIS model but for all of these models, the feature in the TARDIS spectrum is still at too high a velocity to match the observed feature. The 9 shell model with a post-burning helium mass of 0.0206$M_{\odot}$ is shown in the middle panel of the bottom row in Figure 22 as an example. The 9 shell

model is also the first model where the feature produced by helium in the TARDIS model begins to overlap with the feature in the observed spectrum.

As the helium is added over a wider velocity range, the fit of the TARDIS model to the spectrum improves and then begins to deteriorate again as more and more helium is added. Increasing the number of shells which contain helium to 10 and 11 shells (13598 – 27014 km s^{-1} and 12955 – 27014 km s^{-1} for the 10 & 11 shell models respectively) improves the fit but increasing the helium shell beyond 11 shells to models which extend over wider velocity ranges only serves to worsen the fit. An example of the fits for higher mass models (14 shells, covering a velocity range of 11346–27014 km s^{-1}) can be found in Figure 22.

The best fit model was chosen by taking residuals between the TARDIS models and the spectrum across the possible helium feature and using the average of these residuals in conjunction with the maximum and minimum residuals to determine the best fit to the spectrum. Using this method, it was found that the best fit model for SN 2017ejb is the 10 shell model, covering a velocity range of 13598 – 27014 km s^{-1} and with a post-burning helium shell mass of 0.0064 $M_\odot$ (i.e. -80% the original abundance). This model is shown in Figure 23.

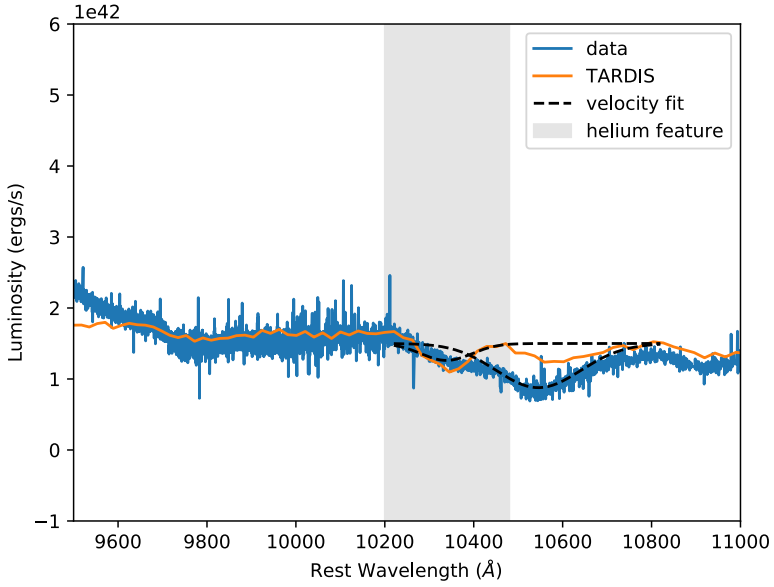

Figure 23: The best fit helium model (10 shells, covering a velocity range of 13598 – 27014 km s^{-1} with a post-burning helium shell mass of 0.0064 $M_\odot$) for SN 2017ejb. The blue line is the observed spectrum, the thin, solid, orange line is the TARDIS model of the helium shell, the two dashed, black lines are the Gaussian velocity fits to the feature from Chapter 6.1.2 and the grey shaded region marks where the helium feature appears in the TARDIS model.

This corresponds to a helium velocity of 13735 km s^{-1}, which is in good agreement with the initial velocity estimation of 13922 km s^{-1}, although is much lower than the values found in Boyle et al. 2017 of $16000 - 19000$ km s^{-1}.

The difference between the two sets of models is most likely due to the density profiles which were used in this investigation. Boyle et al. 2017 used density profiles based on work of Fink et al. 2010 and Kromer et al. 2010 for their 'high-mass' model and Sim et al. 2010 for their subluminous, 'low-mass' model, whereas the density profile used in this investigation was based off the profile used to fit the subluminous SN 2005bl in Heringer et al. 2017. As previously mentioned, this investigation found that for SN 2017ejb and SN 2017gah, using density profiles similar to the commonly used $\omega 7$ for fitting 'normal' luminosity events meant that the spectra were being fit with the incorrect ionisation state of certain elements (e.g. Si III instead of Si II). The higher temperatures that using steeper density profiles caused also prevented some elements from producing features e.g. oxygen. Using a shallower density profile, such as the one used in this investigation, allowed these weaker elements to produce features in the model spectra which better matched those of the measured spectra for these two SNe. This in turn may have allowed for the helium features to form more easily in the model spectra in this thesis compared to those in Boyle et al. 2017 or affected the positions at which the helium feature could be produced in the spectrum, leading to the discrepancy between the recovered velocities between the two investigations. Further work would need to be carried out into using different density profiles to model these and other objects to determine the full effects of using different profiles, particularly on the NIR region around $\sim$ 10250 Å, and to determine which is the most accurate method for these transitional objects.

Whilst the left side of the feature in the best fit model is in good agreement with the spectral data, it can be seen in Figure 23 that the right hand side of the feature is less well fit. One suggestion for this discrepancy between the TARDIS models and the spectrum is the magnesium abundance used in the base model. While there was enough magnesium to produce some of the features in the full spectrum (see Figure 20), it can also be seen in this figure that the magnesium features in the model spectrum do not fully match the depth of the same features in the data (e.g. the Mg II feature around 9200 Å) and have even created extra features in the model which do not appear in the spectrum. While small discrepancies such as these are normally acceptable when trying to find a model that fits the spectrum as a whole, it is possible that in this

scenario, the poorer magnesium fits are causing issues in the NIR region.

As can be seen in Figures 22 and 23, in all models, there is a discernible feature to the right of the TARDIS models ($\sim 10500 - 10700$Å) which is caused by magnesium. This feature agrees relatively well to the width of the right side of the spectral feature, however, it is not deep enough to fully match the feature in the spectrum of SN 2017ejb. Moreover, as the mass of the helium shell increases, for example between the 5 shell models in the top panels of Figure 22 with post-burning helium shell masses of ≤ 0.0020 $M_{\odot}$ and the 7 shell model in the bottom right panel with a post-burning helium shell mass of 0.0068 $M_{\odot}$, the magnesium feature decreases in strength. This suggests that perhaps the magnesium is being affected by the growing helium feature next to it. If the magnesium abundances were altered in the base model, perhaps this would remedy the discrepancies between the model and the full spectrum and provide an even better overall fit to the spectral data. Further investigation would need to be carried out, adding more magnesium to the base models to clarify this matter fully.

The 2μm line did not help to further clarify the possibility of any helium features in the spectrum. The spectrum is noisy in this region and, as mentioned in Chapter 2.2, Molecfit did less well on removing tellurics in the NIR. Even when the data was smoothed to overcome this problem, there appears to be no feature around this region in the observed spectrum or in the TARDIS spectrum. This is in line with what was found in Boyle et al. 2017. As this is a 'subluminous' event, it may be prudent to assume that the expected results from this model would match the 'low-mass' models of Boyle et al. 2017 and that a weak feature would be expected to show in this region. However, the post-burning mass of the helium shell from the 'low-mass' models was much higher than the best fit model found here for SN 2017ejb; 0.077 $M_{\odot}$ compared to only 0.0064 $M_{\odot}$. Even the 'high-mass' models had more helium post-burning than that found here (0.030 $M_{\odot}$) and these models are thought to produce a 2μm feature which would be too weak to detect. This means that there is no feature expected to appear in this region for SN 2017ejb either, even if the SN was caused by a helium shell detonation, and so the 2μm cannot be used to corroborate the existence of helium for this event. This is shown in Figure 24.

An interesting observation from the outcomes of these models is that it is not solely the mass of the helium shell which is important but where it is distributed throughout the model. The initial 7 shell model covering a velocity range of $15976 - 27014$ km s^{-1} produced a post-burning helium shell mass of $0.0068 M_{\odot}$ whilst the 10 shell best fit

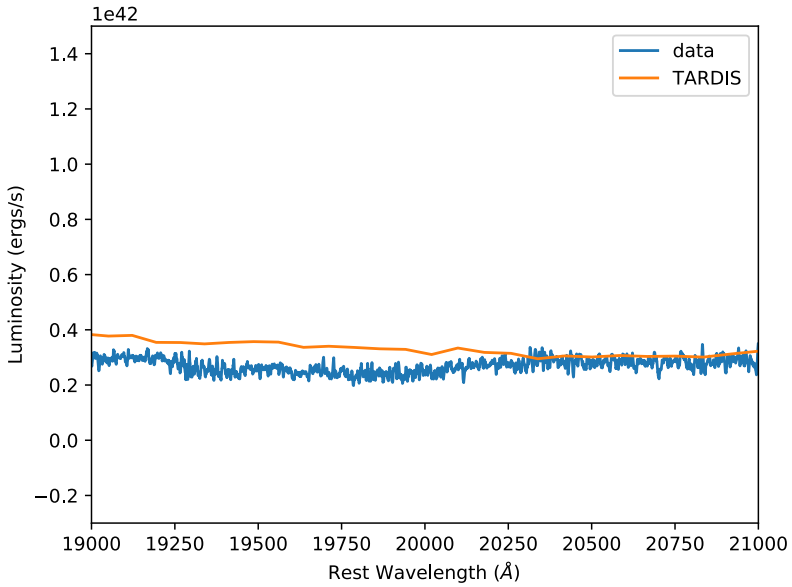

Figure 24: The spectrum of SN 2017ejb around the 2μm region (blue) where another possible helium feature may appear. The TARDIS spectral model shown in the thin, orange line is the best fit model shown in Figure 23.

model with -80% the original helium abundance produced a post-burning helium shell mass of 0.0064$M_\odot$, very similar to the 7 shell model. However, it can be seen from model spectra for both of these objects (bottom right panel of Figure 22 and Figure 23 respectively) that these two produce very different quality of fits to the data. This in itself illustrates that the position of the helium shell within the model is as important as the amount of helium used and this should be taken into careful consideration when modelling these types of objects.

SN 2017gah

The same process of fitting the possible helium feature was carried out for SN 2017gah. For SN 2017gah, the TARDIS models were run using t_{exp} = 20 days and L_o = 9.3 log($L_\odot$). Unlike with SN 2017ejb, the 5 shell model (velocity range of 18086 – 27014 km s^{-1}) produced no discernible helium feature anywhere in the NIR region in the TARDIS spectrum in any model except for the highest abundance model (+200%, post-burning helium shell mass of 0.0043 $M_\odot$). The 6 shell models (velocity range of 16966 – 27014 km s^{-1}) with post-burning helium masses of $\geq$ 0.0039 $M_\odot$ (i.e. +20% the original abundance or higher) were the first to produce a small helium feature, likely due to the higher temperatures caused by the higher luminosity used in these models. The feature around $\sim$ 10250 Å widens and deepens drastically in the 7 shell model for

SN 2017gah (velocity range of 15976 – 27014 km s^{-1}) and this time, the depth becomes saturated in the 8 shell model (velocity range of 15096 – 27014 km s^{-1}). The 6 and 7 shell models are shown in Figure 25.

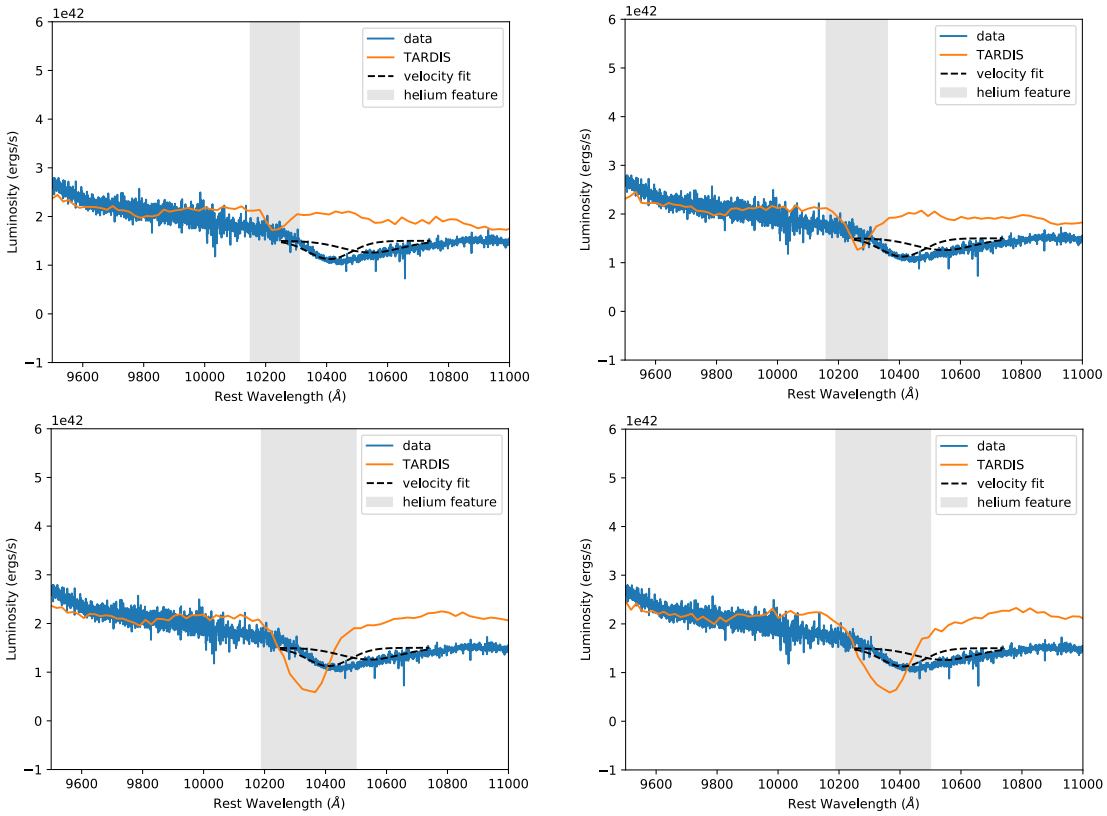

Figure 25: Top Left: The 6 shell model, covering a velocity range of 16966 – 27014 km s^{-1} with a post-burning helium shell mass of 0.0039 $M_\odot$ compared to the observed spectrum of SN 2017gah. Top Right: The 7 shell model, covering a velocity range of 15976 – 27014 km s^{-1} with a post-burning helium shell mass of 0.0068 $M_\odot$ compared to the observed spectrum of SN 2017gah. Bottom Left: The 11 shell model, spanning a velocity range of 12955 – 27014 km s^{-1} with a post-burning helium mass of 0.0490 $M_\odot$, compared to the observed spectrum of SN 2017gah. Bottom Right: The 12 shell model, spanning a velocity range of 12370 – 27014 km s^{-1} with a post-burning helium mass of 0.0778 $M_\odot$, compared to the observed spectrum of SN 2017gah. In all panels, the blue lines are the observed spectrum, the thin, solid, orange line is the TARDIS model of the helium shell, the two dashed, black lines are the Gaussian velocity fits to the feature from Chapter 6.1.1 and the grey shaded regions mark where the helium features appear in the TARDIS models.

Unlike with SN 2017ejb, there is no magnesium feature appearing to the right of the TARDIS models to match that side of the feature in the spectral data, even in the lowest mass helium shells. This is to be expected - the TARDIS models used for SN 2017gah are at a higher luminosity and temperature than those used to model SN 2017ejb. Increasing the temperature in these models can prevent weaker elements from producing features and it can be seen that the magnesium feature around 9200 Å is fit

even less well for SN 2017gah (see Figure 21) than it was for SN 2017ejb, meaning that the weak magnesium feature that was showing in the models of SN 2017ejb has most likely been lost due to the increased temperature. As before, increasing the abundance of magnesium within the base models should help to resolve this issue.

For SN 2017gah, the helium feature in the TARDIS models only begin to start overlapping with the feature in the spectrum at 11 shells, or when the helium shell is covering a velocity range of 12955 – 27014 km s^{-1}, however, even this model does not provide a good fit to the spectrum. It takes increasing the number of shells containing helium to at least 12 before the models and the spectrum start to come into agreement, unlike the case of SN 2017ejb, which worsened after 11 shells. The 11 and 12 shell models for SN 2017gah are shown in Figure 25.

As before, the residuals between the TARDIS models and the observed spectrum were used to determine the best fitting model, which for SN 2017gah was the 13 shell model (velocity range of 11836 – 27014 km s^{-1}) with a post-burning helium mass of 0.0591 $M_\odot$ (-50% abundance). This model is shown in the left panel of Figure 26.

As can be seen in this figure, the helium feature is slightly too strong to match the spectrum. The next helium shell mass that was tested of 0.0236 $M_\odot$ (-80% abundance), shown in the right panel of the same figure, produces a helium feature that is of the right strength but is too narrow to fit the feature. It is likely that the true best fit model for SN 2017gah is a 13 shell model with a helium abundance that lies somewhere between these two helium shell masses and so in this case, it is assumed that the post-burning helium mass of 0.0591 $M_\odot$ is an upper limit on the amount of helium left in SN 2017gah, rather than an accurate measure of the value.

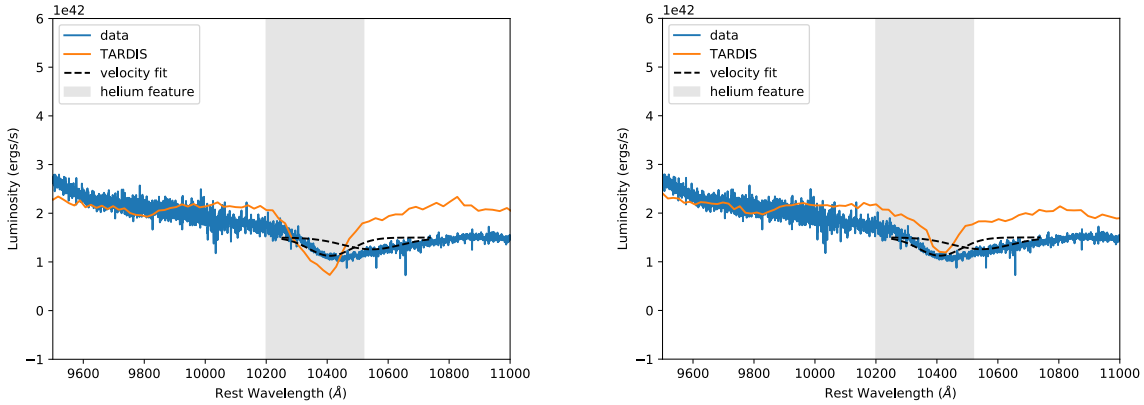

Figure 26: Left: The 13 shell model, covering a velocity range of 11836 – 27014 km s^{-1} with a post-burning helium shell mass of 0.0591 M$_\odot$ compared to the observed spectrum of SN 2017gah. Right: The 13 shell model, covering a velocity range of 11836 – 27014 km s^{-1} with a post-burning helium shell mass of 0.0236 M$_\odot$ compared to the observed spectrum of SN 2017gah. In both panels, the blue lines are the observed spectrum, the thin, solid, orange line is the TARDIS model of the helium shell, the two dashed, black lines are the Gaussian velocity fits to the feature from Chapter 6.1.1 and the grey shaded regions mark where the helium features appear in the TARDIS models.

The two different models shown in Figure 26 give slightly different velocities for the helium feature due to the shape of the features produced. The 0.0591 M$_\odot$ model gives a velocity of 11860 km s^{-1} while the 0.0236 M$_\odot$ gives a velocity of 11572 km s^{-1}. This again means that the velocity of the true best fit model most likely lies between these two values. Both values, however, are in good agreement with the initial velocity fit which predicted a velocity of $\sim$ 11870 km s^{-1}. Again, this is much lower than the velocities predicted in Boyle et al. 2017 but is likely due to the different density profiles used in this thesis. As with the best fit model of SN 2017ejb, it is suggested that the fit to the right hand side of the feature could be improved by adding more magnesium into the base models.

As before with SN 2017ejb, it is interesting to note that the position of the helium within the model is an important factor in the quality of the fit. For the 11 shell model shown in Figure 25, the post-burning helium mass was 0.0490 M$_\odot$. In this model, the helium was spread over a velocity range of 12955 – 27014 km s^{-1}. The 13 shell model at -50% abundance had a similar post-burning helium shell mass of 0.0591 M$_\odot$ spread over a velocity range of 121836 – 27014 km s^{-1} and yet produces a better fit to the spectrum in both terms of width and depth of the helium feature, despite having more helium left in the model. This again illustrates the importance of the positioning of the shell as well as the amount of mass within it in reproducing possible helium features.

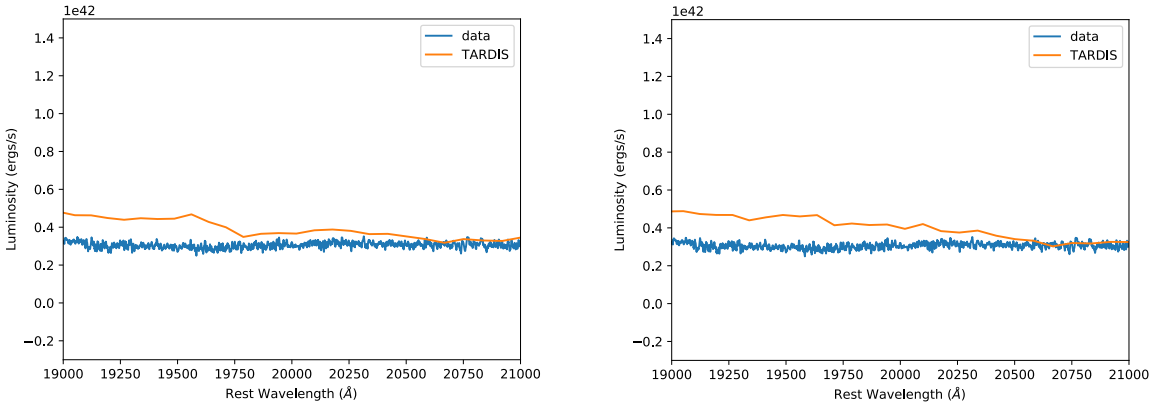

Figure 27: Left: The 13 shell model, covering a velocity range of 11836 – 27014 km s^{-1} with a post-burning helium shell mass of 0.0591 $M_{\odot}$ compared to the observed spectrum of SN 2017gah around the 2μm region where another possible helium feature may appear. Right: The 13 shell model, covering a velocity range of 11836 – 27014 km s^{-1} with a post-burning helium shell mass of 0.0236 $M_{\odot}$ compared to the observed spectrum of SN 2017gah around the 2μm region where another possible helium feature may appear. In both panels, the blue lines are the observed spectrum and the thin, solid, orange line is the TARDIS model of the helium shell.

Again, as with SN 2017ejb, a search of the 2μm region reveals no other possible helium feature detection in either model. This too is in line with Boyle et al. 2017 as the shell mass remaining in these models (post-burning helium shell mass of 0.0236-0.0591 $M_{\odot}$) is similar to the helium shell left in the 'high-mass' models of this paper (with post-burning helium masses of 0.030$M_{\odot}$), and hence, it is expected that no helium feature should appear as in Boyle et al. 2017. This is shown in Figure 27.

Chapter 7: Conclusion And Future Work

The aim of this work was to try and find previously undetected helium shell detonations of Type Ia SNe in a large sample of objects and to model the spectra of these objects with the radiative transfer code, TARDIS. 33 Ia spectra of different sub-types ('normal', '91bg-like' and '91T-like') were investigated for signatures of a helium shell detonation, namely a feature appearing in the NIR around $\sim$ 10250 Å. According to Boyle et al. 2017, this is the region where helium features caused by the He I 10830 Å line would show in the spectra of 'normal' and 'subluminous' SNe Ia at velocities of $\sim 16,000 - 19,000$ km s^{-1} if they had been caused by a helium shell detonation. However, this region can be contaminated by two other features; C I 10693 Å and Mg II 10927 Å.

To be able to distinguish any possible helium features in this region from any Mg II or C I features, velocity fits were carried out to other well-known features that appear in Ia spectra to determine the most likely constituents and their velocities. These were performed for the Si II 6355 Å, Ca II NIR triplet and O I 7773 Å features to build up an idea of the ejecta structure within the sample.

Visually, there were 9 objects which were determined to have features appearing in the NIR around 10250 Å. Of these 9, the initial velocity fits suggested that 7 were comprised of Mg II. The other two; SN 2017gah and SN 2017ejb, were suggested to be comprised of a mix of Mg II and He I.

These two objects were then modelled with TARDIS, using a custom abundance and density profile based on those used to model SN 2005bl in Heringer et al. 2017. SN 2005bl and SN 2017ejb have both been identified as '91bg-like' SNe and whilst SN 2017gah has been identified as a 'normal' event, closer inspection of its spectral features suggests that it is a transitional event, falling somewhere between the two groups, meaning that using a subluminous density and abundance profile was valid for both of the events.

Helium shells covering velocity ranges of 18086 – 27014 km s^{-1} to 11346 – 27014 km s^{-1} were added into the TARDIS models to see if these reproduced the features in the observed spectra. The best fit helium shell model for SN 2017ejb was found to be a helium shell over the velocity range of 13598 – 27014 km s^{-1} which left a post-burning helium shell mass of 0.0064 M$_\odot$. This would correspond to a helium velocity of $\sim$ 13735 km s^{-1}, which is close to that predicted by the initial velocity fit ($\sim$

13922 km s^{-1}).

The best fit model for SN 2017gah was found to be a helium shell covering a velocity range of 11836 – 27014 km s^{-1} which left a post-burning helium shell mass of 0.0236-0.0591 $M_{\odot}$. In this case, the true best fit model most likely lies between two of the models tested, hence the range of final helium shell masses. This corresponds to a helium velocity of 11572 – 11870 km s^{-1}, which is also in good agreement with the initial velocity fit of the feature (11860 km s^{-1}).

Whilst both of these 'best fit' models produce reasonable matches to the observed features in the spectrum, it is suggested that both could be further improved by altering the magnesium abundances of the base models the helium shells were added to. The base models do not have the correct magnesium abundance to reproduce all of the magnesium features in the entire spectra, which lessens the quality of the fit to the overall spectral feature. Indeed, it can be seen in Figure 22 that a weak magnesium feature does appear in the right hand side of the model spectra for SN 2017ejb which is of a similar shape to the feature in the spectrum, although it is not strong enough to fully match the spectrum. As SN 2017gah was modelled as a higher temperature event, the weak magnesium feature present in the model of SN 2017ejb is lost in this case. Future work would include running these helium shell models again but with altered magnesium abundances to try and further improve the quality of the model fit to the data and strengthen the robustness of the possible helium detections in these two objects.

Out of a total of 33 SNe Ia, there are 1-2 events with possible helium features in their spectra. This corresponds to a minimum of $\sim 3–6\%$ of the sample being candidates for helium shell detonations. This number could, however, be higher as the non-detection of helium does not preclude the possibility of a helium shell detonation, as found in this thesis. In both cases, the events were low luminosity, with SN 2017ejb being a '91bg-like' event and SN 2017gah being a probable transitional event, lying somewhere between the '91bg-like' and 'normal' luminosity classes.

It has been noted in several studies that the early light curves of SNe which were caused by a helium shell detonation are thought to have peculiar 'bumps' and blue colours due to early flux excess (Noebauer et al. 2017, Polin et al. 2019). One of the most studied objects with an early light curve bump, SN 2017cbv (Hosseinzadeh et al. 2017), is present in this sample. This was one of the nine SNe which showed a feature in the NIR region where the He I 10830 Å may appear, but the preliminary line velocity

investigation ruled out the possibility of this being He I, attributing the feature entirely to Mg II 10927 Å. None of the light curves for the plausible helium shell objects in this investigation were at early enough epochs to explore the possibility of connecting helium features with light curve bumps. Other future work would include gathering a sample of these objects with early time light curves 'bumps' to compare to those of this sample, particularly to SN 2017ejb and SN 2017gah to see if any relationship can be found between these objects with early light curve bumps and SNe which show a plausible He I feature. Another possibility would also be to use the best fit helium shell models for both SN 2017gah and SN 2017ejb to create model light curves to see how these would compare to the measured light curves' colour, shape and decline rate. This could lend further robustness to the possible helium shell detections if the models could produce similarly shaped light curves.

Finally, the density profiles used in this thesis were shallower than those used in Boyle et al. 2017 and the combination of these and the custom abundance profile produced helium features at lower velocities than predicted in this paper. It is suggested that more work needs to be carried out into the effects of different density profiles on these models to provide insight into the correct profiles which should be used to accurately reproduce these events. The same is suggested for the abundance profiles as the abundance profile for a 'normal' luminosity events produced features in the wrong ionisation in these models (i.e. Si III instead of Si II) and overall produced worse fits to the spectral data than the subluminous profiles.

References

Amanullah, R. et al. (2015). "Diversity in extinction laws of Type Ia supernovae measured between 0.2 and 2μm". In: *Monthly Notices of the Royal Astronomical Society* 453.3, pp. 3300–3328. ISSN: 13652966. DOI: 10.1093/mnras/stv1505.

Anand, S. P. S. (1965). "On Chandrasekhar's Limiting Mass for Rotating White Dwarf Stars*". In: *Proceedings of the National Academy of Sciences of the United States of America* 54. URL: https://www.pnas.org/content/pnas/54/1/23.full.pdf.

Baade, W. and F. Zwicky (1934). "On Super-Novae". In: *Proceedings of the National Academy of Sciences* 20.5, pp. 254–259. ISSN: 0027-8424. DOI: 10.1073/pnas.20.5.254.

Barbary, K. (2016). *extinction documents*. URL: https://extinction.readthedocs.io/en/latest/.

Barna, B. et al. (2016). "Possible detection of singly ionized oxygen in the Type Ia SN 2010kg". In: *Monthly Notices of the Royal Astronomical Society* 457.3, pp. 3225–3240. ISSN: 13652966. DOI: 10.1093/mnras/stw207.

Betoule, M. et al. (2014). "Improved cosmological constraints from a joint analysis of the SDSS-II and SNLS supernova samples". In: *Astronomy and Astrophysics* 568. ISSN: 14320746. DOI: 10.1051/0004-6361/201423413.

Blondin, S. et al. (2012). "The spectroscopic diversity of Type Ia supernovae". In: *The Astronomical Journal* 143.5. ISSN: 00046256. DOI: 10.1088/0004-6256/143/5/126.

Blondin, Stéphane and John L. Tonry (2007). "Determining the Type, Redshift, and Age of a Supernova Spectrum". In: *The Astrophysical Journal* 666.2, pp. 1024–1047. ISSN: 0004-637X. DOI: 10.1086/520494.

Blondin, Stéphane et al. (2017). "Evidence for sub-Chandrasekhar-mass progenitors of Type Ia supernovae at the faint end of the width-luminosity relation". In: *Monthly Notices of the Royal Astronomical Society* 470.1, pp. 157–165. ISSN: 13652966. DOI: 10.1093/mnras/stw2492.

Blondin, Stéphane et al. (2013). "One-dimensional delayed-detonation models of type ia supernovae: Confrontation to observations at bolometric maximum". In: *Monthly Notices of the Royal Astronomical Society* 429.3, pp. 2127–2142. ISSN: 00358711. DOI: 10.1093/mnras/sts484.

Boyle, Aoife et al. (2017). "Helium in double-detonation models of type Ia supernovae". In: *A&A* 599. DOI: 10.1051/0004-6361/201629712. URL: https://www.aanda.org/articles/aa/pdf/2017/03/aa29712-16.pdf.

Brown, Peter J. et al. (2018). "Red and Reddened: Ultraviolet through Near-Infrared Observations of Type Ia Supernova 2017erp". In: URL: http://arxiv.org/abs/1808.04729.

Bulla, M., S. A. Sim, and M. Kromer (2015). "Polarization spectral synthesis for Type Ia supernova explosion models". In: *Monthly Notices of the Royal Astronomical Society* 450.1, pp. 967–981. ISSN: 13652966. DOI: 10.1093/mnras/stv657.

Burnham, K. P. and D. R. Anderson (2002). *Model Selection And Multimodel Inference: A Practical Information-Theoretic Approach (Second Edition)*. Springer, p. 488. ISBN: 0387953647.

Burnham, K. P. and D. R. Anderson (2004). "Multimodel inference: Understanding AIC and BIC in model selection". In: *Sociological Methods and Research* 33.2, pp. 261–304. ISSN: 00491241. DOI: 10.1177/0049124104268644.

Butkevich, A. G., A. V. Berdyugin, and P. Teerikorpi (2005). "Statistical biases in stellar astronomy: The Malmquist bias revisited". In: *Monthly Notices of the Royal Astronomical Society* 362.1, pp. 321–330. ISSN: 00358711. DOI: 10.1111/j.1365-2966.2005.09306.x.

Cardelli, Jason A, Geoffrey C Clayton, and John S Mathis (1989). "The Relationship Between Infrared, Optical, and Ultraviolet Extinction". In: *The Astrophysical Journal* 345, pp. 245–256. DOI: 10.1086/167900.

Chambers, K. C. et al. (2016). "The Pan-STARRS1 Surveys". In: URL: http://arxiv.org/abs/1612.05560.

Chandrasekhar, S. (1931). "The Maximum Mass of Ideal White Dwarfs". In: *The Astrophysical Journal* 74. URL: http://articles.adsabs.harvard.edu/pdf/1931ApJ...74...81C.

Chandrasekhar, S. (1935). "The Maximum Mass of Ideal White Dwarfs". In: *Monthly Notices of the Royal Astronomical Society*. URL: https://ui.adsabs.harvard.edu/abs/1935MNRAS..95..207C.

Chevalier, R. A. and P. C. Plait (1988). "The Nature of S Andromedae (SN 1885A)". In: *American Astronomical Society* 331, pp. 109–112. ISSN: 1098-6596. DOI: 10.1017/CBO9781107415324.004.

Childress, M. J. et al. (2014). "High-velocity features in Type Ia supernova spectra". In: *Monthly Notices of the Royal Astronomical Society* 437.1, pp. 338–350. ISSN: 00358711. DOI: 10.1093/mnras/stt1892.

Childress, M. J. et al. (2013a). "Spectroscopic observations of sn 2012fr: A luminous, normal type ia supernova with early high-velocity features and a late velocity plateau". In: *The Astrophysical Journal* 770.1. ISSN: 15384357. DOI: 10.1088/0004-637X/770/1/29.

Childress, M. et al. (2013b). "Host galaxy properties and hubble residuals of type Ia supernovae from the Nearby Supernova Factory". In: *The Astrophysical Journal* 770.2. ISSN: 15384357. DOI: 10.1088/0004-637X/770/2/108. arXiv: 1304.4720.

Conley, A. et al. (2008). "SiFTO: An Empirical Method for Fitting SN Ia Light Curves". In: *The Astrophysical Journal* 681.1, pp. 482–498. ISSN: 0004-637X. DOI: 10.1086/588518.

Conley, A. et al. (2011). "Supernova constraints and systematic uncertainties from the first three years of the Supernova Legacy Survey". In: *The Astrophysical Journal, Supplement Series* 192.1. ISSN: 00670049. DOI: 10.1088/0067-0049/192/1/1. arXiv: 1104.1443.

curve_fit (2018). URL: https://docs.scipy.org/doc/scipy/reference/generated/scipy.optimize.curve_fit.html.

De, Kishalay et al. (2019). "ZTF 18aaqeasu (SN2018byg): A Massive Helium-shell Double Detonation on a Sub-Chandrasekhar-mass White Dwarf". In: *The Astrophysical Journal* 873.2, p. L18. ISSN: 2041-8213. DOI: 10.3847/2041-8213/ab0aec. URL: http://dx.doi.org/10.3847/2041-8213/ab0aec.

Dessart, Luc and D. John Hillier (2015). "One-dimensional non-LTE time-dependent radiative transfer of an He-detonation model and the connection to faint and fast-decaying supernovae". In: *Monthly Notices of the Royal Astronomical Society* 447.2, pp. 1370–1382. ISSN: 13652966. DOI: 10.1093/mnras/stu2520.

Dimitriadis, G. et al. (2018). "K2 Observations of SN 2018oh Reveal a Two-component Rising Light Curve for a Type Ia Supernova". In: *The Astrophysical Journal* 870.1, p. L1. ISSN: 2041-8213. DOI: 10.3847/2041-8213/aaedb0.

Ergon, M. et al. (2018). "Monte-Carlo methods for NLTE spectral synthesis of supernovae". In: *Astronomy and Astrophysics* 620, pp. 1–22. ISSN: 14320746. DOI: 10.1051/0004-6361/201833043.

Filippenko, A. V. et al. (1992a). "THE SUBLUMINOUS, SPECTROSCOPICALLY PECULIAR TYPE la SUPERNOVA 1991bg IN THE ELLIPTICAL GALAXY NGC 4374". In: *The Astronomical Journal* 104.4. ISSN: 1098-6596. DOI: 10.1017/CBO9781107415324.004.

Filippenko, Alexei V et al. (1992b). "The Peculiar Type Ia SN 1991T: Detonation of a white Dwarf?" In: *ApJ* 384, pp. 15–18.

Fink, M. et al. (2010). "Double-detonation sub-Chandrasekhar supernovae: Can minimum helium shell masses detonate the core?" In: *Astronomy and Astrophysics* 514.8, pp. 1–10. ISSN: 14320746. DOI: 10.1051/0004-6361/200913892.

Fink, M. et al. (2018). "Thermonuclear explosions of rapidly differentially rotating white dwarfs: Candidates for superluminous Type Ia supernovae?" In: *Astronomy and Astrophysics* 618.2012, pp. 1–12. ISSN: 14320746. DOI: 10.1051/0004-6361/201833475.

Fink, M. et al. (2014). "Three-dimensional pure deflagration models with nucleosynthesis and synthetic observables for type ia supernovae". In: *Monthly Notices of the Royal Astronomical Society* 438.2, pp. 1762–1783. ISSN: 00358711. DOI: 10.1093/mnras/stt2315.

Fitzpatrick, Edward L. (1999). "Correcting for the Effects of Interstellar Extinction". In: *Publications of the Astronomical Society of the Pacific* 111.755, pp. 63–75. ISSN: 0004-6280. DOI: 10.1086/316293.

Folatelli, Gastón et al. (2012). "Unburned material in the ejecta of type Ia supernovae". In: *The Astrophysical Journal* 745.1. ISSN: 15384357. DOI: 10.1088/0004-637X/745/1/74.

Foley, Ryan J. et al. (2013). "Type Iax Supernovae: A new class of stellar explosion". In: *The Astrophysical Journal* 767.1. ISSN: 15384357. DOI: 10.1088/0004-637X/767/1/57.

Fontaine, G., P. Brassard, and P. Bergeron (2001). "The Potential of White Dwarf Cosmochronology". In: *Publications of the Astronomical Society of the Pacific* 113.782. URL: https://iopscience.iop.org/article/10.1086/319535/pdf.

Fouesneau, Morgan and Timothy Morton (2018). *pyphot*. URL: https://github.com/mfouesneau/pyphot%20http://mfouesneau.github.io/docs/pyphot/pyphot.html#.

Freudling, W et al. (2013). "The ESO Reflex environment". In: *A&A* 559, A96.

Graham, Matthew J. et al. (2019). "The Zwicky Transient Facility: Science objectives". In: *Publications of the Astronomical Society of the Pacific* 131.1001. ISSN: 00046280. DOI: 10.1088/1538-3873/ab006c.

Guy, J. et al. (2007). "SALT2: Using distant supernovae to improve the use of type la supernovae as distance indicators". In: *A&A* 466.1, pp. 11–21. ISSN: 00046361. DOI: 10.1051/0004-6361:20066930.

Hachinger, S. et al. (2012). "How much H and He is 'hidden' in SNe Ib/c? - I. Low-mass objects". In: *Monthly Notices of the Royal Astronomical Society* 422.1, pp. 70–88. ISSN: 00358711. DOI: 10.1111/j.1365-2966.2012.20464.x.

Hachinger, S. et al. (2009). "Spectral analysis of the 91bg-like Type Ia SN 2005bl: Low luminosity, low velocities, incomplete burning". In: *Monthly Notices of the Royal Astronomical Society* 399.3, pp. 1238–1254. ISSN: 00358711. DOI: 10.1111/j.1365-2966.2009.15403.x.

Hamuy, Mario et al. (2003). "An asymptotic-giant-branch star in the progenitor system of a type la supernova". In: *Nature* 424.6949, pp. 651–654. ISSN: 00280836. DOI: 10.1038/nature01854.

Heringer, E. et al. (2017). "Spectral Sequences of Type Ia Supernovae. I. Connecting Normal and Subluminous SNe Ia and the Presence of Unburned Carbon". In: *The Astrophysical Journal* 846.1, p. 15. DOI: 10.3847/1538-4357/aa8309.

Hosseinzadeh, Griffin et al. (2017). "Early Blue Excess from the Type Ia Supernova 2017cbv and Implications for Its Progenitor". In: *The Astrophysical Journal* 845.2, p. L11. ISSN: 2041-8213. DOI: 10.3847/2041-8213/aa8402.

Hoyle, F. and W. A. Fowler (1960). "Nucleosynthesis in Supernovae". In: *The Astrophysical Journal* 132. URL: http://articles.adsabs.harvard.edu/pdf/1960ApJ...132..565H.

Hsiao, E. Y. et al. (2015). "Strong near-infrared carbon in the Type Ia supernova iPTF13ebh". In: 9, pp. 1–18. ISSN: 0004-6361. DOI: 10.1051/0004-6361/201425297. URL: http://arxiv.org/abs/1503.02293%0Ahttp://dx.doi.org/10.1051/0004-6361/201425297.

Hurvich, Clifford M. and Chih Ling Tsai (1989). "Regression and time series model selection in small samples". In: *Biometrika* 76.2, pp. 297–307. ISSN: 00063444. DOI: 10.1093/biomet/76.2.297.

Iben, I. and A. V. Tutukov (1984). "Supernova of Type I as End Products of the Evolution of Binaries with Components of Moderate Initial Mass (M ¡9 M0) 1".

In: *The Astrophysical Journal Supplement Series* 54. URL: http://articles.adsabs.harvard.edu/pdf/1984ApJS...54..335I.

Ivezić, Željko et al. (2019). "LSST: From Science Drivers to Reference Design and Anticipated Data Products". In: *The Astrophysical Journal* 873.2, p. 111. ISSN: 1538-4357. DOI: 10.3847/1538-4357/ab042c.

Jha, Saurabh, Adam G. Riess, and Robert P. Kirshner (2007). "Improved Distances to Type Ia Supernovae with Multicolor Light-Curve Shapes: MLCS2k2". In: *The Astrophysical Journal* 659.1, pp. 122–148. ISSN: 0004-637X. DOI: 10.1086/512054.

Jiang, Ji An et al. (2017). "A hybrid type Ia supernova with an early flash triggered by helium-shell detonation". In: *Nature* 550.7674, pp. 80–83. ISSN: 14764687. DOI: 10.1038/nature23908.

Joglekar, Hrishikesh et al. (2006). "Oldest sky-chart with supernova record". In: *Journal of Indian Archaelogical Society* 4325, pp. 1–7. URL: http://www.tifr.res.in/~vahia/oldest-sn.pdf.

Jones, David O., Adam G. Riess, and Daniel M. Scolnic (2015). "Reconsidering the effects of local star formation on type Ia supernova cosmology". In: *The Astrophysical Journal* 812.1, p. 31. ISSN: 15384357. DOI: 10.1088/0004-637X/812/1/31. URL: http://dx.doi.org/10.1088/0004-637X/812/1/31.

Kasen, Daniel, R. C. Thomas, and P. Nugent (2006). "Time-dependent Monte Carlo Radiative Transfer Calculations for Three-dimensional Supernova Spectra, Light Curves, and Polarization". In: *The Astrophysical Journal* 651.1, pp. 366–380. ISSN: 0004-637X. DOI: 10.1086/506190.

Kerzendorf, W. E. and S. A. Sim (2014). "A spectral synthesis code for rapid modelling of supernovae". In: *Monthly Notices of the Royal Astronomical Society* 440.1, pp. 387–404. ISSN: 13652966. DOI: 10.1093/mnras/stu055. URL: k.

Kimeswenger, Stefan et al. (2017). "Molecfit GUI and Tutorial". In: *VLT-MAN-ESO-19550-5928* 1.3.

Kramida, A. et al. (2018). *NIST Standard Reference Database 78: NIST Atomic Spectra Database*. DOI: 10.18434/T4W30F. URL: http://www.nist.gov/pml/data/asd.cfm.

Kromer, M. and S. A. Sim (2009). "Time-dependent three-dimensional spectrum synthesis for Type Ia supernovae". In: *Monthly Notices of the Royal Astronomical Society* 398.4, pp. 1809–1826. ISSN: 00358711. DOI: 10.1111/j.1365-2966.2009.15256.x.

Kromer, M. et al. (2010). "Double-detonation sub-Chandrasekhar supernovae: Synthetic observables for minimum helium shell mass models". In: *The Astrophysical Journal* 719.2, pp. 1067–1082. ISSN: 15384357. DOI: 10.1088/0004-637X/719/2/1067.

Li, W. et al. (2018). "Photometric and Spectroscopic Properties of Type Ia Supernova 2018oh with Early Excess Emission from the Kepler 2 Observations". In: *The Astrophysical Journal* 870.1, p. 12. ISSN: 1538-4357. DOI: 10.3847/1538-4357/aaec74.

Magee, M. R. et al. (2018). "Detecting the signatures of helium in type Iax supernovae". In: *Astronomy and Astrophysics* 622, pp. 1–15. ISSN: 14320746. DOI: 10.1051/0004-6361/201834420.

Magee, M. R. et al. (2020). "Determining the 56 Ni distribution of type Ia supernovae from observations within days of explosion". In: *Astronomy & Astrophysics* 634, A37. ISSN: 0004-6361. DOI: 10.1051/0004-6361/201936684.

Magee, M. R. et al. (2016). "The type Iax supernova, SN 2015H: A white dwarf deflagration candidate". In: *Astronomy and Astrophysics* 589. ISSN: 14320746. DOI: 10.1051/0004-6361/201528036.

Maguire, K. et al. (2013). "A statistical analysis of circumstellar material in type Ia supernovae". In: *Monthly Notices of the Royal Astronomical Society* 436.1, pp. 222–240. ISSN: 00358711. DOI: 10.1093/mnras/stt1586.

Maguire, K. et al. (2014). "Exploring the spectral diversity of low-redshift Type Ia supernovae using the Palomar Transient Factory". In: *Monthly Notices of the Royal Astronomical Society* 444.4, pp. 3258–3274. ISSN: 13652966. DOI: 10.1093/mnras/stu1607.

Mandel, Kaisey S. et al. (2009). "Type ia supernova light-curve inference: Hierarchical bayesian analysis in the near-infrared". In: *The Astrophysical Journal* 704.1, pp. 629–651. ISSN: 15384357. DOI: 10.1088/0004-637X/704/1/629.

Marion, G. H. et al. (2015). "Early observations and analysis of the type Ia SN 2014J in M82". In: *The Astrophysical Journal* 798.1. ISSN: 15384357. DOI: 10.1088/0004-637X/798/1/39.

Marion, G. H. et al. (2013). "High-velocity line forming regions in the type Ia supernova 2009ig". In: *The Astrophysical Journal* 777.1. ISSN: 15384357. DOI: 10.1088/0004-637X/777/1/40.

Mazzali, P. A. et al. (2014). "Hubble Space Telescope spectra of the Type Ia supernova SN 2011fe: A tail of low-density, high-velocity material with $Z \leq Z_{\odot}$". In: *Monthly*

Notices of the Royal Astronomical Society 439.2, pp. 1959–1979. ISSN: 13652966. DOI: 10.1093/mnras/stu077.

Meikle, W.P.S et al. (1996). "An early-time infrared and optical study of the Type IA supernovae SN 1994D and 1991T". In: *Monthly Notices of the Royal Astronomical Society* 281, pp. 263–280.

Miller, A. A. et al. (2020). "The Spectacular Ultraviolet Flash From the Type Ia Supernova 2019yvq". In: URL: http://arxiv.org/abs/2005.05972.

Minkowski, R. (1941). "Spectra of Supernovae". In: *Publications of the Astronomical Society of the Pacific* 53, pp. 224–225.

Modigliani, Andrea and Daniel Bramich (2014). "X-Shooter Pipeline User Manual". In: *VLT-MAN-ESO-14650-4840* 12.2.

Moreno-Raya, Manuel E. et al. (2016). "ON THE DEPENDENCE OF TYPE Ia SNe LUMINOSITIES ON THE METALLICITY OF THEIR HOST GALAXIES". In: *The Astrophysical Journal* 818.1, p. L19. ISSN: 2041-8213. DOI: 10.3847/2041-8205/818/1/l19. URL: http://dx.doi.org/10.3847/2041-8205/818/1/L19.

Noebauer, U. M. et al. (2017). "Early light curves for Type Ia supernova explosion models". In: *Monthly Notices of the Royal Astronomical Society* 472.3, pp. 2787–2799. ISSN: 13652966. DOI: 10.1093/MNRAS/STX2093.

Noll, Stefan et al. (2013). "User Manual for molecfit". In: *VLT–MAN–ESO–19550-5772* 3.10.

Nomoto, K. (1982). "Accreting White Dwarf Models for Type I Supernovae. I. Presupernova Evolution and Triggering Mechanisms". In: *The Astrophysical Journal* 798. URL: http://articles.adsabs.harvard.edu/pdf/1982ApJ...253..798N.

Nomoto, K. and S-C. Leung (2018). "Single Degenerate Models for Type Ia Supernovae: Progenitor's Evolution and Nucleosynthesis Yields". In: URL: http://arxiv.org/abs/1805.10811.

Nomoto, K., F-K. Thielemann, and K. Yokoi (1984). "Accreting white Dwarf Models For Type I Supernovae. III Carbon Deflegration Supernovae". In: *ApJ* 286, pp. 644–658. ISSN: 0007-1250. DOI: 10.1192/bjp.112.483.211-a.

Pan, Y. C. et al. (2015). "Type Ia supernova spectral features in the context of their host galaxy properties". In: *Monthly Notices of the Royal Astronomical Society* 446.1, pp. 354–368. ISSN: 13652966. DOI: 10.1093/mnras/stu2121.

Parrent, J., B. Friesen, and M. Parthasarathy (2014). "A review of type Ia supernova spectra". In: *Astrophysics Space Science* 351, pp. 1–51. DOI: 10.1007/s10509-014-1830-1.

Pastorello, A. et al. (2007). "A giant outburst two years before the core-collapse of a massive star". In: *Nature* 447.7146, pp. 829–832. ISSN: 14764687. DOI: 10.1038/nature05825.

Perets, H. B. et al. (2010). "A faint type of supernova from a white dwarf with a helium-rich companion". In: *Nature* 465.7296, pp. 322–325. ISSN: 00280836. DOI: 10.1038/nature09056.

Perlmutter, S. et al. (1999). "Measurements of Ω and Λ from 42 High-Redshift Supernovae". In: *The Astrophysical Journal* 517.2, pp. 565–586. ISSN: 0004-637X. DOI: 10.1086/307221.

Phillips, M. M. (1993). "The Absolute Magnitudes of Type Ia Supernovae". In: *ApJ* 413, p. 4.

Phillips, M. M. et al. (1992). "SN 1991T - Further evidence of the heterogeneous nature of type IA supernovae". In: *The Astronomical Journal* 103.5, p. 1632. ISSN: 00046256. DOI: 10.1086/116177.

Polin, Abigail, Peter Nugent, and Daniel Kasen (2019). "Observational Predictions for Sub-Chandrasekhar Mass Explosions: Further Evidence for Multiple Progenitor Systems for Type Ia Supernovae". In: *The Astrophysical Journal* 873.1, p. 84. ISSN: 1538-4357. DOI: 10.3847/1538-4357/aafb6a. URL: http://dx.doi.org/10.3847/1538-4357/aafb6a.

Quimby, Robert M. et al. (2007). "SN 2005ap: A Most Brilliant Explosion". In: *The Astrophysical Journal* 668.2, pp. L99–L102. ISSN: 0004-637X. DOI: 10.1086/522862. arXiv: 0709.0302.

Riess, Adam G. et al. (1998). "Observational Evidence from Supernovae for an Accelerating Universe and a Cosmological Constant". In: *The Astronomical Journal* 116.3, pp. 1009–1038. ISSN: 00046256. DOI: 10.1086/300499.

Rigault, M. et al. (2015). "Confirmation of a star formation bias in type IA supernova distances and its effect on the measurement of the Hubble constant". In: *The Astrophysical Journal* 802.1. ISSN: 15384357. DOI: 10.1088/0004-637X/802/1/20.

Rigault, M. et al. (2013). "Evidence of environmental dependencies of Type Ia supernovae from the Nearby Supernova Factory indicated by local H α". In: *Astronomy*

and Astrophysics 560. ISSN: 14320746. DOI: 10.1051/0004-6361/201322104. arXiv: 1309.1182.

Roman, M. et al. (2018). "Dependence of Type Ia supernova luminosities on their local environment". In: *Astronomy and Astrophysics* 615, pp. 1–24. ISSN: 14320746. DOI: 10.1051/0004-6361/201731425. arXiv: 1706.07697.

Ruiz-Lapuente, Pilar et al. (1993). "A possible low-mass type Ia supernova". In: *Nature* 365.6448, pp. 728–730. ISSN: 00280836. DOI: 10.1038/365728a0.

Ruiz-Lapuente, P. et al. (1992). "Modeling The Iron-Dominated Spectra of The Type Ia Supernova SN 1991T at Premaximum". In: *ApJ* 387, pp. L33–, 36. ISSN: 1098-6596. DOI: 10.1017/CBO9781107415324.004.

Sand, D. J. et al. (2018). "Nebular Spectroscopy of the 'Blue Bump' Type Ia Supernova 2017cbv". In: DOI: 10.3847/1538-4357/aacde8. URL: http://arxiv.org/abs/1804.03666%0Ahttp://dx.doi.org/10.3847/1538-4357/aacde8.

Sasdelli, Michele et al. (2014). "Abundance stratification in type Ia supernovae - IV. The luminous, peculiar SN 1991T". In: *Monthly Notices of the Royal Astronomical Society* 445.1, pp. 711–725. ISSN: 13652966. DOI: 10.1093/mnras/stu1777.

Schlegel, E. (1990). "A new subclass of type II supernovae?" In: *Monthly Notices of the Royal Astronomical Society* 244.2, pp. 269–271. ISSN: 0035-8711.

Scolnic, D. M. et al. (2018). "The Complete Light-curve Sample of Spectroscopically Confirmed SNe Ia from Pan-STARRS1 and Cosmological Constraints from the Combined Pantheon Sample". In: *The Astrophysical Journal* 859.2, p. 101. ISSN: 1538-4357. DOI: 10.3847/1538-4357/aab9bb.

Seitenzahl, Ivo R. et al. (2013). "Three-dimensional delayed-detonation models with nucleosynthesis for type ia supernovae". In: *Monthly Notices of the Royal Astronomical Society* 429.2, pp. 1156–1172. ISSN: 00358711. DOI: 10.1093/mnras/sts402.

Shappee, B. J. et al. (2018). "Seeing Double: ASASSN-18bt Exhibits a Two-component Rise in the Early-time K2 Light Curve". In: *The Astrophysical Journal* 870.1, p. 13. ISSN: 1538-4357. DOI: 10.3847/1538-4357/aaec79. URL: http://dx.doi.org/10.3847/1538-4357/aaec79.

Shen, Ken J. and Lars Bildsten (2014). "The Ignition of Carbon Detonations via Converging Shock Waves in White Dwarfs". In: DOI: 10.1088/0004-637X/785/1/61. URL: http://arxiv.org/abs/1305.6925%0Ahttp://dx.doi.org/10.1088/0004-637X/785/1/61.

Shen, Ken J. et al. (2018). "Sub-Chandrasekhar-mass white dwarf detonations revisited". In: *The Astrophysical Journal* 854.1, p. 52. ISSN: 1538-4357. DOI: 10.3847/1538-4357/aaa8de. URL: http://arxiv.org/abs/1706.01898%0Ahttp://dx.doi.org/10.3847/1538-4357/aaa8de.

Silverman, Jeffrey M. et al. (2015). "High-velocity features of calcium and silicon in the spectra of Type Ia supernovae". In: *Monthly Notices of the Royal Astronomical Society* 451.2, pp. 1973–2014. ISSN: 13652966. DOI: 10.1093/mnras/stv1011.

Sim, S. A. et al. (2012). "2D simulations of the double-detonation model for thermonuclear transients from low-mass carbon-oxygen white dwarfs". In: *Monthly Notices of the Royal Astronomical Society* 420.4, pp. 3003–3016. ISSN: 00358711. DOI: 10.1111/j.1365-2966.2011.20162.x.

Sim, S. A. et al. (2010). "Detonations in sub-chandrasekhar-mass C+O white dwarfs". In: *The Astrophysical Journal Letters* 714.1 PART 2, pp. 52–57. ISSN: 20418213. DOI: 10.1088/2041-8205/714/1/L52.

Smette, A. et al. (2015). "Molecfit: A general tool for telluric absorption correction: I. Method and application to ESO instruments". In: *Astronomy and Astrophysics* 576, pp. 1–18. ISSN: 14320746. DOI: 10.1051/0004-6361/201423932.

Sullivan, M. et al. (2006). "Rates and Properties of Type Ia Supernovae as a Function of Mass and Star Formation in Their Host Galaxies". In: *The Astrophysical Journal* 648.2, pp. 868–883. ISSN: 0004-637X. DOI: 10.1086/506137.

Taubenberger, Stefan (2017). "The Extremes of Thermonuclear Supernovae". In: *Handbook of Supernovae*, pp. 317–373. DOI: 10.1007/978-3-319-21846-5{_}37.

Thomas, R. C., P. E. Nugent, and J. C. Meza (2011). "SYNAPPS: Data-Driven Analysis for Supernova Spectroscopy". In: *Publications of the Astronomical Society of the Pacific* 123.900, pp. 237–248. ISSN: 00046280. DOI: 10.1086/658673.

Uddin, Syed A. et al. (2017). "The Influence of Host Galaxies in Type Ia Supernova Cosmology". In: *The Astrophysical Journal* 848.1, p. 56. ISSN: 1538-4357. DOI: 10.3847/1538-4357/aa8df7. arXiv: 1709.05830. URL: http://dx.doi.org/10.3847/1538-4357/aa8df7.

Vernet, J et al. (2011). "X-shooter , the new wide band intermediate resolution spectrograph at the ESO Very Large Telescope". In: *A&A* 536A.105.

Vinkó, J. et al. (2018). "Absolute distances to nearby type Ia supernovae via light curve fitting methods". In: *Publications of the Astronomical Society of the Pacific* 130.988. ISSN: 00046280. DOI: 10.1088/1538-3873/aab258.

Vrieze, S. I. (2012). "Model selection and psychological theory: A discussion of the differences between the Akaike Information Criterion (AIC) and the Bayesian Information Criterion (BIC)". In: *Psychol Methods.* 17.2, pp. 228–243. DOI: 10.1037/a0027127.Model. URL: http://www.unodc.org/unodc/en/data-and-analysis/bulletin/bulletin_1967-01-01_4_page003.html.

Wang, B., S. Justham, and Z. Han (2013). "Producing type Iax supernovae from a specific class of helium-ignited WD explosions". In: *Astronomy and Astrophysics* 559. ISSN: 00046361. DOI: 10.1051/0004-6361/201322298. arXiv: 1310.2297.

Webbink, R. F. (1984). "Double White Dwarfs as Progenitors of R Coronae Borealis Stars and Type I Supernovae". In: *The Astrophysical Journal* 277. URL: http://articles.adsabs.harvard.edu/pdf/1984ApJ...277..355W.

Whelan, J. and I. Iben (1973). "Binaries and Supernovae of Type I". In: *The Astrophysical Journal* 186. URL: http://articles.adsabs.harvard.edu/pdf/1973ApJ...186.1007W.

Yaron, Ofer and Avishay Gal-Yam (2012). "WISeREP - An Interactive Supernova Data Repository". In: *ASP* 3.124, pp. 668–681. ISSN: 00046280. DOI: 10.1086/666656. URL: http://arxiv.org/abs/1204.1891%0Ahttp://dx.doi.org/10.1086/666656.

Zhao, Fu Yuan, R. G. Strom, and Shi Yang Jiang (2006). "The guest star of AD185 must have been a supernova". In: *Chinese Journal of Astronomy and Astrophysics* 6.5. ISSN: 10099271. DOI: 10.1088/1009-9271/6/5/17.

Zhao, Xulin et al. (2016). "The Oxygen Features in Type Ia Supernovae and the Implications for the Nature of Thermonuclear Explosions". In: p. 37. ISSN: 15384357. DOI: 10.3847/0004-637X/826/2/211. URL: http://arxiv.org/abs/1605.07781.

Zhao, Xulin et al. (2015). "The silicon and calcium high-velocity features in type Ia supernovae from early to maximum phases". In: *The Astrophysical Journal, Supplement Series* 220.1, p. 20. ISSN: 00670049. DOI: 10.1088/0067-0049/220/1/20. URL: http://dx.doi.org/10.1088/0067-0049/220/1/20.

Chapter A: Appendix

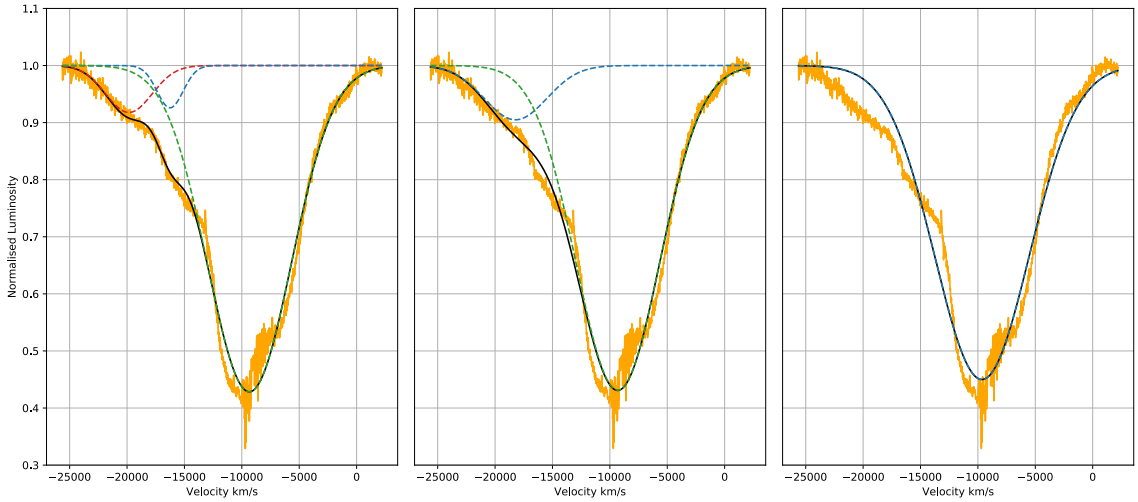

Figure A.1: Example of when the O I 7773 Å fits are used as upper limits for oxygen velocity (SN 2017ejb). The dashed lines represent different lines included in the fit (blue; PVF Oxygen, red; HVF Oxygen, green; Magnesium). The solid black line represents the combined fit. The left panel shows the fit with PVF (middle) + HVF O I (left) + Mg II (right). The middle panel shows the fit for PVF O I (left) and Mg II (right). The right panel shows the fit for PVF O I only (concurrent with the solid black line).

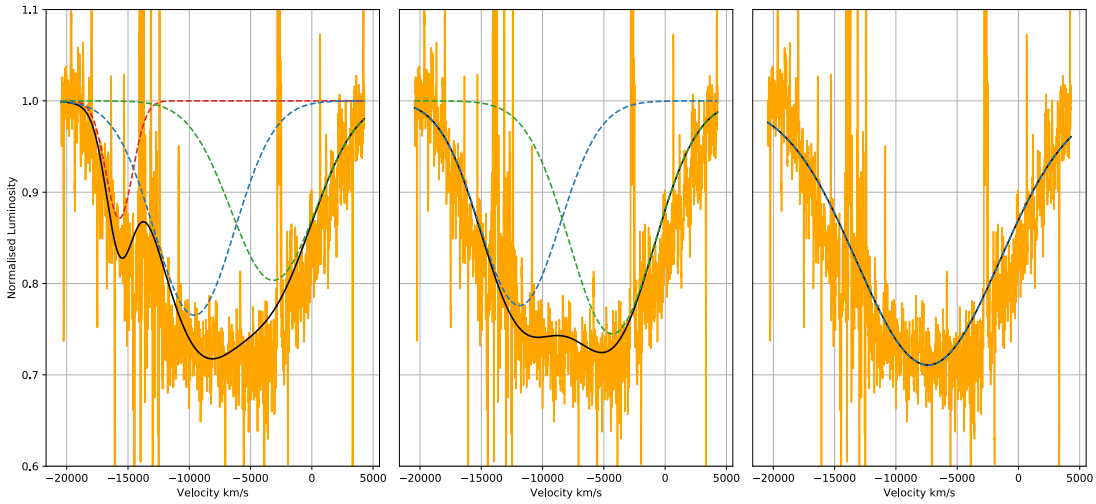

Figure A.2: Example of a poor O I 7773 Å fit for SN 2012et. The dashed lines represent different lines included in the fit (blue; PVF Oxygen, red; HVF Oxygen, green; Magnesium). The solid black line represents the combined fit. The left panel shows the fit with PVF (middle) + HVF (left) O I + Mg II (right). The middle panel shows the fit for PVF O I (left) and Mg II (right). The right panel shows the fit for PVF O I only (concurrent with the solid black line).

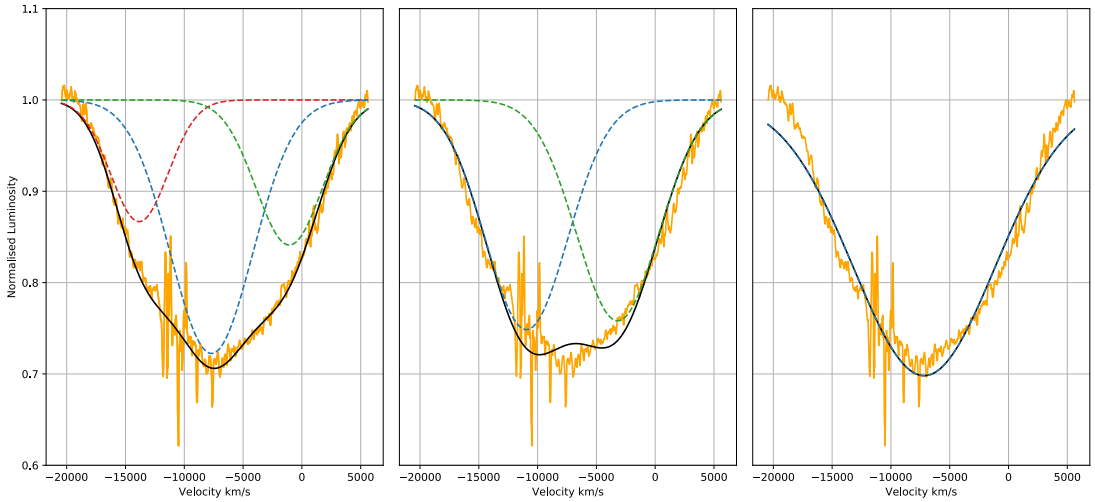

Figure A.3: The O I 7773 Å fit for SN 2017bkc. The dashed lines represent different lines included in the fit (blue; PVF Oxygen, red; HVF Oxygen, green; Magnesium). The solid black line represents the combined fit. The left panel shows the fit with PVF (middle) + HVF (left) O I + Mg II (right). The middle panel shows the fit for PVF O I (left) and Mg II (right). The right panel shows the fit for PVF O I only (concurrent with the solid black line).

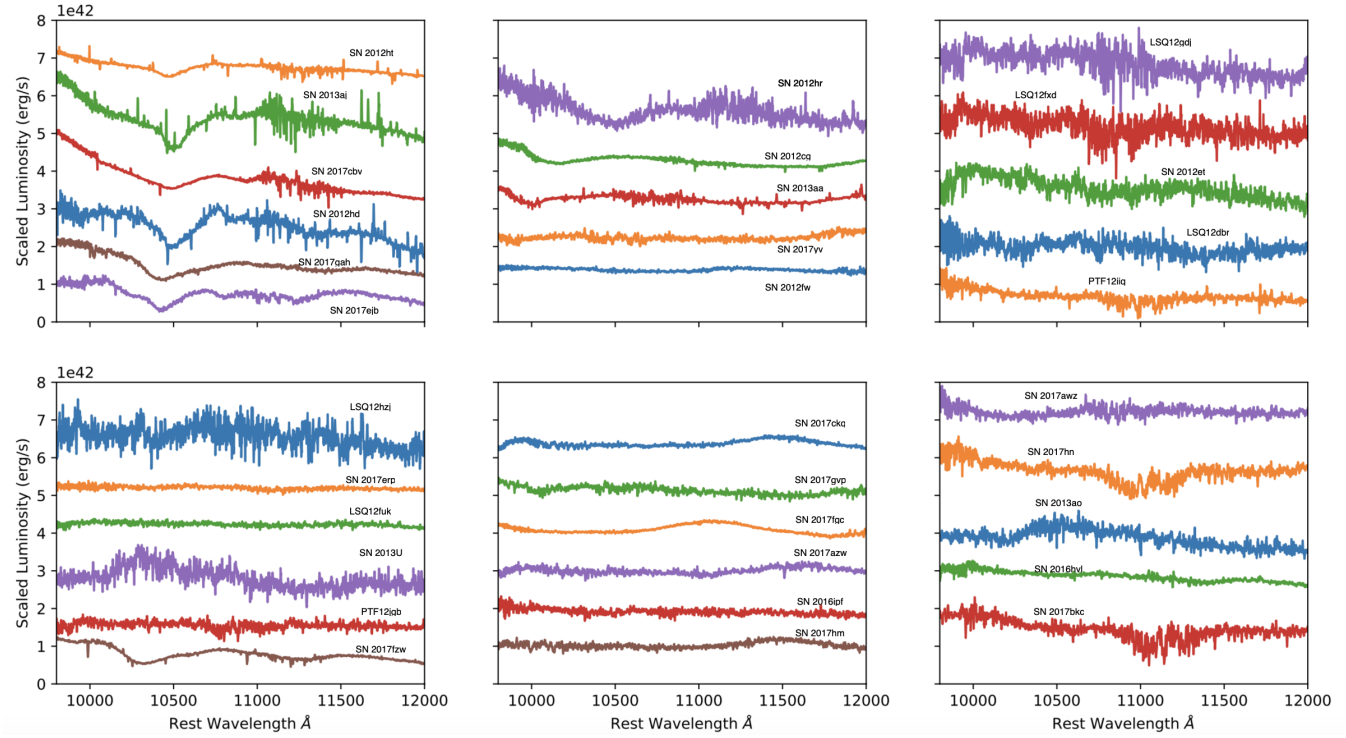

Figure A.4: Zoom in on NIR region where He I is expected to appear for all 33 spectra used in this investigation. The 6 spectra in the left most panel and the top 3 spectra in the second panel from the left make up the 9 objects which show features in this region.